POLYOXOMETALATES

Open Access
REVIEW ARTICLE

Ruthenium containing polyoxometalates: From synthesis, structures, properties to functional applications

Qingmiao Cai[1], Ruili Gao[1], Yanfei Wang[1], Jiashen Xing[1], Qingyang Zhang[1], Muzi Zhu[1], Xinyuan Qin[1], Meihong Liao[2], and Yichao Huang[1] ✉

[1] *State Key Laboratory of Chemical Safety, School of Materials Science and Engineering, China University of Petroleum (East China), Qingdao 266580, China*
[2] *School of Mechanical and Electronic Engineering, Qingdao Binhai University, Qingdao 266555, China*

Cite This: *Polyoxometalates*, **2025**, *4*, 9140083

Read Online

ABSTRACT: Ruthenium-containing polyoxometalates (Ru-POMs) are a class of heteropolyanions (vanadates, molybdates, or tungstates) containing at least one Ru atom as a heteroatom or "addenda" atom. In recent years, Ru-POMs have attracted considerable attention owing to their structural versatility, intriguing redox properties, and oxidation resistance, rendering them highly promising for applications in organocatalysis, electrocatalysis, photocatalysis, and beyond. This review summarizes the advances in Ru-POMs, covering their synthesis methods, structures, properties, and applications. It aims to serve as a reference and guide for the future design and development of novel Ru-POM structures and applications.

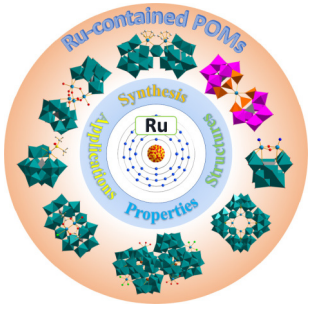

KEYWORDS: ruthenium, polyoxometalates, organocatalysis, electrocatalysis, photocatalysis

1 Introduction

Polyoxometalates (POMs) are a family of polyanionic clusters formed by the coordination of early transition metals (V, Mo, and W, etc.) and oxygen atoms [1, 2]. Due to their well-defined nanocluster structures and tunable redox properties, the potential applications of POMs have been exploded in many fields, such as industrial catalysis, biochemistry, material science and energy [2–6]. Since their initial description in 1826 by Berzelius, specifically the compound $(NH_4)_3[PMo_{12}O_{40}]$ (PMo_{12}), POMs have emerged as a unique subclass of coordination chemistry, attracting widespread attention as advancements in structural characterization techniques have enabled a deeper understanding of their architectures [7, 8]. Especially, ruthenium containing POMs (Ru-POMs), a class of heteropolyanions (vanadates, molybdates or tungstates) that contain at least one Ru atom as a heteroatom or "addenda" atom, have been one of the most investigated hotspots due to their structural versatility, intriguing redox properties and oxidation resistance, leading to valuable applications in electrocatalysis and photocatalysis, etc. [9–11].

In 1989, Neumann and Abu-Gnim reported the first Ru-POMs cluster, $[SiRu(H_2O)W_{11}O_{39}]^{5-}$ (**Ru-SiW11**), which was prepared by the reaction of ruthenium chloride ($RuCl_3{\cdot}H_2O$) and a lacunary $[SiW_{11}O_{39}]^{8-}$ (denoted as SiW11) heteropolyanion in an aqueous solution at 80 °C [12]. In 1992, Pope and Rong reported the synthesis of various $[PW_{11}O_{39}Ru^{n}L]^{p-}$ (L = Me_2SO, $(CH_2)_4SO$, diphenyl sulfoxide (Ph_2SO), Me_2S, Me-cysteine, maleic acid, fumaric acid, crotonic acid, 1,4-dihydroxybut-2-ene, pyridine) complexes with the oxidation state of Ru in the range from +II to +V [13]. Then in 1995, Neuman and Khenkin synthesized $Na_{11}\{[WZnRu^{III}_2(OH)(H_2O)](ZnW_9O_{34})_2\}{\cdot}42H_2O$ by the reaction of $Na_{12}\{[WZn_3(H_2O)_2](ZnW_9O_{34})_2]\}{\cdot}46H_2O$ and $Ru[(CH_3)_2SO]_4Cl_2$ under argon at 90 °C, which was the first Ru-POMs with multi Ru atoms [14]. In 2000, Bonchio and co-workers developed a fast synthesis method to obtain a DMSO-grafted Ru-POMs (DMSO = dimethyl sulfoxide), $[Ru^{II}(DMSO)PW_{11}O_{39}]^{5-}$, within 15 min by using a microwave-assisted hydrothermal condition, which expands the methods for the synthesis of Ru-POMs [15]. In 2008, Hill and Botar et al. prepared a unique Ru-POMs molecular homogenous water oxidation catalyst, $[\{Ru_4O_4(OH)_2(H_2O)_4\}(\gamma\text{-}SiW_{10}O_{36})_2]^{10-}$ (denoted as **Ru4-SiW10**) by the reaction of $[\gamma\text{-}SiW_{10}O_{36}]^{8-}$ (denoted as SiW10) with two equivalents of Ru^{III} in an acidic aqueous solution (pH = 1.6), which is still be widely used now [16]. Currently, researchers focus on synthesizing novel Ru-POM structures containing increased numbers of Ru active sites and ring-like architectures [17].

Usually, transition metal catalysts coordinated with traditional organic macrocyclic ligands may suffer from degradation during the catalytic oxidation reaction due to their susceptibility to self-oxidation. Thus, incorporating transition-metal active sites into the entirely inorganic POMs ligands with resistance to oxidation should enhance their performance work in catalytic oxidation reactions

Received: October 10, 2024; **Revised:** December 3, 2024
Accepted: December 13, 2024

✉Address correspondence to yichaoh@upc.edu.cn

https://doi.org/10.26599/POM.2024.9140083

[18–20]. It should be noted that the lacunary POMs with an "octahedral" binding site on the surface, such as SiW11 and $[P_2W_{17}O_{61}]^{10-}$ (denoted as P2W17), are considered π-acceptor ligands similar to macrocyclic ligands, capable of capturing and stabilizing various transition-metal cations [13, 21, 22]. In 1989, Neumann and Abu-Gnim first used **Ru-SiW11** as a catalyst for the oxidation of alkenes and alkanes with various oxidants, showing that **Ru-SiW11** is a robust catalyst for the oxidation of hydrocarbons [12]. In the early stage, POMs incorporating Ru atoms have received relatively little attention. However, more recent studies, presumably stimulated by the potential organocatalysis applications, have begun to extend to electrocatalysis and photocatalysis applications and to reveal more unexpected properties and new structures.

The electrochemical property of Ru-POMs was firstly investigated by Rong and Pope [13]. They found that the $[PW_{11}O_{39}Ru^{III}(H_2O)]^{4-}$ (denoted as **Ru-PW11**) has the catalyst property for the reduction/oxidization in acidic condition, where three reversible redox couples, $Ru^{III/II}$, $Ru^{IV/III}$ and $Ru^{V/IV}$, exist and the $Ru^{III/II}$ and $Ru^{V/IV}$ potentials are pH independent from pH = 0 to 4 and from 1 to 7, respectively. A similar phenomenon has been confirmed by Bart and Anson [23], who also found three reversible couples, corresponding to $Ru^{III/II}$, $Ru^{IV/III}$ and $Ru^{V/IV}$, in 0.6 mM **Ru-PW11** solution (pH = 2.0) at positive potentials. Moreover, they demonstrated that the as-formed Ru^{V} active site in **Ru-PW11** could be utilized to catalyze the oxidization from alcohols to aldehydes, when a positive potential was applied to oxidize Ru^{IV} to Ru^{V}. It should be noted that Ru-based electrocatalysts with highly efficient oxygen evolution reaction (OER) activity have been widely investigated and recognized as potential alternatives to high-cost and low-reserve iridium (Ir) electrocatalysts [24–28]. However, poor acidic OER stability greatly hampered their widespread applications in proton exchange membrane water electrolysis (PEMWE) technology [24]. Therefore, the development of Ru-based acid-stable OER electrocatalysts has become a hotspot in the field of electrocatalysis [29]. The strong resistance to oxidation and acidic corrosion of Ru-POMs materials makes them of great interest in the applications of electrocatalytic OER.

Apart from organocatalysis and electrocatalysis, the photocatalysis applications of Ru-POMs have also garnered considerable attention. Water oxidation has been considered as the most demanding and challenging step for artificial photosynthetic schemes [30, 31]. In 1982, Meyer and co-workers reported a Ru dimer, $[(bpy)_2(H_2O)Ru^{III}ORu^{III}(H_2O)(bpy)_2]^{4+}$ (bpy = 2,2'-bipyridine), as the soluble and well-defined water oxidation catalyst. In 2008, Hill and Botar et al. found four lines of evidence that prove the **Ru4-SiW10** was stable for water oxidation, including (i) acid-base titrations were reversible from pH 2.5 to 7.5; (ii) cyclic voltammograms (CV) were reproducible and the redox peaks of multiple Ru centers were reversible; (iii) the water oxidation activity of **Ru4-SiW10** was two orders of magnitude higher than that of $RuCl_3$ controlled sample; (iv) the **Ru4-SiW10** catalyst showed a TON (TON = turnover number) of 18 , calculated as TON = $n(O_2)/n$(**Ru4-SiW10**), in the catalytic water oxidation [16]. In the same year, Bonchio et al. prepared the **Ru4-SiW10** catalyst by reacting the SiW10 with $[Ru^{IV}_2OCl_{10}]^{4-}$ in an aqueous solution [32]. The catalytic activity of **Ru4-SiW10** for water oxidation was evaluated by adding an excess of Ce(IV) oxidant in the acidic solution of **Ru4-SiW10** (pH = 0.6), which exhibited a remarkably high turnover frequency (TOF) of over 450 h^{-1} and a robust structure after treatment with excess Ce(IV). Bonchio and co-workers further found that there are five different oxidation states of Ru active sites to power the catalytic cycle for water oxidation in the **Ru4-SiW10** catalyst by monitoring the ultraviolet–visible (UV–vis) and Raman spectroscopy of **Ru4-SiW10** with the stepwise oxidation of air and Ce(IV) in 1 mM **Ru4-SiW10** solution (H_2O/H_2SO_4, pH = 0.6) [33]. Such a unique molecular water oxidation catalyst with multiple Ru active sites stabilized by lacunary POMs ligands provides a new paradigm for the development of photocatalysts for water oxidation. Stimulated by the above pioneering works, more unexpected properties and new structures of Ru-POMs have been revealed in recent studies.

Over the past years, some reviews have been presented with the perspective of Ru-POMs structures. For example, in 2011, Putaj and Lefebvre described the structures and catalytic applications of POMs containing noble metal atoms (Ru, Rh, Pd, Ag, Os, Ir, Pt, and Au) [10]. The structures of Ru-POMs were described as a function of the main metal in the POMs (V, Nb, Mo, and W) and then as a function of its structure (Lindqvist, Keggin, Wells-Dawson, etc.). Subsequently, Izarova, Pope and Kortz also reviewed the advances in POMs containing noble metal ions in 2012, which were classified into two categories, including classical POMs with noble metals as heteroatoms, and the POMs with noble metals as "addenda" atoms [34]. However, it should be noted that only a partial discussion of Ru-POMs was reviewed, and a detailed overview of synthesis methods, structures and applications was not specifically focused. Moreover, since 2012, many new structures and more catalytic applications of Ru-POMs have been developed, thus it is time for a review to summarize the latest research progress in Ru-POMs.

This review aims to provide a comprehensive overview of Ru-POMs, encompassing their synthesis, structures, properties, and applications. Section 2 presents the synthesis and structural aspects of Ru-POMs, including Ru-substituted POMs, sandwich-type Ru-POMs, and other structural variations. Section 3 highlights the properties and applications of Ru-POMs, focusing on their electrochemical redox properties, which serve as a foundation for their utility in electrocatalysis, photocatalysis, and organocatalysis. Finally, the review concludes with a discussion of the current challenges and future prospects of Ru-POMs research.

2 Synthesis and Structures of Ru-POMs

In this section, we describe the synthesis methods and structural characteristics of Ru-POMs, categorized into three main parts: (i) Ru-substituted POMs, which primarily involve typical POMs structures (such as Keggin and Dawson) substituted by Ru ions; (ii) sandwich-type POMs based on typical POMs structures; (iii) other Ru-POMs based on POMs structures that cannot be easily classified. We begin by reviewing Ru-substituted POMs, including monosubstituted Ru-POMs and multisubstituted Ru-POMs, where Ru ions are inserted into the vacancies of the basic Keggin and Dawson POMs. Furthermore, we introduce a unique mode of Ru ion insertion into multi-lacunary POMs and the substitution of a specific POM structure, the Krebs-type POM. The synthesis methods of monosubstituted Ru–POMs are summarized in Table 1, while those of multisubstituted Ru–POMs are presented in Table 2.

2.1 Ru-substituted POMs

The chemistry of Ru-substituted POMs is an important part in the

Table 1 The synthesis methods of monosubstituted Ru-POMs[a]

Entry	Formula	Ru sources	Temp. (°C)	PH	Field	Published year
1	$K_5[SiW_{11}O_{39}Ru(H_2O)]$ [12]	$RuCl_3{\cdot}xH_2O$	80	—	70%	1989
2	$[(C_6H_{13})_4N]_5[SiW_{11}O_{39}Ru(H_2O)]$ [12]	$RuCl_3{\cdot}xH_2O$	80	—	95%	1989
3	$Cs_4[PW_{11}O_{39}Ru^{III}(H_2O)]$ [13]	$[Ru(H_2O)_6](C_7H_7SO_3)_2$	100	3	70%	1992
4	$K_5[SiW_{11}O_{39}Ru^{III}(H_2O)]$ [35]	$RuCl_3$	70	—	45%	1995
5	$Cs_4[PW_{11}O_{39}Ru^{III}(pyridine)]$ [23]	$Cs_4[PW_{11}O_{39}Ru^{III}(H_2O)]$	65	5	—	1995
6	$Cs_3[PW_{11}O_{39}Ru^{III}(pyrazine)]$ [23]	$Cs_4[PW_{11}O_{39}Ru^{III}(H_2O)]$	65	3	—	1995
7	$Cs_3[PW_{11}O_{39}Ru^{III}(N\text{-methylpyrazinium})]$ [23]	$Cs_4[PW_{11}O_{39}Ru^{III}(H_2O)]$	65	3	—	1995
8	$[(n\text{-}C_4H_9)_4N]_4H_4[SiW_{11}Ru^{III}(H_2O)O_{39}]{\cdot}2H_2O$ [36]	$RuCl_3$	20	—	51%	2002
9	$Cs_5[SiW_{11}O_{39}Ru^{III}(H_2O)]{\cdot}15H_2O$ [37]	$Ru(acac)_3$	220	—	55%	2003
10	$Cs_2Na_4[Ru(DMSO)_3(H_2O)GeW_{11}O_{39}]{\cdot}22.5H_2O$ [38]	$cis\text{-}Ru(DMSO)_4Cl_2$	80	4.8	37%	2004
11	$Cs_2Na_4[Ru(DMSO)_3(H_2O)SiW_{11}O_{39}]{\cdot}16H_2O$ [38]	$cis\text{-}Ru(DMSO)_4Cl_2$	80	4.8	35%	2004
12	$Cs_5[PW_{11}O_{39}\{Ru(p\text{-cymene})(H_2O)\}]$ [39]	$[Ru(p\text{-cymene})Cl_2)_2$	—	—	79%	2005
13	$Cs_3K_{0.5}H_{1.5}[PW_{11}O_{39}\{Ru(hexamethylbenzene)(H_2O)\}]$ [39]	$[Ru(hexamethylbenzene)Cl_2]_2$	—	—	90.6%	2005
14	$Cs_{2.5}K_{0.5}H_2[PW_{11}O_{39}\{Ru(toluene)(H_2O)\}]$ [39]	$[Ru(toluene)Cl_2]_2$	20	—	78%	2005
15	$Cs_{5-x}K_x[\alpha\text{-}PW_{11}O_{39}\{Ru(DMSO)_3(H_2O)\}]$ [40]	$fac\text{-}[RuCl_2(DMSO)_3(DMSO)]$	20	—	76%	2006
16	$Cs_4[PW_{11}O_{39}\{Ru^{VI}N\}]$ [41]	$Cs_2[RuNCl_5]$	20	—	48%	2007
17	$TBA_4[PW_{11}O_{39}\{Ru^{VI}N\}]$ [41]	$TBA[RuNCl_4]$	20	—	32%	2007
18	$Cs_6[SiW_{11}O_{39}Ru^{II}(CO)]{\cdot}8H_2O$ [42]	$Ru(acac)_3$	170	—	10%	2008
19	$Na_5[PW_{11}O_{39}Ru^{II}(H_2O)]{\cdot}13H_2O$ [43]	$RuCl_3{\cdot}3H_2O$	80	4.8	—	2009
20	$(n\text{-}Bu_4N)_4[PW_{11}O_{39}Ru^{III}\{N(OH)PPh_3\}]$ [44]	$(n\text{-}Bu_4N)_4[PW_{11}O_{39}Ru^{IV}N]$	—	—	—	2009
21	$(n\text{-}Bu_4N)_4[PW_{11}O_{39}Ru^{III}\{OPPh_3\}]$ [44]	$(n\text{-}Bu_4N)_4[PW_{11}O_{39}Ru^{III}\{N(OH)PPh_3\}]$	20	—	75%	2009
22	$(n\text{-}Bu_4N)_3[PW_{11}O_{39}Ru^{V}\{NPPh_3\}]$ [44]	$(n\text{-}Bu_4N)_4[PW_{11}O_{39}Ru^{IV}N]$	—	—	84%	2009
23	$Cs_{4.7}H_{0.3}[PW_{11}O_{39}Ru^{II}DMSO]{\cdot}9H_2O$ [45]	$Ru(DMSO)_4Cl_2$	125	—	92%	2011
24	$Cs_{3.3}H_{0.7}[PW_{11}O_{39}Ru^{III}DMSO]{\cdot}10H_2O$ [45]	$Cs_{4.7}H_{0.3}[PW_{11}O_{39}Ru^{II}DMSO]{\cdot}9H_2O$	60	—	90%	2011
25	$H_6[FeW_{11}O_{39}Ru(H_2O)]{\cdot}18H_2O$ [46]	$RuCl_3{\cdot}nH_2O$	—	5	60.9%	2011
26	$Cs_5[PW_{11}O_{39}\{Ru^{II}(benzene)(H_2O)\}$ [47]	$[Ru(benzene)Cl_2]_2$	20	—	68%	2012
27	$Cs_6[SiW_{11}O_{39}\{Ru^{II}(benzene)(H_2O)\}$ [47]	$[Ru(benzene)Cl_2]_2$	20	—	28%	2012
28	$Cs_6[GeW_{11}O_{39}\{Ru^{II}(benzene)(H_2O)\}$ [47]	$[Ru(benzene)Cl_2]_2$	20	—	40%	2012
29	$Cs_4[PW_{11}O_{39}Ru^{III}(H_2O)]$ [47]	$[Ru(benzene)Cl_2]_2$	170	—	86%	2012
30	$Cs_5[SiW_{11}O_{39}Ru^{III}(H_2O)]$ [47]	$[Ru(benzene)Cl_2]_2$	170	—	21%	2012
31	$Cs_5[GeW_{11}O_{39}Ru^{III}(H_2O)]$ [47]	$[Ru(benzene)Cl_2]_2$	170	—	38%	2012
32	$TBA_4[PW_{11}O_{39}Ru(NO)]$ [48]	$K_2[Ru(NO)Cl_5]$	150	4.8	93%	2013
33	$TBA_4[PW_{11}O_{39}Ru^{III}(NH_3)]$ [48]	$TBA_4[PW_{11}O_{39}Ru(NO)]$	20	—	75%	2013
34	$K_5[\alpha\text{-}GeW_{11}O_{39}Ru^{III}(H_2O)]{\cdot}10H_2O$ [49]	$Ru(acac)_3$	170	—	66%	2013
35	$Cs_5[\alpha\text{-}GeW_{11}O_{39}Ru^{III}(DMSO)]$ [49]	$K_5[\alpha\text{-}GeW_{11}O_{39}Ru(H_2O)]{\cdot}10H_2O$	80	—	54%	2013
36	$Cs_6[GeW_{11}O_{39}Ru^{II}(DMSO)]$ [50]	$Ru(DMSO)_4Cl_2$	125	—	43%	2014
37	$(n\text{-}Bu_4N)_4[PW_{11}O_{39}Ru^{II}(NO)]$ [51]	$(n\text{-}Bu_4N)_4[PW_{11}O_{39}Ru^{IV}N]$	—	—	97%	2015
38	$(n\text{-}Bu_4N)_4[PW_{11}O_{39}Ru^{IV}(Cl)]$ [51]	$(n\text{-}Bu_4N)_4[PW_{11}O_{39}Ru^{III}(H_2O)]$	—	—	93.3%	2015
39	$K_{18}[Ru^{II}(DMSO)_2(P_2W_{17}O_{61})_2]{\cdot}35H_2O$ [52]	$[RuCl_2(DMSO)_4]$	—	2	68.1%	2001
40	$K_7[\alpha_2\text{-}P_2W_{17}O_{61}Ru^{III}(H_2O)]{\cdot}17H_2O$ [52]	$K_{18}[Ru^{II}(DMSO)_2(P_2W_{17}O_{61})_2]{\cdot}35H_2O$	80	—	29.6%	2001
41	$K_8[\{(C_6H_6)Ru(H_2O)\}(\alpha_2\text{-}P_2W_{17}O_{61})]{\cdot}12H_2O$ [53]	$[(C_6H_6)RuCl_2]_2$	20	—	24.5%	2006
42	$K_8[\{(p\text{-cymene})Ru(H_2O)\}(\alpha_2\text{-}P_2W_{17}O_{61})]{\cdot}16H_2O$ [53]	$[(p\text{-cymene})RuCl_2]_2$	20	—	32.7%	2006
43	$K_8[\alpha_2\text{-}P_2W_{17}O_{61}Ru^{II}(DMSO)]{\cdot}16H_2O$ [54]	$[RuCl_2(DMSO)_4]$	140	—	39%	2014
44	$K_7[P_2W_{17}O_{61}Ru^{III}(H_2O)]$ [54]	$Ru_2(benzene)_2Cl_4$	170	6	42%	2014
45	$K_8[\alpha_1\text{-}P_2W_{17}O_{61}Ru^{II}(DMSO)]{\cdot}4KCl{\cdot}22H_2O$ [54]	$K_7[P_2W_{17}O_{61}Ru^{III}(H_2O)]$	80	—	80%	2014
46	$K_8[\alpha_2\text{-}P_2W_{17}O_{61}Ru^{II}(CO)]{\cdot}19H_2O$ [55]	$Ru(acac)_3$	170	—	10%	2015

(To be continued on the next page)

(Continued)

Entry	Formula	Ru sources	Temp. (°C)	PH	Field	Published year
47	$K_7[\alpha_2\text{-}P_2W_{17}O_{61}Ru^{III}(H_2O)]$ [55]	$Ru(acac)_3$	170	—	10%	2015
48	$K_7[\alpha_1\text{-}P_2W_{17}O_{61}Ru^{III}(H_2O)]$ [56]	$K_8[\alpha_1\text{-}P_2W_{17}O_{61}Ru(DMSO)]\cdot16H_2O$	170	—	57%	2016
49	$K_7[\alpha_2\text{-}P_2W_{17}O_{61}Ru^{III}(H_2O)]$ [56]	$K_8[\alpha_2\text{-}P_2W_{17}O_{61}Ru(DMSO)]\cdot16H_2O$	170	—	57%	2016
50	$((CH_3)_2NH_2)_7[As_2W_{17}\{Ru(NO)\}O_{61}]\cdot4.5H_2O$ [57]	$K_2[Ru(NO)Cl_5]$	160	2	60%	2019
51	$((CH_3)_2NH_2)_{10}[SbW_{17}\{Ru(NO)\}O_{59}]\cdot11H_2O$ [57]	$K_2[Ru(NO)Cl_5]$	160	2	53%	2019
52	$Cs_6KNa_3[SbW_{17}\{Ru(NO)\}O_{59}]\cdot12H_2O$ [57]	$K_2[Ru(NO)Cl_5]$	160	2	35%	2019

[a]TBA = n-Bu_4N = n-tetrabutylammonium, bipy = 4,4'-bipyridine, acac = acetylacetonate, DMSO = dimethyl sulfoxide. "—" indicates that it is not mentioned in the references. The entries 1–38 are Keggin-type Ru-POMs, entries 39–52 are Dawson-type Ru-POMs.

Table 2 The synthesis methods of multisubstituted Ru-POMs[a]

Entry	Formula	Ru source	Temp. (°C)	PH	Field	Published year
1	$Na_7[HW_9O_{33}Ru_2((CH_3)_2SO)_6]\cdot25.5H_2O$ [60]	cis-$Ru(DMSO)_4Cl_2$	80	4.8	50%	2004
2	$[(C_4H_9)_4N]_4\gamma\text{-}[(SiO_4)Ru_2(OH)_2(OH_2)_2W_{10}O_{32}]\cdot2H_2O$ [61]	$RuCl_3\cdot H_2O$	ca. 20	3	89%	2006
3	$K_2(Me_2NH_2)_2H_2[\gamma\text{-}SiW_{10}O_{38}\{RuN\}_2]\cdot5H_2O$ [62]	$Cs_2[RuNCl_5]$	ca. 20	2.7	20%	2009
4	$K_2(Me_2NH_2)_2H_2[\gamma\text{-}GeW_{10}O_{38}\{RuN\}_2]\cdot5\ H_2O$ [62]	$Cs_2[RuNCl_5]$	ca. 20	2.7	—	2009
5	$(n\text{-}Bu_4N)_5K[\gamma\text{-}SiW_{10}O_{38}\{RuN\}_2]$ [62]	$K_2(Me_2NH_2)_2H_2[\gamma\text{-}SiW_{10}O_{38}\{RuN\}_2]\cdot5H_2O$	—	—	51%	2009
6	$\alpha\text{-}K_6Na[SiW_9O_{37}Ru_4(H_2O)_3Cl_3]\cdot14H_2O$ [63]	$RuCl_3\cdot nH_2O$	70~80	5	—	2010
7	$\alpha\text{-}K_7[SiW_9O_{37}Ru_4(H_2O)_3Cl_3]\cdot14H_2O$ [63]	$RuCl_3\cdot nH_2O$	70~80	5	—	2010
8	$\beta\text{-}K_6Na[SiW_9O_{37}Ru_4(H_2O)_3Cl_3]\cdot15H_2O$ [63]	$RuCl_3\cdot nH_2O$	70~80	5.5	—	2010
9	$\alpha\text{-}K_6Na[\{Ru_3O_3(H_2O)Cl_2\}(SiW_9O_{34})]\cdot17H_2O$ [64]	$RuCl_3\cdot nH_2O$	70~80	5	43%	2012

[a]Me = methyl, TBA = n-Bu_4N = n-tetrabutylammonium. "—" indicates that it is not mentioned in the references.

POMs family. Among them, the lacunary Keggin-type POMs (SiW11 or PW11) and Dawson-type POMs (P2W17) are the main ones to capture and stabilize Ru atoms. In this section, we will introduce the Ru-substituted POMs by the following three categories: (i) mono-substituted Ru-POMs, (ii) multi-substituted Ru-POMs, and (iii) other Ru-substituted POMs.

2.1.1 *Mono-substituted Ru-POMs*

For the mono-lacunary Keggin-type POMs (denoted as $[XW_{11}O_{39}]^{n-}$, X = P/Si/Ge), there are two coordination modes for the Ru atom. One is that the Ru center is octahedral coordination, where Ru atom is coordinated with the lacunary POMs via four Ru–O(W) bonds and a Ru–O(X) bond (X = P/Si/Ge), remaining one site to coordinate with a terminal ligand (CO, H_2O, benzene, DMSO, tetramethylene sulfoxide (TMSO), Ph_2SO, etc.) [42, 45, 46, 47] (Fig. 1(a)). The other combination mode is that mono-lacunary Keggin POMs act as bidentate ligands to coordinate with the Ru atom (Ru–O(W), 2.03–2.08 Å) (Fig. 1(b)), while the remaining four sites of Ru atom coordinate with terminal ligands. Interestingly, the positions of oxygen atoms in the bidentate grafting Ru-POMs are nonequivalent and regioselective, resulting in two enantiomers regardless of the nature of the grafted moiety [38, 40]. The grafting mode has been widely used in multi-Ru-ions POMs, which would be frequently mentioned in the following sections.

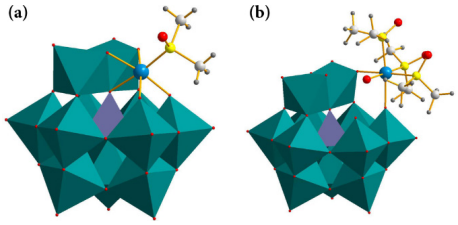

Figure 1 (a) The structure of $[\beta_3\text{-}GeW_{11}O_{39}Ru(DMSO)]^{6-}$. (b) The structure of $[Ru(DMSO)_3(H_2O)GeW_{11}O_{39}]^{6-}$. Color: Ge, blue grey; W, teal; O, red; Ru, blue; C, white; S, yellow; H, grey. (a) was reproduced from Ref. [45]. (b) was reproduced from Ref. [38].

In the first coordination mode of Ru-POMs grafted with different ligands, the average Ru–O bond length (Ru–O(X) (X = P/Si/Ge), 2.12–2.32 Å) between Ru and central heteroatom X of POM varies, decreasing in the order: oxygen-containing ligand (H_2O) > sulfur-containing ligand (DMSO) > nitrogen-containing ligand (4,4'-bipyridine, denoted as bipy). While the bond lengths between Ru and ligands follow the order of Ru-S bond (~ 2.15 Å) > Ru-N bond (~ 2.02 Å) [45, 50, 58], indicating the strong coordination of Ru and the bipy ligand. The organo-Ru with other larger size organic ligands tends to combine with POMs via the second mode due to their steric and electronic effect. Multi-DMSO ligands could also be combined in this mode [38, 40]. However, the exact structure of Ru-POMs containing Ru–CO, such as $Cs_6[SiW_{11}O_{39}Ru^{II}(CO)]$, cannot be determined using X-ray diffraction (XRD) technique because the incorporated Ru atom cannot be differentiated from the W atoms distributed equally over the 12 addenda atom positions of the Keggin POMs [42].

Similar to the Keggin-type POMs, the Dawson-type POMs also have two coordination modes with the Ru atom: (i) The Ru ion is fully incorporated into the POMs unit via five oxygen atoms [54, 56] or (ii) grafted to the POMs via two oxygen atoms [53]. Moreover, the Ru-POMs with $\{\alpha_1\text{-}P_2W_{17}O_{61}\}$ have a chiral configuration, where a set of enantiomeric pairs can be found in the unit cell [54, 56]. It should be noted that a Ru-POMs composed of one Ru ion with two lacunary Dawson POMs, $[Ru^{II}(DMSO)_2(P_2W_{17}O_{61})_2]^{18-}$ (denoted as **Ru-(P2W17)$_2$**), can also

be obtained, in which the Ru atom acts as the symcenter, coordinating with two DMSO ligands through Ru–S bonding and four oxygen atoms from each mono-lacunary Dawson-type POMs. By Br_2 oxidation of **Ru-(P2W17)$_2$**, a paramagnetic Ru-POMs, $[\alpha_2\text{-}P_2W_{17}O_{61}Ru^{III}(H_2O)]^{7-}$, can be obtained as a black crystalline compound without solvated or coordinating DMSO [52].

Most Keggin-type Ru-POMs were synthesized under hydrothermal conditions without the need for precise pH control, except for a few cases requiring acidic conditions (pH 2–6) (Table 1). In all the mono-substituted Ru-POMs, it seems that **Ru-PW11** has a better yield than the other Ru-POMs (Table 1). These Ru-POMs materials are usually obtained by reacting mono-lacunary Keggin-type POMs with Ru salts, such as $RuCl_3{\cdot}xH_2O$ or $Ru(DMSO)_4Cl_2$, in a ratio of 1:1 (Fig. 2). Furthermore, Sadakane's group synthesized the POMs in a ratio of 2:1 and increased the temperature to improve the yield (Table 1, entries 1 and 29) [47]. However, comparing the entries 9 and 30, it could be found that with higher temperature, the yield in a ratio of 1:1 is higher than that in a ratio of 2:1. For different Ru sources, it is hard to confirm which the main factor is. It still needs a further study to find the best condition to synthesize the mono-substituted Ru-POMs. Sometimes, the ligands on Ru atom of Ru-POMs could also be replaced by the other ligands. The ligands exchange methods have also been widely used to prepare Ru-POMs, which usually have a better yield than using the $RuCl_3$ and its analogues as precursors (Table 1). For example, the N grafted Ru-POMs, $[PW_{11}O_{39}Ru^{IV}N]^{4-}$ can be efficiently converted into $[PW_{11}O_{39}Ru^{II}(NO)]^{4-}$ with a high yield of 97% (Table 1, entry 37) [51]. For the synthesis of some Ru-POMs with other central heteroatom, such as $H_6[FeW_{11}O_{39}Ru(H_2O)]{\cdot}18H_2O$, Wu and co-workers successively added solution of $Fe(NO_3)_3{\cdot}9H_2O$ and $RuCl_3{\cdot}nH_2O$ dropwise with stirring into the boiling solution of $Na_2WO_4{\cdot}H_2O$. The final product was obtained by passing through an Amberlite IR-120 cation-exchange column in H^+ form until the pH is less than 1 [46]. Usually, K^+, Cs^+, and TBA^+ cations were utilized to precipitate the Ru-POMs products. The choice of the cations may also make a different for the yield (Table 1, entries 1 and 2). Especially, using TBA^+ cation to precipitate the Ru-POMs product can transfer Ru-POMs from aqueous solution to organic solution, such as chloroform, DMSO, *N,N*-dimethylformamide (DMF), acetone and acetonitrile [58].

Except for the hydrothermal reactions or traditional refluxing reactions, some new methods have been developed. For example, in 2000, Bonchio and co-workers developed a fast synthesis method to obtain a DMSO-grafted Ru-POMs, $[Ru^{II}(DMSO)PW_{11}O_{39}]^{5-}$, with 15 min by using a microwave-assisted hydrothermal condition [15].

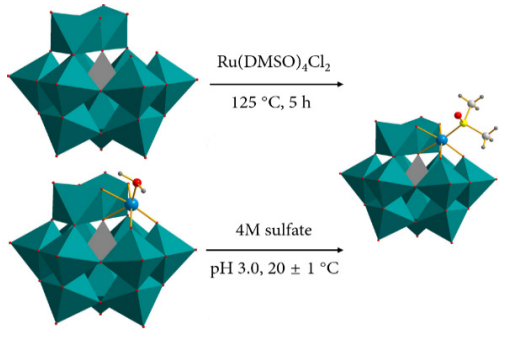

Figure 2 Two different synthetic methods for $[PW_{11}O_{39}Ru^{II}(DMSO)]^{5-}$. Color: P, dark grey; W, teal; O, red; Ru, blue; C, white; S, yellow; H, grey. These structures were reproduced from Ref. [45].

In 2005, Proust's group synthesized $Cs_5[PW_{11}O_{39}Ru^{II}L]$ (L = DMSO, TMSO, Ph_2SO) by adding organic compounds into a degassed deuterated aqueous solution of $Cs_5[PW_{11}O_{39}\{Ru(p\text{-}cymene)(H_2O)\}]$ and then ultraviolet irradiation of the samples to gain yield of 77%, 35%, and 57%, respectively [39]. In 2009, Izzet's group synthesized **Ru-PW11** by the microwave irradiation of mono-lacunary PW11 POMs and $[Ru(DMF)_6](CF_3SO_3)_3$ [59]. In 2015, Yan and Yi et al. developed a new synthesis method to prepare the **Ru-PW11** with a high yield of 95.7% by irradiating the $[PW_{11}O_{39}Ru^{II}(NO)]^{4-}$ precursor with Hg immersion lamp (253.7 nm, 70 W) for 3 h [51].

2.1.2 *Multisubstituted Ru-POMs*

Ru-POMs with two Ru ions are also fascinating. In 2004, Kortz's group firstly synthesized multi-substituted Ru-POMs, $[HW_9O_{33}Ru_2((CH_3)_2SO)_6]^{7-}$ (denoted as **Ru-W9-Ru**), by the reaction of $Na_2WO_4{\cdot}2H_2O$ and cis-$Ru(DMSO)_4Cl_2$ in a ratio of 1:4.5 at 80 °C (pH = 4.8). There are two unconnected Ru ions in the **Ru-W9-Ru**, the Ru centers are coordinated with three oxo-groups of the isopolytungstate core and with the sulfur atoms of three terminal DMSO ligands which lead to a trigonal antiprismatic coordination geometry for the Ru (Fig. 3(a)) [60].

In 2006, Hill and Musaev et al. firstly synthesized $[(C_4H_9)_4N]_4\gamma\text{-}[(XO_4)Ru_2(OH)_2(OH_2)_2W_{10}O_{32}]{\cdot}2H_2O$ (denoted as **Ru2-XW10**, X = P/Si/Ge/Al/S), which maintains two connected Ru atoms, by the reaction of SiW10 and $RuCl_3{\cdot}H_2O$ in a ratio of 1:2 under argon at room temperature (pH = 3) (Table 2, entry 2) [61]. Later on, Proust's group tried to attach N-contained ligands to the POMs by the reaction of SiW10 and $Cs_2[RuNCl_5]$ at room temperature (pH = 2.7) (Table 2, entries 3–5) [62]. In **Ru2-XW10**, the Ru atoms exhibit six-coordination sites, including three oxygen atoms from the POMs, two Ru–O(Ru) bonds, and one terminal ligand. The ground electronic states and, consequently, the reactivity of the γ-Ru_2-Keggin POMs are determined by the heteroatom X, which acts as an "internal switch." The (Ru–O(Ru)–Ru–O(Ru)) dihedral angle is approximately −34.7° (this angle may vary with different ligands, e.g., for N, the angle is 6.0°, and the Ru–O(Si) distance increases from 2.072 to 2.600 Å) [61, 62].

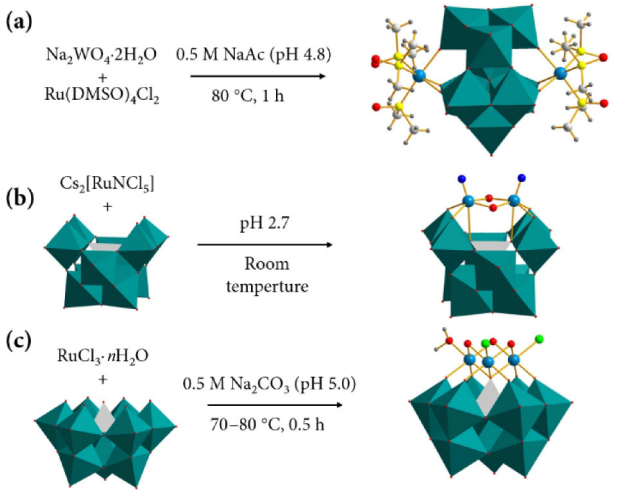

Figure 3 (a) The synthetic method of $[HW_9O_{33}Ru_2((CH_3)_2SO)_6]^{7-}$. (b) The synthetic method of $[\gamma\text{-}SiW_{10}O_{38}\{RuN\}_2]^{6-}$. (c) The synthetic method of $[\{Ru_3O_3(H_2O)Cl_2\}(SiW_9O_{34})]^{7-}$. Color: W, teal; O, red; Ru, blue; C, white; S, yellow; H, grey; Si, light grey; N, dark blue; Cl, green. (a) was reproduced from Ref. [60]. (b) was reproduced from Ref. [61]. (c) was reproduced from Ref. [64].

Later on, the multi-substituted Ru-POMs based on tri-lacunary Keggin-type POMs have been studied. In 2010, Cavaleiro's group attached $\{Ru_4\}$ to the tri-lacunary Keggin-type POMs getting $[SiW_9O_{37}Ru_4(H_2O)_3Cl_3]^{7-}$ (denoted as **Ru4-SiW9**) by the reaction of $RuCl_3{\cdot}nH_2O$ and α-$Na_{10}[SiW_9O_{34}]{\cdot}15H_2O$ at 80 °C (pH = 5). In those POMs, each Ru atom, which is in a cluster type $\{Ru_4O_4\}$, is combined with three O atoms around it, three of them with the O around act as a cluster, which is similar to $\{W_3O_{12}\}$, to connect to the Keggin structure via each two Ru–O(W) bonds (2.01 to 2.10 Å), the internal Ru–O(Ru) distances range from 1.877 to 2.169 Å [63]. In 2012, Car and Patzke et al. synthesized a trinuclear Ru-POMs, α-$K_6Na[\{Ru_3O_3(H_2O)Cl_2\}(SiW_9O_{34})]{\cdot}17H_2O$ (denoted as **Ru3-SiW9**), using the same reaction (Table 2, entries 6–9) but with the addition of a centrifugation step at 3500 rpm. It appears that this additional procedure was essential in obtaining the new structure. In **Ru3-SiW9**, the capping $\{Ru_3\}$ unit is connected to the $\{SiW_9O_{34}\}$ shell via Ru–O(W) bonds between 2.064 and 2.101 Å, which acts as a cluster similar to the $\{W_3O_{12}\}$ group in the Keggin-type POM (Fig. 3(c)), and the internal Ru–O(Ru) distances range from 1.877 to 2.169 Å [64]. Therefore, the increase of the number of catalytically active Ru centers in the POMs structure is of high interest to allow them to become good oxidation catalysts.

2.1.3 *Other Ru-substituted POMs.*

The POMs with more lacunary sites usually can capture more Ru ions, forming multi-substituted Ru-POMs. However, there are some exceptions due to the steric effects. For example, Kortz and Nadjo et al. synthesized a new Ru-POMs structure, $[\{Ru(C_6H_6)(H_2O)\}\{Ru(C_6H_6)\}(\gamma\text{-}GeW_{10}O_{36})]^{4-}$, by the reaction of SiW10 and $[Ru(C_6H_6)Cl_2]_2$ in a ratio of 1:1 at 80 °C (pH = 2.5), which is quite different from the synthesis of **Ru2-XW10**. It appears that the choice of starting materials plays a critical role in determining the outcome. It could be found that the $Ru(C_6H_6)(H_2O)$ unit occupied the lacunary site of $[Si/GeW_{10}O_{36}]^{n-}$ via two Ru–O(W) bonds. Interestingly, the other $Ru(C_6H_6)$ unit is not coordinated at the lacunary site but at the side of POMs through three bridging oxygen atoms due to the steric effects of $Ru(C_6H_6)$ ligand (Fig. 4(a)) [65]. Additionally, Kortz et al. discovered that in some cases, one (RuC_6H_6) unit coordinates to the lacuna of the $\{Si/GeW_9O_{34}\}$ POMs *via* two Ru–O(W) bonds and one Ru–O(Si/Ge) bond, while the other (RuC_6H_6) unit attaches to the opposite end of the POMs through three bridging oxygen atoms. The new Ru-POMs, $[(RuC_6H_6)_2GeW_9O_{34}]^{6-}$, was synthesized in the same condition by replacing $[GeW_{10}O_{36}]^{8-}$ with $[GeW_9O_{34}]^{10-}$ (Fig. 4(b)) [66]. Subsequently, Sadakane et al. demonstrated that a mono-(benzene)Ru(II) attached POM, $[\gamma\text{-}SiW_{10}O_{36}Ru(C_6H_6)]^{6-}$, could be obtained at room temperature. They showed that if only one $Ru(C_6H_6)$ group was present, it preferred to bind at the non-lacunary site of the POMs, as confirmed by single-crystal X-ray structure analysis, nuclear magnetic resonance (NMR) spectroscopy, high-resolution ESI mass spectrometry (MS), and density functional theory (DFT) calculations [67].

A unique structure, the Krebs-type compound structure $[X_2W_{22}O_{74}(OH)_2]^{12-}$ (X = Sb, Bi, Te) has been widely used in Ru-POMs, which was first reported by Bernt Krebs et al. in 1997 [68]. In 2005, Proust's firstly attached organo-Ru group {Ru(p-cymene)} to the Krebs-type POM, and later in 2009, Richards and Kortz et al. attached $\{Ru(C_6H_6)\}$ to the Krebs-type POMs. The POMs, $[Sb_2W_{20}O_{70}(RuL)_2]^{10-}$ (L = p-cymene, C_6H_6), were obtained by the reaction of $[RuLCl_2]_2$ (L = p-cymene, C_6H_6) and

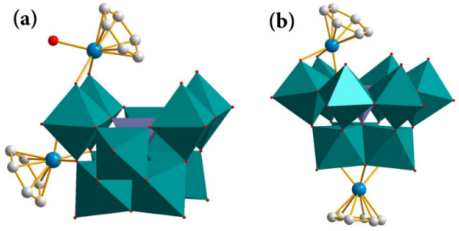

Figure 4 (a) The structure of $[\{Ru(C_6H_6)(H_2O)\}\{Ru(C_6H_6)\}(\gamma\text{-}GeW_{10}O_{36})]^{4-}$. (b) The structure of $[(RuC_6H_6)_2GeW_9O_{34}]^{6-}$. Color: Ge, blue grey; W, teal; O, red; Ru, blue; C, white. (a) was reproduced from Ref. [65]. (b) was reproduced from Ref. [66].

$Na_{12}[Sb_2W_{22}O_{74}(OH)_2]$ in a ratio of 1:1 at 50 °C (pH = 6.0). In such Ru-POMs, they are composed of two trilacunary B-β-$[XW_9O_{33}]^{8-}$ Keggin fragments linked via two inner cis-WO_2 groups and two outer {RuL} (L = p-cymene, C_6H_6) units, which result in a structure with perfect C_{2h} symmetry. Alternatively, these Ru-POMs can be described as a dilacunary $[X_2W_{20}O_{70}]^{12-}$ fragment stabilized by two {RuL} (L = C_6H_6, $C_{10}H_{14}$) units. In the structure, an oxygen atom from one $\{XW_9O_{33}\}$ unit and two oxygen atoms from the other $\{XW_9O_{33}\}$ unit coordinate to the Ru ions in the POMs (Fig. 5(a)). Moreover, the coordination mode of the Ru center of the Krebs-type POMs is different to the other dimeric organo-Ru containing POMs, which is probably attributed to the lone pair repulsion in the POMs. In them, the lengths of Ru–O(W) bonds are around 2.08–2.10 Å [69, 70].

In 2009, Bi and Wu et al. synthesized $[Ru^{II}(bpy)_3]_2[Sb_2W_{20}Ru^{III}_2(H_2O)_2(DMSO)_6O_{68}]{\cdot}3DMSO$ via the reaction of $K_6Na_4[Sb_2W_{20}Mn_2(H_2O)_6O_{70}]$ and $Ru(bpy)_3Cl_2$ in a 2:5 molar ratio in a 1:1 DMSO/H_2O mixture at 80°C. The presence of different ligands resulted in slight variations in the structure. In the POM complex, the Ru centers were coordinated to the POM framework in the same mode (Ru–O(W) distances of 2.05–2.20 Å). Notably, four of the six DMSO ligands bonded to the two Ru centers through Ru–O–$S(CH_3)_2$ bonds, distinguishing them from other POMs with DMSO ligands. The other two link the two W centers, connecting the two (B-β–SbW_9O_{33}) units via W–O–$S(CH_3)_2$ bonds (Fig. 5(b)). This unique combination mode is of particular interest [71].

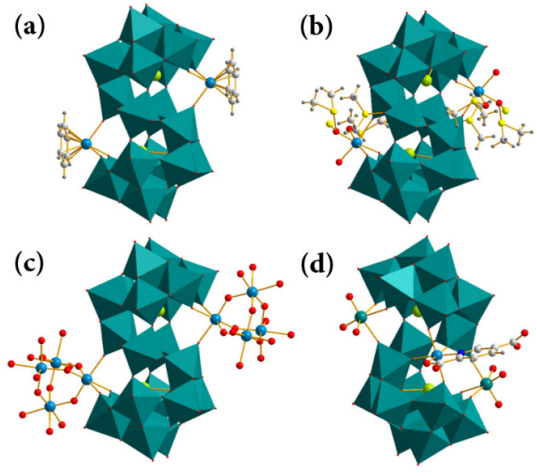

Figure 5 (a) The structure of $[Sb_2W_{20}O_{70}(RuC_6H_6)_2]^{10-}$. (b) The structure of $[Sb_2W_{20}Ru^{III}_2(H_2O)_2(DMSO)_6O_{68}]^{4-}$. (c) The structure of $[\{Ru^{IV}_4O_6(H_2O)_9\}_2Sb_2W_{20}O_{68}(OH)_2]^{4-}$. (d) The structure of $[(SbW_9O_{33})_2\{WO_2(OH)\}_2\{WO_2\}RuC_7H_3NO_4]^{12-}$. Color: W, teal; O, red; Ru, blue; C, white; S, yellow; H, grey; Sb lime. (a) was reproduced from Ref. [70]. (b) was reproduced from Ref. [71]. (c) was reproduced from Ref. [72]. (d) was reproduced from Ref. [74].

In 2012, Kortz's group replaced the organo-Ru with $\{Ru_4\}$ group to get $[\{Ru^{IV}_4O_6(H_2O)_9\}_2Sb_2W_{20}O_{68}(OH)_2]^{4-}$ (denoted as **Ru4SbW9-W2-Ru4SbW9**) by the reaction of $(NH_4)_2[RuCl_6]$ and $Na_{12}[Sb_2W_{22}O_{74}(OH)_2]$ at 90 °C with oil bath heating at pH 1.5. While using $[Fe_4(H_2O)_{10}(\beta\text{-}TeW_9O_{33})_2]^{4-}$ at 110 °C, they synthesized $[\{Ru^{IV}_4O_6(H_2O)_9\}_2\{Fe(H_2O)_2\}_2\{\beta\text{-}TeW_9O_{33}\}_2H]^-$ (denoted as **Ru4TeW9-Fe2-Ru4TeW9**). The $\{Ru_4\}$ units are linked to the POM fragment as the way above by only one of the four Ru^{IV} ions, via three Ru–O(W) bridges (2.099–2.144 Å). For the other three Ru^{IV} ions which are remained, their coordination sphere is achieved via three terminal aqua ligands (Ru–O, 2.107–2.216 Å). Finally, for the each {Ru4} motif, the four octahedrally coordinated Ru^{IV} ions are connected via six oxo bridges (Ru–O, 1.830–1.889 Å) (Fig. 5(c)). The coordination mode of $\{Ru_4\}$ seems to be the idealized mode for the four Ru atoms with high valence to bound, which is also utilized to form the sandwich-type POMs introduced in the following. The **Ru4TeW9-Fe2-Ru4TeW9** is similar to the **Ru4SbW9-W2-Ru4SbW9**, but the length of Ru–O(W) bridges changed in the ranges of 1.853–1.885 Å. The Ru-POMs possess tremendous potential catalytic applications because the $\{Ru^{IV}_4\}$ units are bound in a highly accessible, external fashion [72].

In 2016, Bi et al. synthesized $Na_6(TMA)_2[Te_2W_{20}O_{70}(RuC_6H_6)_2]\cdot 25H_2O$ via a simplified reaction process involving $Na_2WO_4{\cdot}2H_2O$, TeO_2 (pH 4.7), and $[RuC_6H_6Cl_2]_2$ in a ratio of 15:2:1 at 50 °C [73]. These Krebs' POMs are promising catalysts owing to the highly accessible and external coordination of the Ru units to the POM framework.

The Ru centers coud not only occupy the two internal positions but also the central position. In 2023, Niu et al. synthesized $Na_{5.5}H_{6.5}[(SbW_9O_{33})_2\{WO_2(OH)\}_2\{WO_2\}RuC_7H_3NO_4]\cdot 36H_2O$ through a multistep procedure: (i) mixing $Na_2WO_4{\cdot}2H_2O$ and Sb_2O_3 (pH 3.4–3.9), (ii) adding $RuCl_3$ and 2,5-dicarboxylic acid to the solution, and (iii) heating at 160 °C. In the resulting Ru-POMs, the Ru coordination center is formed by four μ_2-O atoms from $\{SbW_9\}$ (1.91–2.05 Å), one carboxyl oxygen, and one nitrogen atom from the $\{RuC_7H_3NO_4\}^{2+}$ ligands (Fig. 5(d)). The POMs further assemble into layered ionic crystals via Na-bridged sheets and hydrogen-bonded layers, resulting in high electrical conductivity [74].

2.2 Sandwich-type Ru-POMs

Sandwich-type POMs are a kind of multi-functional compounds which have been widely studied. They are mainly composed of two lacunary POMs and metal ions, which form structures similar to "hamburger". The Ru ions could act as the "filling" or load on the POMs, in this section, their structures and synthesis methods are introduced systematically. We review the typical sandwich-type POMs and pseudo-sandwich-type POMs in this section.

2.2.1 *Typical Sandwich-type Ru-POMs*

In 1995, Neuman and Khenkin made a groundbreaking discovery by synthesizing $Na_{11}\{[WZnRu^{III}_2(OH)(H_2O)](ZnW_9O_{34})_2\}\cdot 42H_2O$. This remarkable compound was prepared via the reaction of $Na_{12}\{[WZn_3(H_2O)_2](ZnW_9O_{34})_2]\}\cdot 46H_2O$ and $Ru[(CH_3)_2SO]_4Cl_2$ in a 1:3 ratio under argon at 90 °C. Notably, this was the first reported Ru-POM containing multiple Ru ions. The sandwich structure features a tetranuclear ring $\{WZnRu^{III}_2(OH)(H_2O)\}$ as the filling, which is sandwiched between two trivacant Keggin-type $[B\text{-}\alpha\text{-}ZnW_9O_{34}]^{10-}$ moieties. All metal centers exhibit six-coordinated environments. The Ru center is coordinated to five oxygen atoms from the POMs and one terminally bound water ligand. For the Zn and W centers, all oxygen atoms originate from the POMs. These four $\{MO_6\}$ octahedra are interconnected via edge-sharing interactions, forming a rhombus-like cluster (Fig. 6(a)) [14]. Neuman and Dahan further studied the structure in 1997 and 1998, who found that the non-oxidizable Zn could help Ru have a better redox property [75, 76]. In 2008, Proust's group synthesized $Rb_{9.5}K_{0.5}\{PW_{11}O_{39}\}_2\{(HO)Ru^{IV}\text{–}O\text{–}Ru^{IV}(OH)\}\cdot 18H_2O$ (denoted as **Ru2-PW11**) by the reaction of a $K_7[PW_{11}O_{39}]\cdot 14H_2O$ and $[Ru_2(O_2CCH_3)_4]Cl$ in a ratio of 2:1 at 120 °C (pH = 2.9). In the **Ru2-PW11**, two lacunary $[\alpha\text{-}PW_{11}O_{39}]^{7-}$ POMs are bridged by a $\{(HO)Ru^{IV}\text{–}O\text{–}Ru^{IV}(OH)\}$ cluster. This cluster is coordinated in a near-linear arrangement (Ru–O–Ru angle: 175.2°; O–Ru–O angles: 178.5° and 178.0°). Each Ru^{IV} ion attains six-coordination by bonding to two terminal oxo ligands from the lacuna of each $[PW_{11}O_{39}]^{7-}$ anion. These four oxygen atoms form a square planar environment around the Ru^{IV} ions (Fig. 6(b)) [77].

In the same year, Botar et al. discovered a highly effective POM structure that remains widely used today: $Rb_8K_2[\{Ru_4O_4(OH)_2(H_2O)_4\}(\gamma\text{-}SiW_{10}O_{36})_2]\cdot 25H_2O$ (denoted as Ru4-SiW10). This compound was synthesized via the reaction of SiW10 with two equivalents of $RuCl_3{\cdot}H_2O$ in an acidic aqueous solution (pH = 1.6), followed by precipitation of the product using RbCl (Figs. 6(c) and 7(a)) [16]. Meanwhile, Sartorel, Geremia and Bonchio et al. synthesized $Cs_{10}[Ru_4(\mu\text{-}O)_4(\mu\text{-}OH)_2(H_2O)_4(\gamma\text{-}SiW_{10}O_{36})_2]$ through the reaction of SiW10 and $K_4Ru_2OCl_{10}$ at 90 °C for an hour (pH = 6.2/1.8 after heating), with CsCl used for product precipitation (Fig. 7(b)) [32]. While Bonchio's method offers a higher yield (75% vs. 40%), Hill's method is considered milder. And in the Bonchio's method, the dosage of Ru source is higher than the dosage of the lacunary POM, which also explains difficulty of the synthesis. The study of how to increase the yield is worth further conducting. For the structure, this is a major milestone in the research of Ru-POMs. First, we will further introduce the major fragment

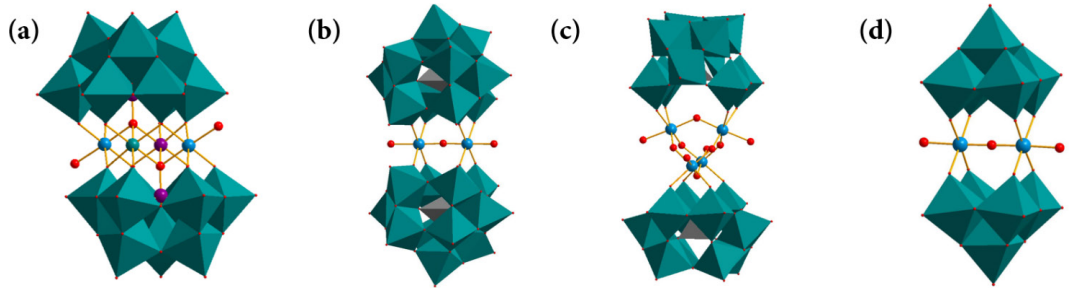

Figure 6 (a) The structure of $[WZnRu^{III}_2(OH)(H_2O)(ZnW_9O_{34})_2]^{11-}$. (b) The structure of $[(Ru(OH))_2O(PW_{11}O_{39})_2]^{10-}$. (c) The structure of $[\{Ru_4O_4(OH)_2(H_2O)_4\}(\gamma\text{-}SiW_{10}O_{36})_2]^{10-}$. (d) The structure of $[(Ru(OH))_2O(W_5O_{18})_2]^{8-}$. Color: W, teal; O, red; Ru, blue; Zn, violet; P, dark grey; Si, light grey. (a) was reproduced from Ref. [14]. (b) was reproduced from Ref. [77]. (c) was reproduced from Ref. [16]. (d) was reproduced from Ref. [80].

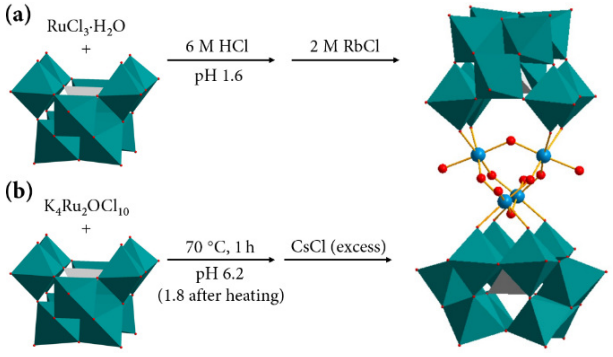

Figure 7 (a) Bonchio's synthetic route to $Cs_{10}[\{Ru_4O_4(OH)_2(H_2O)_4\}(\gamma\text{-}SiW_{10}O_{36})_2]$. (b) Hill's synthetic route to $Rb_8K_2[\{Ru_4O_4(OH)_2(H_2O)_4\}(\gamma\text{-}SiW_{10}O_{36})_2]·25H_2O$. Color: W, teal; O, red; Ru, blue; Si, light grey. (a) was reproduced from Ref. [16]. (b) was reproduced from Ref. [32].

$\{Ru_4O_4(OH)_2(H_2O)_4\}$, in which the four Ru centers span a slightly distorted tetrahedron with Ru···Ru distances of 3.47–3.66 Å. Different from the $\{Ru_4\}$ in the **Ru4SbW9-W2-Ru4SbW9**, more external oxygen atoms are derived from the POMs, which make the $\{Ru_4\}$ gorup a slight distinction. Consequently, the $\{Ru_4\}$ core in **Ru4-SiW10** displays the expected adamantane-like arrangement, with four Ru atoms and six oxygen atoms at the apexes of a tetrahedron and of an octahedron, respectively. In addition, the Ru ions' high valent (+IV) also predicts its high activity.

For the whole POM, it could be considered as two "out-of-pocket" γ-$\{SiW_{10}Ru_2\}$ monomeric units rotated by 90° around the vertical C_2 axis relative to one another. Consequently, the combination mode leads the POM to a D_{2d} symmetry. The adjacent Ru centers within each γ-$\{SiW_{10}Ru_2\}$ unit are bridged by hydroxo ligands, and oxo ligands bridge the Ru centers of different monomeric units (Fig. 6(c)). These two bridging motifs are associated with bent hydroxo bridges that connect two adjacent Ru^{IV} centers linked to different POM binding sites (Ru–O–Ru bond angle of 131.2°) [16, 32]. In the next few years, similar POMs incorporating different heteroatoms and Ru ions with varying valence states have been investigated, although they exhibit no considerable structural differences. There are only a few differences in the bonds' lengths, bonds' angles and oxygen's existing ways. For example, in $[\{Ru^{V}Ru^{IV}_3O_6(OH_2)_4\}(\gamma\text{-}SiW_{10}O_{36})_2]^{11-}$ (the synthesis way is similar to Hill's), with lower negative electron density on the $[Ru_4O_6]$ core compared with the standard **Ru4-SiW10**, none of these $[Ru_4O_6]$ core oxygens are protonated, while all four Ru terminal ligands in it remain aqua as in standard **Ru4-SiW10** and not hydroxo [78]. For $Cs_9[(\gamma\text{-}PW_{10}O_{36})_2Ru^{IV}_4O_5(OH)(H_2O)_4]$, synthesized in a more acidic condition (pH = 0.6), the oxygen atoms linking the $\{PW_{10}O_{37}Ru_2\}$ units are non-protonated (the average bond valence sums (BVS) = 1.87), while the oxygen atoms bridging the two Ru centers within one $\{PW_{10}O_{37}Ru_2\}$ unit display a BVS of 1.35 and 1.48, significantly lower than the previous value but still higher than that encounter in the silicon analogue where both bridges are protonated (BVS never exceeds 1.30 in this case) [79].

In 2022, Niu and Wang et al. successfully synthesized another linear structure, $Cs_2NaH_5[(Ru(OH))_2O(W_5O_{18})_2]·18H_2O$ (denoted as **Ru2-(W5)$_2$**), which incorporated a smaller POM unit, $\{W_5O_{18}\}$. This synthesis used GeO_2 and 2,5-pyridinedicarboxylic acid (although the specific roles of these substances remain unclear). The linear $\{(HO)Ru^{IV}–O–Ru^{IV}(OH)\}$ unit (Ru–O–Ru angle: 180.0°; O–Ru–O angles: 177.2° and 177.4°) connects two $\{W_5O_{18}\}$ POMs in an identical manner (Fig. 6(d)). In this combination mode, Ru–O(W) bond is around 2.000 Å. However, the yield of the POM is under 10% (8.42%, based on Ru) [80].

2.2.2 *Pseudo-sandwich-type POMs*

The POMs can also be interconnected by cation clusters. In 2009, Bi et al. successfully synthesized $KNa_6[(RuC_6H_6)AsW_9O_{34}]·17H_2O$ and $Na_7[(RuC_6H_6)PW_9O_{34}]·14H_2O$ through a simple one-pot procedure. This involved dissolving $[RuC_6H_6Cl_2]_2$ and $Na_8H[P/AsW_9O_{34}]$ in a 1:2 ratio in an acetate buffer, followed by heating to 80°C for 1 h. The resulting structure comprises two $[(RuC_6H_6)XW_9O_{34}]^{7-}$ subunits (X = As, P) that are linked by a Na cation cluster. This cluster contains both partially and fully occupied Na sites, giving rise to a novel pseudo-sandwich-type organo-Ru-POM. The Na cations are arranged in a plane that surrounds the crystallographic inversion center, positioned exactly halfway along the Na1···Na1' vector. The (RuC_6H_6) unit is coordinated via three Ru–O(W) bridges to the site of the trilacunary POM, while the vacant site remains unbound (Fig. 8(a)) [81]. This is the first example of a pseudo-sandwich-type organo-Ru(II) POM linked through a ring-like Na cation cluster.

Ruthenium ions can also be incorporated into the cation cluster. In 2013, Bi et al. synthesized an asymmetric sandwich-type structure by reacting $KNa_6[(RuC_6H_6)AsW_9O_{34}]·17H_2O$ with five different metal chloride salts or metal acetates at 80 °C. Upon removal of $Ru(C_6H_6)$, the POM consists of two distinct lacunary Keggin moieties: a trilacunary $\{B\text{-}\alpha\text{-}AsW_9O_{34}\}$ and a tetralacunary $\{B\text{-}\beta\text{-}AsW_8O_{31}\}$. A rhomb-like transition-metal cluster $\{M_4O_{16}\}$ (M = Ni^{II}, Zn^{II}) serves as the filling, resulting in the formation of another pseudo-sandwich-type POM with an asymmetric structure. Three (RuC_6H_6) units are linked through the W atoms of the POM and the transition metal M (M = Ni^{II}, Zn^{II}) occupying the central position. This arrangement results in a new POM with C_s symmetry (Fig. 8(b)). The terminal $Ru(C_6H_6)$ unit is coordinated to the $\{B\text{-}\beta\text{-}AsW_8O_{31}\}$ framework via three chemically nonequivalent oxygens (Ru3–O, 2.102–2.107 Å) (M = Zn^{II}). One O atom forms part of the $\{W_2O_{10}\}$ cluster in the $\{B\text{-}\beta\text{-}AsW_8O_{31}\}$ framework, while the remaining two O atoms belong to two distinct $\{W_3O_{13}\}$ triads derived from the same moiety. The other two (RuC_6H_6) units are attached to all μ_2-oxo bridges at the central belt, with Ru1–O distances ranging from 2.100 to 2.130 Å and Ru2–O distances from 2.12 to 2.15 Å [82]. These unique pseudo-sandwich-type POMs also exhibit remarkable catalytic properties owing to their structural features. These studies not only provide new avenues for synthesizing potentially functional materials but also hold

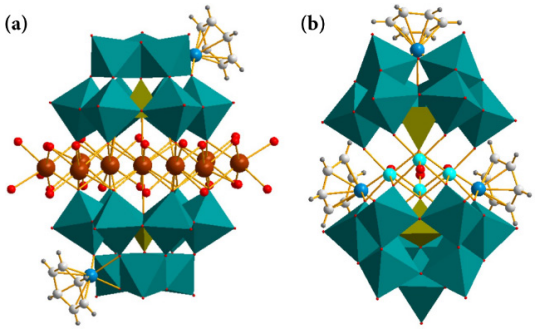

Figure 8 (a) The structure of $[(RuC_6H_6)AsW_9O_{34}]^{7-}$. (b) The structure of $[\{B\text{-}\alpha\text{-}AsW_9O_{34}\}\{B\text{-}\beta\text{-}AsW_8O_{31}\}\{M_4(OH)_2(H_2O)_2\}\{(RuC_6H_6)_3\}]^{6-}$ (M = Ni, Zn, Cu, Mn, Co). Color: W, teal; O, red; Ru, blue; C, white; H, grey; Na, brown; M, turquoise. (a) was reproduced from Ref. [81]. (b) was reproduced from Ref. [82].

promising prospects for practical applications in catalysis.

2.3 Other Ru-POMs structure

Other unique Ru–POMs with diverse structural features have been discovered in recent years. Some of these structures defy easy classification into typical POM categories. In this section, we will explore these atypical Ru-POMs, including those with single Ru atoms, dimeric structures, ring-like arrangements, and multiple Ru atoms.

2.3.1 Other Ru-POMs with single Ru atom

In 2003, Proust et al. synthesized $Na_4K_9[(PW_9O_{34})_2(cis\text{-}WO_2)(cis\text{-}RuL^{Me}{}_2)]\cdot 23H_2O$ (L^{Me} = 1,3-dimethylimidazolidine-2-ylidene) via air oxidation of $[RuL^{Me}{}_4Cl_2]$ with $K_{7-x}Na_x[PW_{11}O_{39}]^{14-}$. This POM comprises two α-A-$[PW_9O_{34}]^{9-}$ frameworks linked by a cis-$\{WO_2\}^{2+}$ group and a cis-$\{RuL^{Me}{}_2\}^{3+}$ fragment in a symmetrical arrangement. At the center of the POM, a K cation interacts with 10 oxygen atoms from the POM, with two additional water ligands completing its coordination sphere. Both the bridging tungsten and Ru atoms achieve six-coordination by linking to four oxo ligands—two from each $\{PW_9\}$ unit—and two terminal ligands (Fig. 9(a)) [83]. Some molybdenum/vanadium-containing POM have unique construction. Neumann's group loaded $Ru^{II}(DMSO)_3$ to $[Mo_7O_{24}]^{6-}$, getting $(NH_4)_4[Ru^{II}(DMSO)_3Mo_7O_{24}]\cdot 6.5H_2O$, which is a nearly pyramidal configuration, by the reaction of $(NH_4)_6Mo_7O_{24}\cdot 4H_2O$ and $Ru(DMSO)_4Cl_2$ in boiling water. The Ru center in a trigonal antiprismatic coordination mode is linked to three DMSO moieties via the sulfur atom and three oxygen atoms of the new heptamolybdate species (Fig. 9(b)) [84].

In 2010, Bi and Wu et al. achieved the first synthesis of a structurally characterized hepta-tungstovanadate fragment, $[HVW_7O_{28}Ru(DMSO)_3]^{6-}$, stabilized by the $Ru(DMSO)_3$ group. This was accomplished through the reaction of Na_2WO_4 and $NaVO_3$ with $Ru(DMSO)_4Cl_2$ in a ratio of 7:1:1 at 80 °C (pH = 6.0). The $Ru(DMSO)_3$ unit coordinates to the $\{VW_7O_{28}\}$ fragment via two Ru–O–W bonds and one Ru–O–V bond: two oxo groups originate from the tungsten–oxo framework (Ru–O distances: 2.064 and 2.104 Å), while one originates from the hetero group $\{VO_4\}$ (Ru–O distance: 2.100 Å) (Fig. 9(c)) [85]. In 2021, Jia and Zhang et al. synthesized Ru-POMs coordinated to phosphovanadomolybdate $[PMo_6V_3O_{32}]^{8-}$ via the reaction of cis-$[RuCl_2(DMSO)_4]$, $NaVO_3$, Na_2MoO_4, and NaH_2PO_4 at 80 °C. This POM comprises six octahedral $\{MoO_6\}$ units linked by a tetrahedral $\{PO_4\}$ unit. Four of the $\{MoO_6\}$ units share edges in pairs with square $\{VO_5\}$ pyramids, while two $\{MoO_6\}$ units from different pairs also share corners to coordinate with the remaining tetrahedral $\{VO_4\}$ unit. There are two types of connections. In one, the Ru center coordinates to three sulfur atoms from three DMSO ligands and three oxygen atoms from the POM framework to form $[Ru(DMSO)_3PV_3Mo_6O_{32}]^{6-}$ (denoted as **RuPMo6V3**) (Fig. 9(d)). The other type of connection involves the Ru center symmetrically coordinating with two frameworks to form $[Ru(PMo_6V_3O_{32})_2]^{14-}$ (denoted as **Ru(PMo6V3)$_2$**) (Fig. 9(e)). To synthesize this POM, the amount of metal salts used for **Ru(PMo6V3)$_2$** is twice that of **RuPMo6V3**, and the reaction time is extended from 1 to 4 h. Notably, the Ru–O(Mo) bond in **Ru(PMo6V3)$_2$** is shorter than that in **RuPMo6V3**, indicating enhanced stability [86]. These studies have expanded the family of organo–metal functionalized POMs.

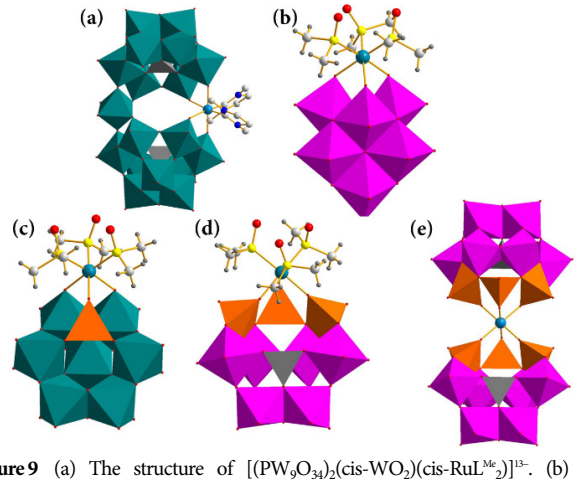

Figure 9 (a) The structure of $[(PW_9O_{34})_2(cis\text{-}WO_2)(cis\text{-}RuL^{Me}{}_2)]^{15-}$. (b) The structure of $[Ru^{II}(DMSO)_3Mo_7O_{24}]^{4-}$. (c) The structure of $[HVW_7O_{28}Ru(DMSO)_3]^{6-}$. (d) The structure of $[Ru(DMSO)_3PV_3Mo_6O_{32}]^{6-}$. (e) The structure of $[Ru(PMo_6V_3O_{32})_2]^{14-}$. Color: W, teal; O, red; Ru, blue; C, white; H, grey; N, dark blue; Mo, purple; V, orange; P dark grey. (a) was reproduced from Ref. [83]. (b) was reproduced from Ref. [84]. (c) was reproduced from Ref. [85]. (d) and (e) was reproduced from Ref. [86].

2.3.2 Other Ru-POMs with dimeric structures

The POMs could be combined by some fragment connected with Ru center to obtain new POMs. As the smallest bridge, O atom has been firstly found. In 1993 Finke's group synthesized $[O\{Ru^{IV}Cl(\alpha_2\text{-}P_2W_{17}O_{61})\}_2]^{16-}$ by the reaction of $K_{10}[\alpha_2\text{-}P_2W_{17}O_{61}]\cdot 15H_2O$ and $RuCl_3\cdot xH_2O$ at 90 °C. For the whole POMs, it could be considered as one of the two $[\alpha_2\text{-}P_2W_{17}O_{61}]^{10-}$ frameworks, which act as the tetradentate chelating and bridging ligands to the Ru atoms, rotated by 180° around the Ru atom to establish the structure (Fig. 10(a)). The Ru–O(Ru) bond is relatively short (1.773 Å), providing a stable connection between the two POMs. Both Ru ions are in the +IV oxidation state, while a Cl atom is also coordinated with each Ru atom [87]. In 2003, Sadakane and Higashijima synthesized $Cs_{11}[\{SiW_{11}O_{39}Ru^{IV/III}\}_2O]\cdot 12H_2O$ via the reaction of $K_8[\alpha\text{-}SiW_{11}O_{39}]\cdot 13H_2O$ and $Ru(acac)_3$ in a 1:1 ratio at 220 °C (oil bath temperature). In this POM, five Ru–O bonds originate from the lacunary Keggin structure, while a Ru–O(Ru) bond connects the two fragments (Fig. 10(b)). Notably, the two Ru ions exhibit different oxidation states (+IV and +III), resulting in unique electrochemical properties [37]. These studies paved the way for the synthesis of a new class of POMs.

In 2005, Proust's group used a fragment $\{WO_2\}$ to combine two POMs, $[PW_{11}O_{39}\{Ru(benzene)\}]^{4-}$, in which the organo-Ru(II) units are coordinated with two oxygen atoms of the POM and with an oxygen atom derived from the $\{WO_2\}^{2+}$ which acts as the bridge (Fig. 10(c)). The POM exhibits C_2 symmetry overall, featuring a binary axis positioned within the plane that bisects the $\{WO_2\}^{2+}$ group (the symmetry will lose when terminal ligand is not symmetric, such as p-cymene). The Ru–O(W) bond is similar to those in monosubstituted Ru-POMs with grafting mode, where the Ru–O distances fall in the range 2.00–2.14 Å, while the Ru–O–W angles are all within the range 150.3°–161.3° [39]. In 2012, Proust's group also found that the $\{W_2O_5\}$ fragment can combine two $[PW_{11}O_{39}\{Ru(benzene)\}]^{4-}$ in a similar way. The Ru ion is linked with two non-equivalent oxygen atoms from the lacuna of $[\alpha\text{-}PW_{11}O_{39}]^{7-}$, three DMSO ligands, and one oxo ligand from the $\{(WO_2(H_2O))_2O\}^{2+}$ bridge (Fig. 10(d)) [88]. In 2013, Kortz's group performed further investigations on POMs connected by $\{WO_2\}$, using a dihedral angle (φ) between the two planes P1(Ru1, X, X)

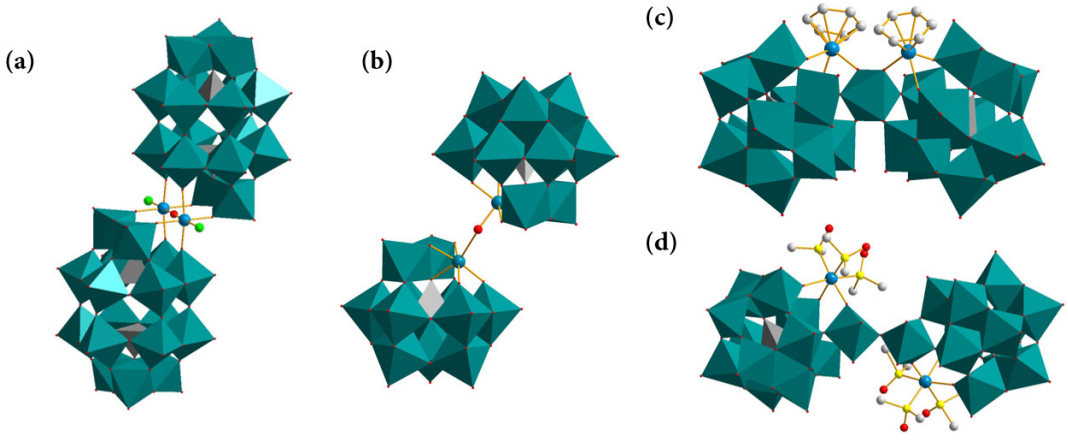

Figure 10 (a) The structure of $[O\{Ru^{IV}Cl(\alpha_2\text{-}P_2W_{17}O_{61})\}_2]^{16-}$. (b) The structure of $[\{SiW_{11}O_{39}Ru^{IV/III}\}_2O]^{11-}$. (c) The structure of $[\{PW_{11}O_{39}\{Ru(p\text{-cymene})\}\}_2\{WO_2\}]^{8-}$. (d) The structure of $[\{PW_{11}Ru(DMSO)_3\}_2(W_2O_5)]^{8-}$. Color: W, teal; O, red; Ru, blue; C, white; S, yellow; H, grey; P, dark grey; Si, light grey; Cl, green. (a) was reproduced from Ref. [87]. (b) was reproduced from Ref. [37]. (c) was reproduced from Ref. [39]. (d) was reproduced from Ref. [88].

and P2(Ru2, X, X) (66.9°–70.8°) (X = Ge, Si, and B) to describe the structure. The smallest angle was observed when X = Ge [89].

Regarding the synthesis of these Ru-POMs, they are all directly synthesized via the reaction of $[Ru(C_6H_6)Cl_2]_2$ and their corresponding POMs precursor (Table 3, entries 3–12). The formation ratio of monomeric to dimeric species was found to be directly influenced by the size of the arenes, where larger arenes hindered the formation of dimeric species. However, the primary factor contributing to a higher ratio of dimeric species is not the utilization of arenes with smaller size, but the reduction in the pH of the reaction situation. Especially, there are two routes for synthesizing $[\{PW_{11}Ru(DMSO)_3\}_2(W_2O_5)]^{8-}$, from $[P_2W_{20}O_{70}(H_2O)_2]^{10-}$ or from $[\alpha\text{-}PW_{11}O_{39}]^{7-}$, they all react at low pH (pH= 3). Importantly, the dimeric POMs connected by fragments tend to be synthesized under milder conditions and exhibit higher yields compared to those connected by single O atoms (Table 3). It is worth noting that these dimeric POMs also serve as crucial components in organo-Ru-POMs.

2.3.3 *Ru-POMs with ringlike structures*

In recent years, some Ru-POMs with ringlike structures have been synthesized. It should be noted that the "ring-like" is refer to the structures of Ru-POMs with a cavity that are constructed by at least one Ru atom. Niu and Wang et al. have made great contributions in this field. In 2018, Niu and Wang et al. successfully synthesized $[H_2N(CH_3)_2]_{14}[As_4W_{40}O_{140}\{Ru_2(CH_3COO)\}_2]\cdot 22H_2O$ (denoted as **$(Ru2)_2As4W40$**) through the reaction of $Na_2WO_4\cdot 2H_2O$, $NaAsO_2$, and $RuCl_3$ in a specific molar ratio of 7.7:1.1:1.0. The reaction was performed in a sodium acetate buffer solution (pH = 4.3) in the presence of dimethylamine hydrochloride and was heated to 150 °C for 24 h to obtain the product. Notably, the acetate buffer solution and the countercation were instrumental in this synthetic process. The unique structural arrangement features two diametrically opposed Ru atoms brought into close proximity, each coordinated to a {CH_3OO} group in a (μ_2-η^1:η^1) mode. Both Ru atoms complete their coordination sphere by bonding to two μ_2-O atoms from the {AsW_9} fragment (Ru–O(W), 1.979–2.067 Å), two μ_2-O atoms from two octahedral {WO_6} units (Ru–O(W), 1.995–2.022 Å), one μ_2-O atom from the {CH_3OO} group (Ru–O(C), 2.105–2.11 Å), and one As atom from the {AsW_9} group (Fig. 11(a)). Furthermore, in the {$Ru_2(CH_3COO)$} segment, the Ru···Ru distance is 5.9147 Å. The POM $[As_4W_{40}O_{140}\{Ru_2(CH_3COO)\}_2]^{14-}$ comprises a cyclic

Table 3 The synthesis methods of Ru-POMs which connected by non-Ru group

Entry	Formula	Ru source	Temp. (°C)	pH	Yield	Published year
1	$K_{15}H[O\{Ru^{IV}Cl(\alpha_2\text{-}P_2W_{17}O_{61})\}_2]$ [87]	$RuCl_3\cdot xH_2O$	90	—	11%–16%	1993
2	$Cs_{11}[\{SiW_{11}O_{39}Ru^{IV/III}\}_2O]\cdot 12H_2O$ [37]	$Ru(acac)_3$	220	—	12%	2003
3	$K_8[\{PW_{11}O_{39}\{Ru(p\text{-cymene})\}\}_2\{WO_2\}]$ [39]	$[Ru(p\text{-cymene})Cl_2)_2$	40	—	50%	2005
4	$K_7H[\{PW_{11}O_{39}\{Ru(toluene)\}\}_2\{WO_2\}]$ [39]	$[Ru(toluene)Cl_2]_2$	—	—	6%	2005
5	$K_8[\{PW_{11}Ru(DMSO)_3\}_2(W_2O_5)]\cdot 12H_2O$ [88]	fac- $[RuCl_2(DMSO)_3(DMSO)]$	—	3	32%	2012
6	$Cs_{8-x}K_x[\{PW_{11}O_{39}Ru(p\text{-cymene})\}_2\{WO_2\}]$ [88]	$[Ru(p\text{-cymene})Cl_2]_2$	—	3	—	2012
7	$K_{10}[\{Ru(benzene)\}_2(\alpha\text{-}SiW_{11}O_{39})_2WO_2]\cdot 19H_2O$ [89]	$[Ru(C_6H_6)Cl_2]_2$	85	4/5.5 (after cooling)	39%	2013
8	$K_{12}[\{Ru(p\text{-cymene})\}_2(\alpha\text{-}SiW_{11}O_{39})_2WO_2][SiW_{12}O_{40}]_{0.5}\cdot 28H_2O$ [89]	$[Ru(p\text{-cymene})Cl_2]_2$	80	4	22%	2013
9	$K_{10}[\{Ru(benzene)\}_2(\alpha\text{-}GeW_{11}O_{39})_2WO_2]\cdot 19H_2O$ [89]	$[Ru(C_6H_6)Cl_2]_2$	80	3.9/5 (after cooling)	58%	2013
10	$K_{10}[\{Ru(p\text{-cymene})\}_2(\alpha\text{-}GeW_{11}O_{39})_2WO_2]\cdot 23H_2O$ [89]	$[Ru(pcymene)Cl_2]_2$	80	4/4.5 (after cooling)	47%	2013
11	$K_{10}[\{Ru(benzene)\}_2(\alpha\text{-}HBW_{11}O_{39})_2WO_2]\cdot 33H_2O$ [89]	$[Ru(C_6H_6)Cl_2]_2$	80	4/5.1 (after cooling)	20%	2013
12	$K_{10}[\{Ru(p\text{-cymene})\}_2(\alpha\text{-}HBW_{11}O_{39})_2WO_2]\cdot 20H_2O$ [89]	$[Ru(p\text{-cymene})Cl_2]_2$	80	4	16%	2013

$[As_4W_{40}O_{140}]^{28-}$ ($\{As_4W_{40}\}$) framework that encapsulates two $[Ru_2(CH_3COO)]^{7+}$ segments in its internal cavities. The $\{As_4W_{40}\}$ unit is constructed from four trivacant $[B\text{-}\alpha\text{-}AsW_9O_{33}]^{9-}$ ($\{AsW_9\}$) fragments, which are interconnected by the addition of four octahedral $\{WO_6\}$ units. Each pair of adjacent $\{AsW_9\}$ fragments is linked by an octahedral $\{WO_6\}$ unit via two μ_2-O atoms. The S2 sites are defined by the oxygen atoms remaining in each octahedral $\{WO_6\}$ unit, supplemented by two oxygen atoms from each $\{AsW_9\}$ fragment. The central S1 site, on the other hand, is defined by the eight oxygen atoms remaining from four octahedral $\{WO_6\}$ units. In the POM, the four lacunary S2 sites of $\{As_4W_{40}\}$ are occupied by four Ru atoms, while the central S1 site remains vacant [90].

Moreover, in 2021, the synthesis of $K_5NaH_{10}[\{Ru_4(H_2O)_n\}(WO_2)_4(AsW_9O_{33})_4]\cdot mH_2O$ was achieved through the reaction of $Na_{28}[As_4W_{40}O_{140}]$ and $RuCl_3$ in a sodium acetate buffer solution (pH = 4.5), followed by heating to 160 °C for 72 h. Subsequently, in 2022, two ring-like $\{Ru_4\}$ POMs were synthesized: $K_5Na_9H_8[Ru_2(WO_2)_4(AsW_9O_{33})_4]\cdot 50H_2O$ and $Na_{13}H_5[Ru_4(H_2O)_2(Cl)_2(WO_2)_4(AsW_9O_{33})_4]\cdot 43H_2O$. These compounds exhibited structural similarities and were synthesized via the reaction of $K_{14}[As_2W_{19}O_{67}(H_2O)]$ (denoted as As2W19) and $RuCl_3$ in acetate buffer solutions (pH = 4 and 5, respectively), followed by heating to 160 and 150 °C for 72 h. $K_5Na_9H_8[Ru_2(WO_2)_4(AsW_9O_{33})_4]\cdot 50H_2O$ contains four trivacant $\{B\text{-}\alpha\text{-}AsW_9O_{33}\}$ POMs and one quadrate-shaped $\{Ru_2(WO_2)_4\}$ cluster (Fig. 11(b)). The quadrate-shaped $\{Ru_2(WO_2)_4\}$ cluster is composed of four $\{WO_2\}$ segment and four Ru^{III} sites in a structured manner. Each Ru atom is coordinated with two oxygen atoms derived from the trivacant $\{AsW_9\}$ framework (Ru–O(W), 2.160–2.224 Å) to form the basic plane of the POM, and two oxygen atoms derived from two adjacent $\{WO_6\}$ units (Ru–O(W), 2.170–2.195 Å), one As atom derived from the $\{AsW_9\}$ fragment to establish itself in an unordinary penta-coordination mode. The structure of $K_5NaH_{10}[\{Ru_4(H_2O)_n\}(WO_2)_4(AsW_9O_{33})_4]\cdot mH_2O$ is similar to the two POMs above, but all the terminal ligands are aqua ligands. Upon heat treatment of these POMs at 100 and 200 °C, their structures remained intact, except for variations in the number of aqua ligands. Upon heating to 200 °C, the Ru–O(W) bond lengths between the Ru atoms and the $\{AsW_9\}$ framework increase from 2.16 to 2.24 Å, while the O–Ru–O(W) angles in the quadrate-shaped $\{Ru_2(WO_2)_4\}$ cluster decrease from 90.087° to 87.106°. However, further heating to 300 °C induces a structural transformation, resulting in the formation of $K_5Na_9H_8[Ru_2(WO_2)_4(AsW_9O_{33})_4]\cdot 50H_2O$. $Na_{13}H_5[Ru_4(H_2O)_2(Cl)_2(WO_2)_4(AsW_9O_{33})_4]\cdot 43H_2O$ comprises four trivacant $\{B\text{-}\alpha\text{-}AsW_9O_{33}\}$ POMs and a crown-shaped $\{Ru_4(H_2O)_2(Cl)_2(WO_2)_4\}$ cluster (Fig. 11(c)). The $\{Ru_4(H_2O)_2(Cl)_2(WO_2)_4\}$ cluster is a unique eight-metal cluster consisting of four $\{WO_2\}$, two $\{Ru(H_2O)\}$, and two $\{Ru(Cl)\}$ units arranged in a specific manner. Notably, this crown-shaped $\{Ru_4(H_2O)_2(Cl)_2(WO_2)_4\}$ cluster is encapsulated by four $\{B\text{-}\alpha\text{-}AsW_9O_{33}\}$ units, which form a ship-shaped framework. In the central eight-metal cluster, two crystallographically independent Ru(III) ions exhibit a distorted octahedral geometry, displaying a tapered six-coordinate mode. The Ru1 atom is coordinated in a manner similar to that observed in the quadrate-shaped $\{Ru_2(WO_2)_4\}$ cluster, with two oxygen atoms from the $\{AsW_9\}$ framework (Ru–O, 2.073 Å) forming the basal plane of the POM, two oxygen atoms from two adjacent $\{WO_6\}$ units (Ru–O, 2.032 Å), one As atom from an $\{AsW_9\}$ fragment, and an additional terminal oxygen atom from a water ligand. The Ru2 atom also adopts a similar coordination mode but with slight variations in bond lengths, potentially influenced by the nature of the terminal ligands, with two oxygen atoms from the $\{AsW_9\}$ fragment (Ru–O, 2.022 Å) forming the basal plane, two oxygen atoms from two adjacent $\{WO_6\}$ units (Ru–O, 1.978 Å), one As atom from the $\{AsW_9\}$ fragment, and one chlorine atom, which possesses high electronegativity. Notably, all three POMs exhibit high symmetry, crystallizing in the tetragonal crystal system with the space group $I\bar{4}$. This structural feature provides increasingly exposed active sites for catalytic applications [17, 91].

In 2022, a unique POM, $K_6H[\{Ru_2Cl(H_2O)(CH_3COO)_2\}\{WO\text{-}H_2O)\}_2(PW_9O_{34})_2]\cdot 14H_2O$, was synthesized via the reaction of $K_{14}[P_2W_{19}O_{69}(H_2O)]\cdot 24H_2O$ and $RuCl_3$ in acidic condition (pH= 3.5–4.2) at room temperature with the help of carboxylic acid ligand which is then heated to 120 °C for 72 h to get the product. Different from the POMs inserted with ringlike Ru groups, this ringlike Ru group works as a bridge to connect the two POMs fragments to form the Ru-POMs structures with a cavity. In the center of the POM, there is a trapezoid cluster established with two W atoms derived from two $[WO(H_2O)]^{4+}$ units and two Ru atoms from the central $[Ru_2Cl(H_2O)(CH_3COO)_2]^{3+}$ group. It is amazing that in the distorted pyramidal $[Ru_2Cl(H_2O)(CH_3COO)_2]^{3+}$ group, the Ru^{III} ions are all penta-coordinated, which is coordinated with two μ_2-O atoms from $\{PW_9\}$ (Ru–O(W), 1.971–1.982 Å), two carboxyl oxygen atoms from the $[CH_3COO]^-$ ligand and a chlorine atom or an oxygen atom derived from water ligand (Fig. 11(d)). In addition, Ru1 and Ru2 combine C1, C3, O1, O2, O3, and O4 to form a "boat" geometry with a distance of 2.340 Å between Ru1 and Ru2 sites [92]. This serves as an exemplary illustration of how to build structurally robust POMs through the design and adjustment of building blocks and organic ligands featuring diverse coordination modes. Moreover, such a cavity in ringlike Ru-POMs may ultimately facilitate the exploration of their potential catalytic applications. However, these Ru-POMs are still in low yields, which are synthesized at high temperatures with a controlled pH value around 4 to get the product. How to effectively and selectively

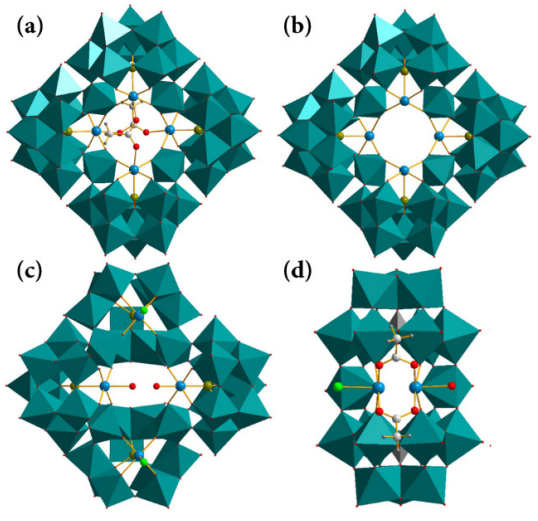

Figure 11 (a) The structure of $[As_4W_{40}O_{140}\{Ru_2(CH_3COO)\}_2]^{14-}$. (b) The structure of $[Ru_2(WO_2)_4(AsW_9O_{33})_4]^{22-}$. (c) The structure of $[Ru_4(H_2O)_2(Cl)_2(WO_2)_4(AsW_9O_{33})_4]^{18-}$. (d) The structure of $[\{Ru_2Cl(H_2O)(CH_3COO)_2\}\{WO\text{-}(H_2O)\}_2(PW_9O_{34})_2]^{7-}$. Color: W, teal; O, red; Ru, blue; C, white; H, grey; P, dark grey; Cl green; As dark yellow. (a) was reproduced from Ref. [90]. (b) and (c) were reproduced from Ref. [17]. (d) was reproduced from Ref. [92].

prepare this unique ring-like Ru-POMs structures is worth further studying.

2.3.4 Other Ru-POMs with multi Ru atoms

In 2008, Kortz et al. reported the synthesis of a heteropoly blue via a sequential addition of $NaVO_3$, NaH_2PO_4, and cis-$Ru(DMSO)_4Cl_2$ to a sodium acetate buffer (pH = 4.8), followed by heating to 50 °C. This compound exhibits a unique, open-framework structure composed of two octahedral $\{Ru^{III}O_6\}$ units, two octahedral $\{V^{IV}O_6\}$ units, fourteen $\{V^{V}O_5\}$ square-pyramids, eight tetrahedral $\{V^{V}O_4\}$ units, and two tetrahedral $\{PO_4\}$ units, all interconnected directly through their edges and corners. Additionally, six $Ru^{II}(DMSO)_3$ groups adorn its outer surface. These six external $Ru^{II}(DMSO)_3$ groups are exclusively attached to vanadium centers via three Ru–O(V) bonds. The three Ru^{II} atoms adopt octahedral fac-O_3S_3 coordination, with Ru–O bond lengths ranging from 2.025 to 2.086 Å (Fig. 12(a)) [93].

In 2019, Niu and Wang et al. synthesized a trimeric Ru-substituted POM, $Rb_{10}K_3H_6[SeO_3(H_9Ru^{IV}_{5.5}W_{30.5}O_{114})]Cl_3{\cdot}48H_2O$, via the reaction of $Na_2WO_4{\cdot}2H_2O$, SeO_2, and $RuCl_3$ at 80 °C (pH = 5). This POM features a $\{SeO_3Ru_3\}$ core anchored to a $\{Ru_{2.5}W_{30.5}\}$ wheel, exhibiting C_{3v} symmetry with the central Se atom aligned along the C_3 symmetry axis. In the $\{Ru_{2.5}W_{30.5}\}$ assembly, three equivalent monovacant iso-POT $\{H_3Ru_{0.83}W_{10.17}O_{38}\}$ units are interconnected via corner-shared Ru/W–O–Ru/W bridges, forming a cyclic cluster (Fig. 12(b)). In this POM, all remaining vacant sites are occupied by three octahedral $\{RuO_6\}$ units, with the $[SeO_3]^{2-}$ ion positioned centrally. From a top-down perspective, these components further assemble to form a clover-leaf-shaped $\{SeO_3Ru_3\}$ unit. Notably, the Ru6 and W6 atoms exhibit statistical disorder, with the Ru6 atom occupying 42.2% and the W6 atom occupying 57.8% of these respective positions. This POM represents not only the first example of inorganic Ru–POMs based on isopolytungstates but also a rare instance of SeO_3^{2-}-bridged trimeric structures among all known trimeric architectures based on Keggin-type or Keggin-like POMs [94]. In 2022, Niu et al. synthesized **Ru2-(W5)$_2$** by adjusting the final pH from 4.3 to 6.8. This modification led to the formation of a different POM, $Na_{5.5}H_{6.5}[(W_5O_{18})(Ru_2W_8O_{31})]{\cdot}28H_2O$ (Fig. 12(c)). This POM contains a unique $[Ru_2W_8O_{31}]^{6-}$ subunit fused with a mono-lacunary Lindqvist-type $[W_5O_{18}]^{6-}$ unit, resulting in an external framework similar to that of **Ru2-(W5)$_2$**. The unprecedented $[Ru_2W_8O_{31}]^{6-}$ anion adopts a boat-like conformation featuring a slightly distorted $\{W_8\}$ ring that fully encapsulates the central {Ru–O–Ru} unit. Notably, the central {Ru–O–Ru} unit exhibits high linearity but with slight distortions attributed to the unique coordination environment imposed by the surrounding $\{W_8\}$ ring (Ru–O(Ru) bond: 1.763–1.794 Å, Ru–O–Ru angle: 174.8°, and O–Ru–O angles of 175.9° and 177.3°). Each Ru atom in the $[Ru_2W_8O_{31}]^{6-}$ subunit adopts a distorted octahedral geometry coordinated exclusively by bridging oxygen atoms. The Ru–O bond lengths range from 1.763 to 2.050 Å, which are comparable to those observed in other Ru^{IV}-containing POMs. The $\{W_4\}$ building block is constructed by linking four octahedral $\{WO_6\}$ units through their edges to form a $\{W_4\}$ semicircle. Subsequently, these $\{W_4\}$ fragments are joined together via two corners, ultimately resulting in the formation of the $\{W_8\}$ ring. Notably, the four W atoms in each $\{W_4\}$ semicircle lie in a quasi-planar arrangement, although they are not strictly coplanar owing to the influence of the Ru–O–Ru bond, which deviates from linearity [80].

In 2021, Niu and Wang et al. synthesized $Na_3[NaM_{12}O_{42}(Ru(DMSO)_3)_4]{\cdot}13H_2O$ (M = Mo and W) (Fig. 13). These new Silverton-type archetypes $[NaM_{12}O_{42}]^{11-}$ (M = Mo, W) are effectively stabilized by four $\{Ru(DMSO)_3\}^{2+}$ groups, while the central Na^+ ions in the $\{NaM_{12}O_{42}\}$ archetype exhibit regular dodecahedral coordination environments. The synthesis of $Na_3[NaM_{12}O_{42}(Ru(DMSO)_3)_4]{\cdot}13H_2O$ (M = Mo and W) involves acidifying the substrate $Na_2MO_4{\cdot}2H_2O$ (M = Mo, W) in concentrated hydrochloric acid. Subsequently, $RuCl_3$ and DMSO are added to the solution, which is then adjusted to pH 5.6 using NaOH. The reaction mixture undergoes a multistep heating process, including 3 h at 80 °C followed by 24 h at 120 °C, to yield the desired product [95].

In 2023, Niu et al. synthesized $Cs_2Na_4H_7[(SbW_9O_{33})_6\{Ru(H_2O)_5\}(RuCl_3)(RuO_6)_2\{W(H_2O)\}_6(WO)_4\{WO_2(H_2O)\}_2\{WO_2(H_2O)_2\}_2\{WO_5(H_2O)\}]{\cdot}43H_2O$ (Fig. 14(a)) by mixing $Na_2WO_4{\cdot}2H_2O$, Sb_2O_3, and $RuCl_3$ at 200 °C (with pH adjusted to 6, and then to 3 after adding $RuCl_3$) for 3 days [96]. Its structure bears similarities to the large tungstoarsenate $[As^{III}_6W_{65}O_{217}(H_2O)_7]^{26-}$ (Fig. 14(b)). The POM consists of four inner $\{\beta\text{-}AsW_9O_{33}\}$ and two outer $\{\alpha\text{-}AsW_9O_{33}\}$ segments, which are interconnected by a total of eleven octahedral $\{WO_6\}$ units sharing corners. Accordingly, the large tungstoarsenate is formulated as $[(\beta\text{-}AsW_9O_{33})_4(\alpha\text{-}AsW_9$

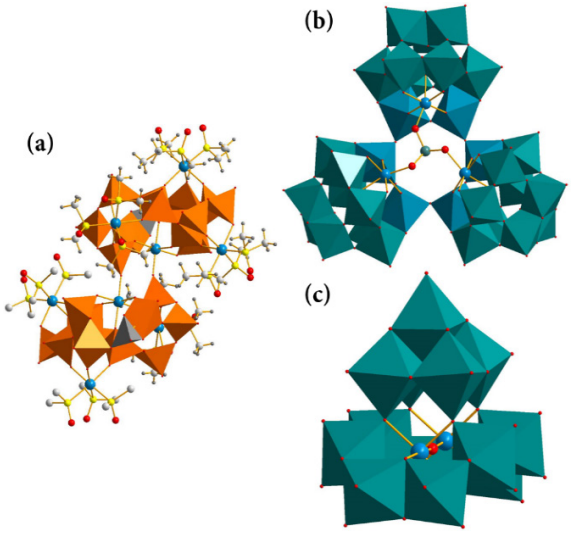

Figure 12 (a) The structure of $[\{[Ru^{II}(DMSO)_3]_3PV^{V}_{11}V^{IV}Ru^{III}O_{37}(OH)_3\}_2]^{8-}$. (b) The structure of $[SeO_3(H_9Ru^{IV}_{5.5}W_{30.5}O_{114})]^{16-}$. The color mixed by Ru and W means a uncertain component between Ru and W. (c) The structure of $[(W_5O_{18})(Ru_2W_8O_{31})]^{11-}$. Color: V, orange; W, teal; O, red; Ru, blue; C, white; H, grey; Se, sea green; Aqua, Ru or W. (a) was reproduced from Ref. [93]. (b) was reproduced from Ref. [94]. (c) was reproduced from Ref. [80].

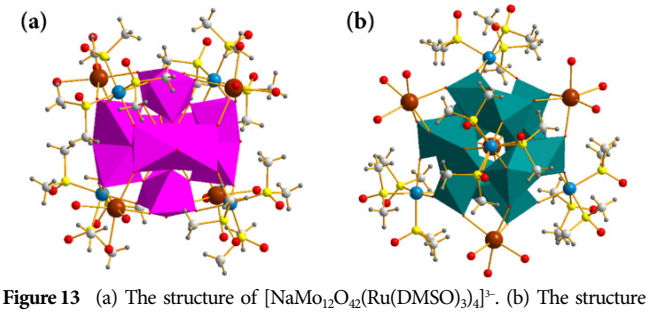

Figure 13 (a) The structure of $[NaMo_{12}O_{42}(Ru(DMSO)_3)_4]^{3-}$. (b) The structure of $[NaW_{12}O_{42}(Ru(DMSO)_3)_4]^{3-}$. Color: Mo, purple; W, teal; O, red; Ru, blue; C, white; H, grey; Na, brown. (a) and (b) were reproduced from Ref. [95].

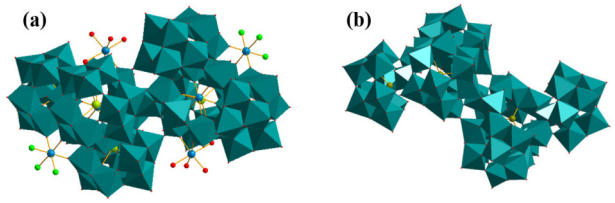

Figure 14 (a) The structure of $[(SbW_9O_{33})_6\{Ru(H_2O)_5\}(RuCl_3)(RuO_6)_2\{W(H_2O)\}_6(WO)_4\{WO_2(H_2O)\}_2\{WO_2(H_2O)_2\}_2\{WO_5(H_2O)\}]^{13-}$. (b) The structure of $[As^{III}_6W_{65}O_{217}(H_2O)_7]^{26-}$. Color: W, teal; O, red; Ru, blue; Sb, lime; As, dark yellow; Cl, green. (a) was reproduced from Ref. [96]. (b) was reproduced from Ref. [97].

$O_{33})_2(WO_2)_4(WO(H_2O))_6WO_5(H_2O)]^{26-}$. The arrangement of the six (AsW_9O_{33}) subunits resembles the chair conformation of cyclohexane [97]. The newly synthesized POMs can be viewed as incorporating an eighteen-metal cluster (comprising six Ru atoms and twelve W atoms) into the large tungstoarsenate framework [96].

In the synthesis of Ru-POMs, the Ru sources can be categorized into $Ru(L)_xCl_{3-x}$ and $RuCl_3{\cdot}xH_2O$. For Ru-POMs with open structures, the choice of Ru source directly influences the target products with specific ligands. The synthesis methods for these open-structured Ru-POMs are not limited to hydrothermal conditions. In contrast, most Ru-POMs with closed structures are synthesized from $RuCl_3{\cdot}xH_2O$, often under conditions of high temperature or low pH, or a combination of both. Using a suitable cation to precipitate the Ru-POM products has proven effective in synthesizing the basic Ru-POMs discussed in Section 2.1. Together with their low yields, it is still challenging to develop better and simpler methods to increase the yield and selectivity of Ru-POMs.

3 Properties and applications of Ru-POMs

Many Ru-POMs have shown desired properties and applications in many fields, especially in the field of real catalysis. In this section, we will compare the properties of Ru-POMs and introduce their applications.

3.1 Electrocatalyst

3.1.1 Electrochemical properties

Variations in the structure of POMs induce changes in their redox activity. Furthermore, the specific combination of ligands and Ru also influences the redox behavior of POMs. For instance, the relatively simple $[Si/PW_{11}O_{39}Ru^{III}H_2O]^{n-}$ complex exhibits three reversible redox couples corresponding to $Ru^{III/II}$, $Ru^{IV/III}$, and $Ru^{V/IV}$ (Fig. 15(a)) [23, 35]. Notably, the $Ru^{III/II}$ reduction potential of 0.21 V is lower than that observed in other $[PW_{11}O_{39}M^{III/II}H_2O]$ complexes (M = Fe, E = 0.28 V; M = Mn, E = 1.12 V; M = Co, E = 1.39 V; E = redox potential). Substitution of an electron-donating group for the ligand stabilizes $Ru^{III/II}$. Consequently, Ru typically assumes the +2 oxidation state in these POMs. Table 4 presents several reversible redox couples of $Ru^{III/II}$ with various ligands. However, certain nucleophilic ligands, such as $NPPh_3$ and Cl, tend to stabilize higher valence states. For $NPPh_3$, cyclic voltammetry (CV) reveals two quasi-reversible waves at 0.31 V and −0.71 V vs. CE, corresponding to the $Ru^{VI/V}$ and $Ru^{V/IV}$ redox couples, respectively. In the case of Cl, CV shows one reversible redox wave ($E_{1/2}$ = 0.287 V vs. $Ag/AgNO_3$) and one irreversible wave ($E_{1/2}$ = 1.208 V vs. $Ag/AgNO_3$), tentatively assigned to the $Ru^{IV/III}$ and $Ru^{V/IV}$ couples, respectively. These results are depicted in Fig. 15(b). As shown in Fig. 15(b), the redox couples are also influenced by the choice of cations, such as TBA^+. The $[PW_{11}O_{39}Ru^{III}H_2O]^{n-}$ species exhibits only two redox peaks ($E_{1/2}$ = 0.542 and 1.339 V vs. $Ag/AgNO_3$), corresponding to the $Ru^{III/II}$ and $Ru^{IV/III}$ couples [44, 51]. The grafting binding mode further stabilizes the $Ru^{III/II}$ redox pair in this manner. The simultaneous presence of three strongly bound DMSO ligands at the Ru(II) center likely enhances the stabilization described above and shifts all Ru redox potentials beyond the accessible range [38]. Notably, $Cs_6[PW_{11}O_{39}\{Ru^{II}(benzene)(H_2O)\}]$ does not exhibit any discernible redox couple in CVs prior to calcination at 450 °C, at which point the ligands are exchanged for CO [47]. Dawson-type POMs exhibit a similar behavior to Keggin-type POM isomers (Fig. 15(c)) [56]. In Krebs' POMs, the Ru ions are also attached to the POM in the grafting mode. However, these POMs exhibit a $Ru^{IV/III}$ reversible redox couple stemming from Ru centers coordinated with the tungsten–oxo fragment. The peak at 1.00 V is ascribed to a one-electron process, corresponding to the $Ru^{III/II}$ couple originating from Ru(bpy). The peak at 0.24 V is also attributed to a one-electron process, but it is assigned to the $Ru^{IV/III}$ couple originating from Ru centers coordinated with the tungsten–oxo fragment. This difference may arise from the distinct binding mode of DMSO (Fig. 15(d)) [71]. In monosubstituted POMs with multiple Ru ions, all exhibit a $Ru^{III/II}$ oxidation potential that is higher than that of other Ru-containing POMs. This phenomenon can be attributed to the outer Ru (Figs. 15(e) and 15(f)) [65–67].

For dimeric POMs connected by small groups, such as $\{WO_2\}$, the redox behavior is not clearly manifested, and they primarily exhibit the character of $[\alpha\text{-}SiW_{12}O_{40}]^{4-}$ [89]. However, in $[\{SiW_{11}O_{39}Ru^{IV/III}\}_2O]^{11-}$, where the POMs are directly linked by an oxygen atom, the two Ru ions exhibit mixed valency. The CV of this complex in acidic (pH 1.5) solution reveals one oxidative peak and two reduction peaks with approximate current ratios of 1:1:2. These peaks can be assigned to the Ru(IV)–O–Ru(IV)/Ru(IV)–O–Ru(III), Ru(IV)–O–Ru(III)/Ru(III)–O–Ru(III), and Ru(III)–O–Ru(III)/Ru(II)–O–Ru(II) redox reactions, respectively (Fig. 16(a)) [37]. In sandwich-type POMs and other complex structures, Ru ions generally adopt the +4 oxidation state. In **Ru2-PW11**, for the linear $\{(HO)Ru^{IV}–O–Ru^{IV}(OH)\}$ group bridged by two POMs $\{PW_{11}O_{39}\}$, two redox peaks are observed (Fig. 16(b)). The first couple at −0.02 V likely involves a two-electron transfer and can be attributed to the Ru^{IV}_2/Ru^{III}_2 process, while the second couple at +0.65 V corresponds to a single-electron transfer and is therefore assigned to the $Ru^{V}Ru^{IV}/Ru^{IV}_2$ couple [77]. Furthermore, in **Ru4-SiW10**, at pH 1.0, two oxidation peaks are observed at approximately 940 and 1050 mV during a scan from the resting potential (800 mV) to positive potentials. During the reverse scan, a reduction peak at approximately 750 mV and another at approximately 965 mV emerge, indicative of two $Ru^{V/IV}$ couples. In the region below the resting potential, three reduction peaks appear at 530, 370, and −170 mV, with their corresponding re-oxidations at 640, 480, and 290 mV, consistent with three $Ru^{IV/III}$ reductions. Furthermore, a peak pertaining to the fourth $Ru^{IV/III}$ reduction near −350 mV coincides with a peak for $W^{VI/V}$ reduction at approximately −460 mV. This suggests that in the electrochemical process, two of the Ru^{IV} centers undergo oxidation to Ru^{V}, while all four Ru^{IV} centers are capable of being reduced to Ru^{III}. As the pH increases, the rest potentials are lower, but the CV traces are less informative owing to the complex acid–base equilibria exhibited by the Ru complexes (Fig. 16(c)) [16].

The electrochemical performances of the other POMs with

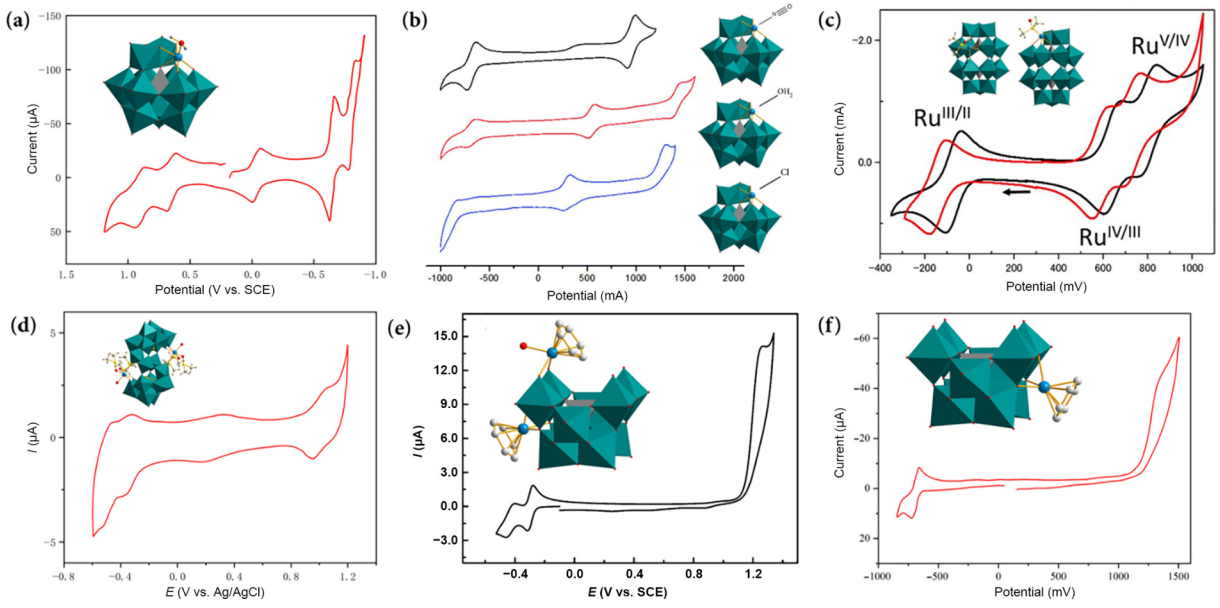

Figure 15 (a) CV at a pyrolytic graphite electrode of 0.68 mM **Ru-PW11** (supporting electrolyte, 0.3 M Na_2SO_4 adjusted to pH 2.0). (b) CVs of (n-$Bu_4N)_4[PW_{11}O_{39}Ru^{II}(NO)]$ (black), (n-$Bu_4N)_4[PW_{11}O_{39}Ru^{III}(H_2O)]$ (red), and (n-$Bu_4N)_4[PW_{11}O_{39}Ru^{IV}Cl]$ (blue) in acetonitrile with 0.1 M $TBABF_4$ as supporting electrolyte vs. Ag/$AgNO_3$ (scan rate 100 mV·s^{-1}). (c) CVs of (black) $[\alpha_1\text{-}P_2W_{17}O_{61}Ru^{III}(H_2O)]^{7-}$ and (red) $[\alpha_2\text{-}P_2W_{17}O_{61}Ru^{III}(H_2O)]^{7-}$ in 0.2 M Na_2SO_4 + H_2SO_4 (pH 3.0). POM concentration: 2.5 × 10^{-4} M. Scan rate: 10 mV·s^{-1}. Working electrode: EPG; counter electrode: Pt; reference electrode: SCE. (d) CV of 0.5 mM $[Sb_2W_{20}Ru^{III}_2(H_2O)_2(DMSO)_6O_{68}]^{4-}$ in DMSO+H_2SO_4 at pH 2.5 at a bare GCE with scan rate 100 mV·s^{-1}. (e) CVs of 2 × 10^{-4} M $[\{Ru(C_6H_6)(H_2O)\}\{Ru(C_6H_6)\}(\gamma\text{-}GeW_{10}O_{36})]^{4-}$ in 1 M HCl (pH 0) medium. The working electrode was glassy carbon and the reference electrode was SCE. The scan rate was 10 mV·s^{-1}. (f) CV of $Cs_6[\gamma\text{-}SiW_{10}O_{36}Ru(C_6H_6)]$ (1 mM) dissolved in acetate buffer (pH = 4.7). (a) is reprinted from the permission from Ref. [23], © Elsevier B.V. 1995. (b) is reprinted from the permission from Ref. [51], © The Royal Society of Chemistry 2015. (c) is reprinted from the permission from Ref. [56], © The Royal Society of Chemistry 2016. (d) is reprinted from the permission from Ref. [71], © Elsevier Inc. 2009. (e) is reprinted from the permission from Ref. [65], © American Chemical Society 2006. (e) is reprinted from the permission from Ref. [67], © WILEY-VCH Verlag GmbH & Co. KGaA, Weinheim 2018.

Table 4 Redox potentials of some of $[XW11O39Ru^{II}L)]^{4-/5-}$

	L	E ($Ru^{III/II}$, V vs. SCE)	Solution and pH
X = P	Me_2SO [13]	+0.33	Controlled by 0.5 M sulfate and 0.5 M 3,3-dimethylglutarate (plus 0.5 M NaCl) buffers for the pH ranges of 0–3 and 4–7, respectively.
	$(CH_2)_4SO$ [13]	+0.33	
	Ph_2SO [13]	+0.38	
	Me_2S [13]	+0.11	
	Me-cysteine [13]	+0.17	
	Maleic acid [13]	+0.63	
	Fumaric acid [13]	+0.63	
	Crotonic acid [13]	+0.48	
	1,4-Dihydroxybut-2-ene [13]	+0.41	
	Pyridine [13]	+0.03	
	NO [48]	+1.29 (vs. Ag/AgCl)	CH_3CN
X = Si	CO [42]	+0.495	0.5 M KH_2PO_4 (pH 4.5)

multiple Ru ions resemble those of the POMs described above; however, the valency can also be adjusted by changing the ligands. In the $[\gamma\text{-}SiW_{10}O_{38}\{RuN\}_2]^{6-}$, an irreversible reduction wave is observed at −0.23 V vs. Ag/AgCl, which can be attributed to a $\{Ru^{VI}N\}/\{Ru^{V}NH\}$ couple (Fig. 16(d)) [62]. The electrochemical properties of Ru–POMs with other unique structures discovered in recent years lack definitive patterns and will be discussed in the context of their applications, as needed.

3.1.2 *Electrocatalysis*

Ru-POMs exhibit remarkable electrocatalytic performance owing to the redox properties of the entire system and the electron transfer reaction mechanism influenced by the coordination environment of the incorporated Ru. They can catalyze the oxidation of DMSO, benzyl alcohol, nitrite, 5-hydroxymethyl-2-furancarboxylic acid, and water while also catalyzing the reduction of DMSO and nitrate. The electrochemical catalytic performance of Ru–POMs is closely related to their valence state.

In the case of the basic monosubstituted POM, **Ru-PW11**, the oxidation state of the Ru center enables the POM to catalyze the oxidation of benzyl alcohol to the corresponding aldehyde at potentials higher than 1.3 V. This process involves the initial oxidation of the Ru center from Ru^{IV} to Ru^{V}, which is then used to catalytically oxidize benzyl alcohol. However, at pH = 4, the system reaches a limiting plateau current of approximately 12 μA, corresponding to k = 30 $M^{-1}\cdot s^{-1}$ (k = reaction rate constant). Under the same conditions, **Ru-PW11** exhibits even lower activity toward 2-propanol (k = 9 $M^{-1}\cdot s^{-1}$) and methanol (k = 0.1 $M^{-1}\cdot s^{-1}$). Although **Ru-PW11** has the capability to catalyze alcohols to aldehydes, the rate constant of this reaction is too small to make the complexes attractive as catalysts for the electro-oxidations of alcohols [23]. When dissolved in solution or confined to the electrode surface, **Ru4-SiW10** demonstrates substantial catalytic activity in electro-oxidating methanol and ethanol at carbon electrodes. Across a broad pH range in both aqueous (including acidic, neutral, and alkaline environments) and alcoholic media, the oxidized states of **Ru4-SiW10** efficiently catalyze methanol and ethanol under all tested conditions by Bond and Zhang et al., which is attributed to

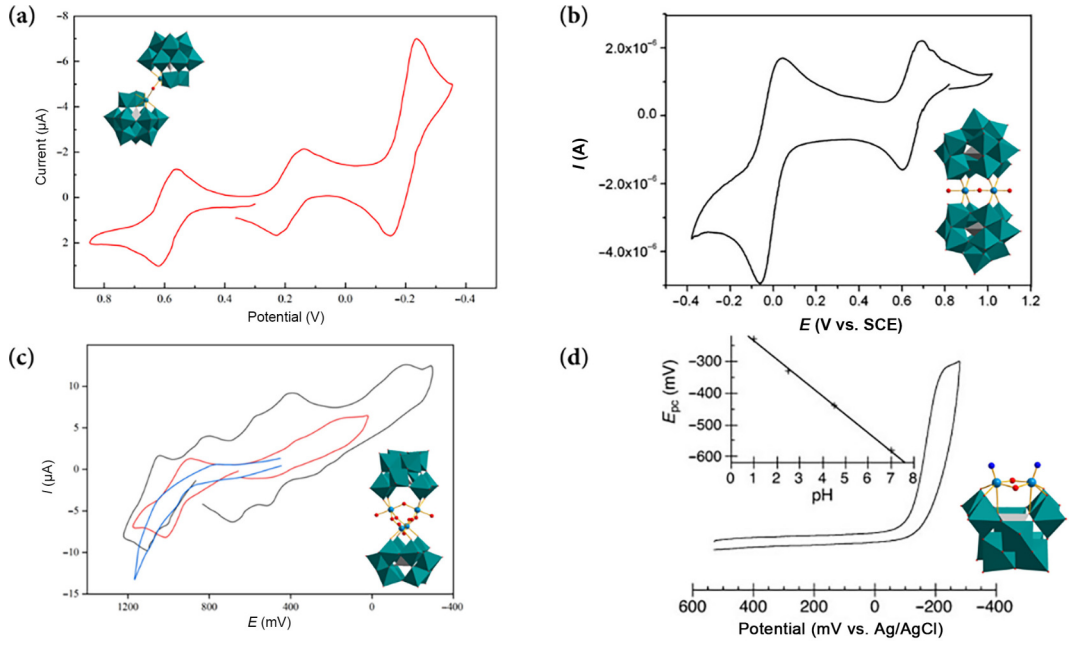

Figure 16 (a) CV of $[\{SiW_{11}O_{39}Ru^{IV/III}\}_2O]^{11-}$ in 0.5 M $KHSO_4$ (pH = 1.5) solution. (b) CV of **Ru2-PW11** (pH = 3). (c) CVs of 1 mM **Ru4-SiW10** in 0.1 M HCl (pH = 1.0, black curve), in 0.4 M sodium acetate buffer (pH = 4.7, red curve), and of 0.6 mM **Ru4-SiW10** (pH = 7.0, blue curve). Scans start at the rest potentials (800, 600, and 400 mV, respectively), and potentials are relative to a Ag/AgCl (3 M NaCl) reference electrode. (d) CV of $K_2(Me_2NH_2)_2H_2[\gamma\text{-}SiW_{10}O_{38}\{Ru^{VI}N\}_2]$ (0.5 mM) in 0.1 M HCl (scan rate 100 $mV{\cdot}s^{-1}$). Inset: Cathodic peak potential vs. pH. (a) is reprinted from the permission from Ref. [37], © The Royal Society of Chemistry 2003. (b) is reprinted from the permission from Ref. [77], © WILEY-VCH Verlag GmbH & Co. KGaA, Weinheim 2008. (c) is reprinted from the permission from Ref. [16], © WILEY-VCH Verlag GmbH & Co. KGaA, Weinheim 2008. (d) is reprinted from the permission from Ref. [62], © WILEY-VCH Verlag GmbH & Co. KGaA, Weinheim 2009.

the combination of the stable POM structure and the effective oxidation state of Ru center. Each step of the catalytic oxidation processes contains an overall two-electron transfer reaction, which could be attributed to the process where the substrate is catalyzed by **Ru4-SiW10** with higher valent as shown in Scheme 1, or ethanol could spontaneously reduce **Ru4-SiW10** as shown in Scheme 2 ($\{Ru^{IV}_4\}$ = $\{Ru^{IV}_4O_4(OH)_2(H_2O)_4\}$). With studies conducted in alcoholic electrolyte which contains 0.50 M H_2SO_4, using a **Ru4-SiW10**/PDDA-modified (PDDA = poly(diallyldimethylammonium chloride)) glassy carbon electrode as the sample, in acidified methanol and ethanol media, two surface-confined processes with $E^{0'}$ values of 0.278 and 0.096 V, respectively, were observed (Fig. 17(a)). These processes exhibit similar characteristics to those seen in CVs of surface-confined **Ru4-SiW10** in aqueous solution containing 1.0 M methanol or ethanol (Fig. 17(b)). Under the given condition, the catalysis onset potentials are 0.6 V (vs. Fc/Fc^+) (Fc/Fc^+ = ferrocene/ferricenium) for the two media. However, despite comparable surface concentrations of **Ru4-SiW10**, the catalytic current for methanol is approximately 2.2 times greater than for ethanol at 0.80 V. This disparity is likely attributable to the involvement of $\{Ru^V_4\}$ in the catalytic process, facilitated by the lacunary POM structure and the favorable environment for methanol oxidation (Fig. 17(a)).

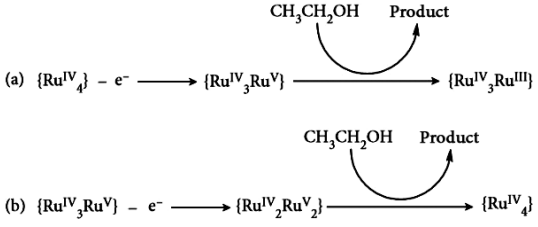

Scheme 1 Reaction pathways proposed for $[\{Ru_4O_4(OH)_2(H_2O)_4\}(\gamma\text{-}SiW_{10}O_{36})_2]^{10-}$-catalyzed electrooxidation of ethanol in an acidic medium.

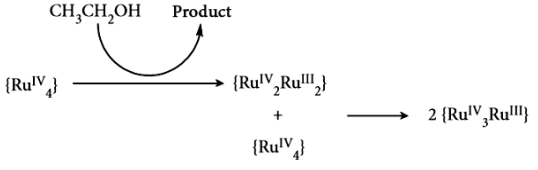

Scheme 2 Proposed mechanism for the spontaneous reduction of $[\{Ru_4O_4(OH)_2(H_2O)_4\}(\gamma\text{-}SiW_{10}O_{36})_2]^{10-}$ by ethanol.

By contrast, aqueous solutions of 2.0 M H_2SO_4 containing either 1.0 M methanol or 1.0 M ethanol exhibit similar oxidation current magnitudes, with $\{Ru^VRu^{IV}_3\}$ serving as the catalytically active species in both cases (Fig. 17(b)). When bulk electrolysis (with 100 C of charge passing at a carbon cloth working electrode) is conducted in the supporting alcoholic electrolyte which involves 0.50 M H_2SO_4, the resulting products comprised 38.5% aldehydes and 61.5% acids for ethanol, and 22.4% aldehydes and 77.6% acids for methanol, under surface-confined catalytic conditions at potentials of 0.80 or 0.93 V (vs. Fc/Fc^+). When conducting the bulk electrolysis in the supporting electrolyte which contains 0.10 mM **Ru4-SiW10** dissolved in the methanol or ethanol media both involving 0.50 M H_2SO_4, the product ratio of aldehyde increased to 73.8% at an applied potential ($E_{app.}$) of 0.66 V (vs. Fc/Fc^+) for ethanol and 47.6% at 0.83V (vs. Fc/Fc^+) for methanol oxidation, respectively. Notably, maintaining the catalyst dosage (0.10 mM **Ru4-SiW10**) while adjusting the supporting electrolytes to a more acidic (2.0 M H_2SO_4) or more moderate environment (1.0 M KNO_3 and 0.40 M sodium phosphate buffer solution (pH = 7.0)) led to a substantial increase in the quantities of products formed during ethanol and methanol oxidation. Under surface-confined conditions in alcoholic media, the faradaic efficiency for ethanol oxidation reaches 99%, while for methanol oxidation, it achieves

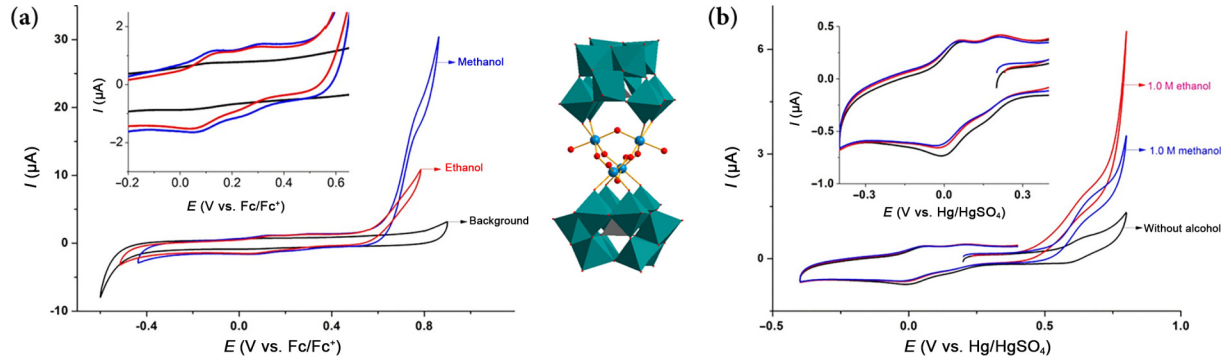

Figure 17 (a) CVs obtained at a 3.0 mm diameter glassy carbon electrode modified with 3 μL of **Ru4-SiW10**/PDDA (Γ = 0.03 nmol·cm^{-2}) with a scan rate of 0.05 V·s^{-1} in ethanol (red line) and methanol (blue line) solutions containing 0.50 M H_2SO_4 as the electrolyte. CV obtained with a PDDA-modified glassy carbon electrode in ethanol solution is also shown for comparison (black line). (b) CVs obtained at a 3.0 mm diameter glassy carbon electrode modified with 3 μL of **Ru4-SiW10**/PDDA (Γ = 0.08 nmol·cm^{-2}) with a scan rate of 0.01 V·s^{-1} in aqueous 2.0 M H_2SO_4 solution without alcohol (black line) and with 1.0 M ethanol (red line) or methanol (blue line). (a) and (b) are reprinted from the permission from Ref. [98], © American Chemical Society 2016.

98%. In contrast, under other conditions, the faradaic efficiencies experience a slight reduction but consistently remain above 94%. Long-term electrolysis data reveals no considerable decline in catalytic current after passing 100 C of charge (>1000 electrons per catalyst) [98].

In addition, **Ru-PW11** is also capable of catalyzing DMSO oxidation using a graphite thread as anode and can maintain at a potential of +1.10 V for a duration of 28 h, in 1.0 M H_2SO_4-Na_2SO_4 solution (pH = 0) with the current efficiency of the oxidation being 92% for which most Ru complex can't achieve in the low pH. When producing 100 μmol sulfone, the catalyst achieves a ratio of approximately 40% for the oxidation from sulfoxide to sulfone. During this process, the valence of Ru in the catalyst alternates between +III and +V, resulting in a turnover number (TON) of 40. While **Ru-PW11** also exhibits catalytic activity in the reduction of DMSO owing to its low valence state, proceeding via a two-electron process, the amount of DMSO reduced is approximately 30 mol per 1 mol of POM, with a current efficiency of approximately 50%. Notably, **Ru-PW11** remains present in the final solution, suggesting possible mechanisms involving the transfer of electrons from the reduced POM to bound DMSO or the nascent hydrogen reduction of free or bound DMSO [13]. [{Ru(C_6H_6)(H_2O)}{Ru(C_6H_6)}(γ-$SiW_{10}O_{36}$)]$^{4-}$ in 1 M HCl also exhibits high activity in catalyzing DMSO oxidation. The mechanism for this process is as follows. First, the Ru-centered oxidation undergoes a cathodic shift in potential and becomes a composite process. Second, the solvent limit also shifts in a negative potential direction, and the intensity of the catalytic current is influenced by the excess amount of DMSO added. Along with efficient catalytic oxidation of DMSO, ligand substitution on the Ru centers also occurs. The second-order rate constant for this process is approximately 2.30 × 10^3 M^{-1}·s^{-1}. A comparison of catalytic activity tests using [Ru(C_6H_6)Cl_2]$_2$ confirms the superior performance of the POM [65]. It is also hypothesized that the vacancy in the POM may play a considerable role in the synthesis, resulting in a structure with more exposed active sites than **Ru2-SiW10**. This hypothesis warrants further investigation.

Recognizing the increasing importance of accurate nitrite detection and removal, Bi et al. elucidated the electrocatalytic activity of Na_7[($Ru^{II}C_6H_6$)PW_9O_{34}]·14H_2O in reducing nitrate in a medium of 1.0 M LiCl + HCl (pH = 3.0) containing 1.0 M nitrate [81]. Additionally, they synthesized Na_4K_2[HVW_7O_{28}Ru(DMSO)$_3$]·Na_3VO_4·15H_2O, which exhibits electrocatalytic activity toward the reduction of NO^{2-} and H_2O_2 at pH 3.0 [85]. However, their research primarily focused on introducing novel structures and did not produce a detailed analysis of the catalytic properties.

In 2019, Niu et al. synthesized $Rb_{10}K_3H_6$[SeO_3($H_9Ru^{IV}_{5.5}W_{30.5}O_{114}$)]$Cl_3$·48$H_2O$, which also exhibits catalytic activity in the reduction of nitrite. The characteristic redox processes of this POM with a Ru^{IV} center involve two quasi-reversible reactions: $Ru^{V/IV}$ with $E_{1/2}$ = +0.93 V vs. Ag/AgCl and $Ru^{IV/III}$ with $E_{1/2}$ = +0.13 V vs. Ag/AgCl. Additionally, a quasi-reversible reaction occurs for the transition from Ru^{III} to Ru^{II}, with $E_{1/2}$ = −0.08 V vs. Ag/AgCl. The inherent rapid electron transfer capability and redox-active sites of Ru-POM contribute to its stability in the efficient electrocatalysis of NO^{2-} oxidation. As the concentration of $NaNO_2$ increased, a consistent enhancement in the oxidation current response was observed. A precise relationship was established between the nitrite concentration and the oxidation current response over a concentration range of 5 × 10^{-4} to 1 × 10^{-2} mol·L^{-1}. The linear regression equation was calculated as I_p (A) = 3.36 × 10^{-5} + 0.016[nitrite] (mol·L^{-1}), with a determination coefficient of 0.996. The electrocatalytic oxidation of nitrite was characterized as an electrochemically irreversible diffusion-controlled process. The peak potential (E_{pa}) also exhibited a linear relationship with the logarithm of the scan rate (log v) as expressed by the equation: E_{pa} = 0.89 + 0.057log v (R^2 = 0.997) [94].

Well base could efficiently improve the electrocatalyst activity. Nickel foam has been confirmed as a great base to improve the electrocatalyst activities by Hou's group in 2018. They utilized a silane coupling agent to fix POM catalyst on the nickel foam electrode. The POM retains its molecular structure upon being loaded onto nickel foam. Profited from the nickel foam's high specific surface area and superior electronic conductivity, this composite material demonstrates outstanding electrocatalytic performance for the OER and remarkable stability under mild pH conditions. When the concentration of POM is 1 mM and pH value is 6, it shows the excellent electrocatalytic activity [99].

In 2020, Ryu, Yang and Park et al. used perylene diimide amino N-oxide (PDI–NO) functionalized graphene as a substrate to enhance the electrocatalytic activity of a POM for water oxidation. Leveraging the hydration repulsion effects induced by PDI–NO, they achieved effective functionalization of graphene and ensured its pH-independent dispersion. Their research demonstrated that PDI–NO functionalized graphene could serve as an efficient electron mediator for the OER, enhancing the electrocatalytic activity of a Ru–POM catalyst in an acidic environment. The

complex was synthesized by homogeneously dispersing PDI–NO@G and Ru–POMs with varying mass ratios in 0.5 M H_2SO_4 via sonication for 24 h. Remarkably, **Ru4-SiW10** exhibits exceptional OER activity with an onset potential of approximately 1.4 V vs. RHE. However, when PDI–NO, graphene, and PDI–NO@G are used individually, they fail to demonstrate substantial catalytic activity. Intriguingly, the OER activity of **Ru4-SiW10** is considerably enhanced when it is stabilized by PDI–NO@G, while minimal electrocatalytic activity is observed in the presence of only PDI–NO. These observations underscore the crucial role of PDI–NO@G as an electron mediator. Furthermore, they suggest that PDI–NO acts as a redox-active material, while graphene serves as an excellent conductor in the PDI–NO@G composite. The overpotentials of **Ru4-SiW10** alone and PDI–NO@G/Ru4-SiW10 at a current density of 20 mA·cm^{-2} are 1.53 and 1.43 V vs. RHE, respectively. These values represent some of the lowest overpotentials reported to date, particularly under acidic conditions. The Tafel slopes for PDI–NO@G, **Ru4-SiW10**, and PDI–NO@G/**Ru4-SiW10** are 458.1, 94.1, and 61.3 mV·dec^{-1}, respectively (Fig. 18(a)). The outstanding electrocatalytic activity observed can be attributed to the PDI–NO@G composite, which contains positively charged tertiary amine (N^+) groups that interact strongly with Ru-POM. This interaction promotes efficient electron transfer between the two components (Fig. 18(b)). The PDI backbone, with its electron-deficient carbon atoms and large π–π interaction area, enhances the dispersibility of graphene in aqueous media, enabling strong interaction with graphene. Furthermore, the zwitterionic –NO side terminal groups effectively prevent graphene aggregation across various pH levels through hydration repulsion effects [100].

In 2022, Dong and Lv et al. reported the synthesis of a Ru_4/PEI-rGO composite via electrostatic interaction between **Ru4-SiW10** and polyethyleneimine (PEI), which was then modified with reduced graphene oxide (rGO). The **Ru4-SiW10**/PEI-rGO composite exhibited high electrocatalytic performance in catalyzing 5-hydroxymethylfurfural (HMF). After electrocatalysis for 6 h at a potential of 0.94 V vs. Ag/AgCl, analysis of the anode oxidation products using high-performance liquid chromatography (HPLC) revealed a conversion rate of 50.8% for the HMF substrate, with a total selectivity of 95.5% toward anodic furanic products. Notably, 2,5-diformylfuran was the dominant product, with a selectivity of 66.2%. The underlying mechanism involves a process during electrolysis where, in the anodic chamber, the Ru^{IV} centers present in the **Ru4-SiW10**/PEI-rGO composite undergo an initial oxidation to a three-electron state. This state possesses the ability to catalyze the conversion of HMF into furanic products while simultaneously reducing the Ru^{IV} centers to Ru^{III} species. Meanwhile, the protons released during these processes are further reduced to hydrogen in the cathodic chamber, completing a full valorization cycle of HMF to furanic products and hydrogen [101]. Notably, a substrate that can strongly interact with POMs and enhance electrical conductivity appears to considerably improve the catalytic activity.

In 2024, Lu et al. reported a groundbreaking work where they used an "atom-to-cluster" strategy to synthesize a highly dispersed $RuSe_2$-WO_x@HMCS electrocatalyst with exceptional properties for hydrogen evolution reaction (HER) in both acidic and alkaline solutions (HMCS, hollow mesoporous carbon spheres). This remarkable composite was synthesized through a multistep process. Initially, PW9 and $RuCl_3$ were reacted to obtain Ru_xPW9. Subsequently, Ru_xPW9 was combined with HMCS for loading. Finally, the electrocatalyst was obtained after *in situ* selenization, which effectively exposed the active sites owing to the dual confinement of trilacunary PW9 and HMCS. The strong interaction between $RuSe_2$-WO_x and HMCS facilitated electron transfer and enhanced the electrocatalytic activity. HMCS provides numerous structural defects to the overall structure, promoting electron transfer. Additionally, the selection of HMCS as the support ensures high dispersion of $RuSe_2$-WO_x and improves electrical conductivity. Compared to **Ru3-SiW9**, selenization optimizes the electronic structure of Ru, leading to increased electrical conductivity, improves utilization of Ru, and enhances synergistic effects between Ru and W. As a result, the composite exhibits exceptional electrocatalytic performance for HER, with overpotentials (η) of only 58 and 60 mV in acidic and alkaline solutions, respectively, at a current density of 10 mA·cm^{-2}. These overpotentials are considerably lower than those of $RuSe_2$@HMCS (108 and 135 mV), $Ni_{0.85}Se$-WO_x@HMCS (152 and 156 mV), WO_x@HMCS (179 and 186 mV), and HMCS (249 and 265 mV) in 0.5 M H_2SO_4 and 1 M KOH solutions, respectively. Moreover, the

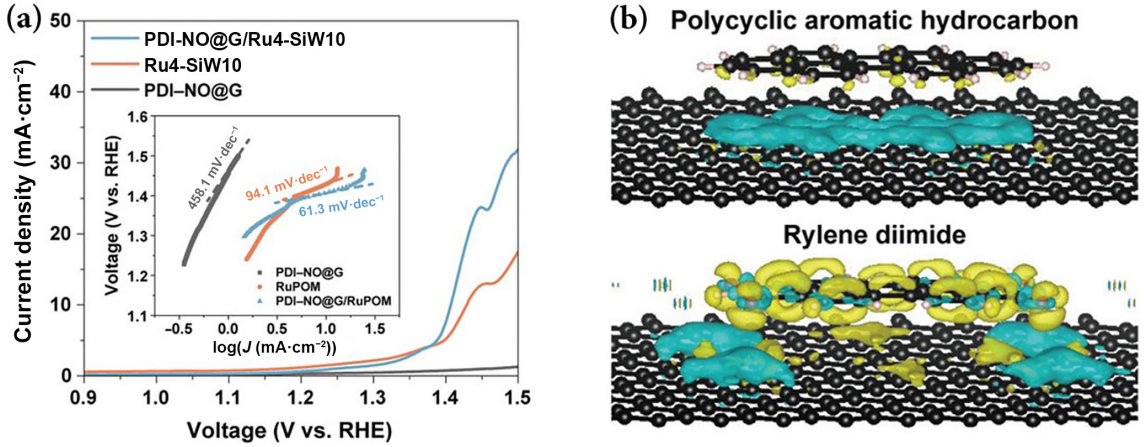

Figure 18 (a) Polarization curves of a CFP electrode with PDI–NO@G, **Ru4-SiW10**, and a mixture of PDI–NO@G and **Ru4-SiW10** in 0.5 M H_2SO_4. The inset shows the Tafel plots of the respective samples. (b) Electron density difference between the interacting system and the sum of noninteracting individual systems (upper: polycyclic aromatic hydrocarbon and graphene, lower: rylene diimide and graphene), where light blue and yellow color denote the depleted and increased density upon interaction, respectively, with the same isosurface magnitude used for two cases. The black, blue, white, and red atoms represent carbon, nitrogen, hydrogen, and oxygen, respectively. (a) and (b) are reprinted from the permission from Ref. [100], © Springer Nature 2018.

HER activity of $RuSe_2$-WO_x@HMCS surpasses that of the commercial Pt/C electrocatalyst at overpotentials of ≥ 152 and ≥ 258 mV in both acidic and alkaline solutions [102]. Thus, confining Ru and another transition metal in a POM, which has been demonstrated to have a synergistic effect for specific applications, is a promising strategy for future research.

3.2 Photocatalysis

Ru-POMs are widely used as catalysts for the conversion of amines to imines through oxidation processes. Niu and Wang et al. synthesized three POMs containing cyclic Ru groups $(K_6H[\{Ru_2Cl(H_2O)(CH_3COO)_2\}\ \{WO\text{-}(H_2O)\}_2(PW_9O_{34})_2]\cdot 14H_2O$ (denoted as **Ru-POM-PC-1**), $K_5Na_9H_8[Ru_2(WO_2)_4(AsW_9O_{33})_4]\cdot 50H_2O$ (denoted as **Ru-POM-PC-2**), $Na_{13}H_5[Ru_4(H_2O)_2(Cl)_2(WO_2)_4(AsW_9O_{33})_4]\cdot 43H_2O$ (denoted as **Ru-POM-PC-3**)) that exhibit high catalytic activity in converting amines to imines in the presence of oxygen (particularly in aniline coupling reactions) [17, 92]. As evident from Table 5, POMs with a higher number of Ru active sites demonstrate enhanced photocatalytic activity. Entries 3 and 4 in Table 5 reveal that **Ru-POM-PC-1** exhibits limited catalytic activity for aniline substrates bearing Cl or Br substituents on the meta-position. However, it displays high activity for substrates with substituents on the para-position (87.2% for Br and 92.6% for Cl) (not mentioned in the table). Furthermore, entries 8 and 9 in Table 5 suggest that the photocatalytic activity of different amines is influenced by the structure of the POMs. Notably, benzylamine derivatives containing electron-donating groups (Me and OMe) yield higher reaction rates compared to those with electron-

Table 5 Oxidative coupling of various amines to imines over **Ru-POM-PC-1**, **Ru-POM-PC-2**, and **Ru-POM-PC-3**[a]

Entry	Substrate	Product	Yield (%)		
			Ru-POM-PC-1	**Ru-POM-PC-2**	**Ru-POM-PC-3**
1	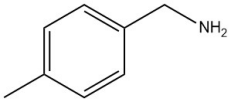	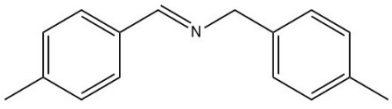	97.2	72.3	94.4
2	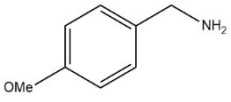	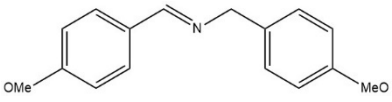	99.2	77.0	94.6
3	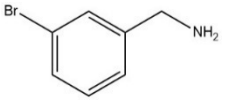	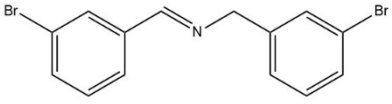	—	69.2	91.6
4	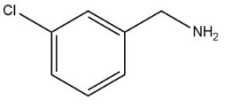	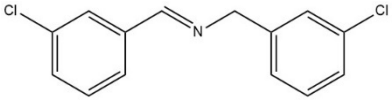	—	58.5	92.5
5	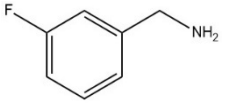	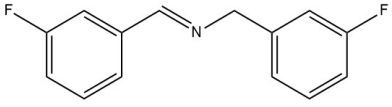	96.2	66.7	93.8
6	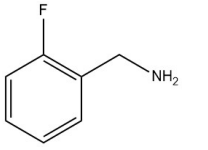	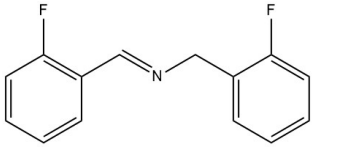	94.6	54.5	90.3
7	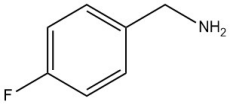	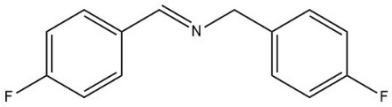	92.6	52.4	92.2
8	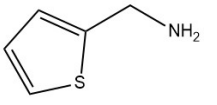	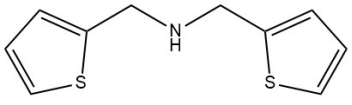	94.8	49.0	81.0
9	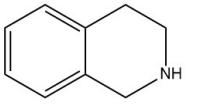	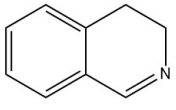	15.2	48.3	62.1
10	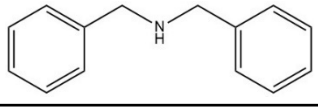	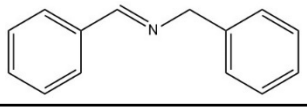	6.5	4.8	7.5

[a]Reaction conditions: benzylamine (1 mmol), catalyst (0.1 mol%), solvent-free, room temperature, 10 W white LED lamp, O_2 (1.5 atm for **Ru-POM-PC-1**, 1.0 atm for **Ru-POM-PC-2** and **Ru-POM-PC-3**), T = 24 h, isolated yields.

withdrawing groups (Cl, Br, and F). This variation in yield is attributed to the electronic properties of the substituents, as benzylamine derivatives with electron-donating groups exhibit enhanced reactivity. However, secondary and tertiary amines exhibit low reactivity under the same reaction conditions. Additionally, using $RuCl_3$ alone, As_2W_{19} alone, or simple mixtures of $RuCl_3$ and As_2W_{19} as catalysts for the oxidative coupling of benzylamine yielded only small amounts of target products (55.8%, 31.8%, and 62.1%, respectively), considerably lower than the yields obtained using Ru-POMs as the catalysts (Table 5, entry 1) [17, 92]. The plausible mechanism involves the formation of a reactive intermediate, Ru^{IV}–POM(W^{V}), under the reaction conditions. This intermediate is responsible for the oxidation of amines to amine radical cations, facilitating the subsequent coupling reactions. Concurrently, the intermediate undergoes reduction to Ru^{III}–POM(W^{V}), which then returns to its original state as Ru^{III}–POM(W^{VI}) by transferring an electron to oxygen, leading to the formation of the superoxide radical anion ($\cdot O_2^-$). Finally, the amine radical cation reacts with the superoxide radical anion to generate the imine intermediate [92]. It is evident that the efficient electron transfer between the Ru center and the POM, as well as the oxidation state of the Ru^{IV} center, play crucial roles in the catalytic process. Additionally, the exposed active site provided by the ring-like Ru group contributes to the high activity of the catalysts. Notably, the catalysts exhibit good stability and can be reused five times without considerable loss of activity. In 2022, Niu et al. discovered two POMs capable of efficiently catalyzing the oxidative coupling reaction of a wide range of primary benzylamine derivatives, including those with various functional groups (H, F, Cl, Br, and Me), under optimized conditions. These POMs achieved yields ranging from 71% to 96%, considerably higher than the 70% yield obtained using $RuCl_3$ and Na_2WO_4 as catalysts. Notably, these POMs exhibited activity even for benzylamines with functional groups in the inner ortho position, where steric hindrance typically hinders imine formation, resulting in high yields. The proposed mechanism for this process is as follows. Initially, the catalyst donates an electron to an oxygen molecule, reducing it to the superoxide radical ($\cdot O_2^-$). Simultaneously, the benzylamine undergoes one-electron oxidation by the catalyst, forming a benzylamine radical cation (Ph–CH_2–NH_2^+). The superoxide radical then abstracts a proton and a hydrogen atom from the radical cation, generating a highly reactive imine intermediate (RCH=NH). This imine intermediate subsequently undergoes a nucleophilic addition reaction with a second primary amine, forming an aminal. Finally, the aminal releases NH_3, yielding the desired product. This catalytic process is facilitated by the catalysts, which can be reused five times without considerable loss of reactivity [80]. However, further research is needed to elucidate the specific role of the novel Ru-POM structures in this catalytic mechanism.

Ru-POMs have also made considerable contributions to the field of catalytic water oxidation and can be used as catalysts for various water oxidation pathways, which will be discussed in detail in this section. First, Ru-POMs exhibit high catalytic activity in water oxidation reactions involving cerium ammonium nitrate (CAN). This reaction primarily involves the nucleophilic attack of water on the high-valent Ru centers [33]. All {$Ru^{III}XW_{11}(H_2O)$} (X = Si, P, Ge) complexes tested in 20 mL of 0.1 M HNO_3 containing 0.3 mM of catalyst and 30 mM of CAN at room temperature exhibit good oxygen evolution capability. The POMs with $Ru^{III}(H_2O)$ can be stabilized and produce oxygen with a yield of approximately 130 μmol in 2 h, with **Ru-PW11** showing the highest yield of nearly 160 μmol. In contrast, the POM with $Ru^{II}(H_2O)$ exhibits minimal catalytic activity but still outperforms a mixture of $[Ru(benzene)Cl_2]_2$ and $K_7PW_{11}O_{39}$ [47]. However, replacing H_2O with DMSO results in good catalytic performance for Ru^{II} under the same conditions, with an initial oxygen evolution rate of approximately half of that catalyzed by **Ru4-SiW10**, which contains four Ru^{IV} active sites, as discussed later. Despite reaching saturation yield in 40 min, its low saturation yield of approximately 80 μmol limits its widespread application [45]. Identifying strategies to enhance its stability could be a promising research direction. Dawson-type Ru^{III}-POMs exhibit even lower catalytic activity than Keggin-type POMs [56].

In the case of **Ru4-SiW10**, the presence of excess CAN results in excellent catalytic activity within 2 h, with a yield reaching nearly 400 μmol, more than double that of the POMs discussed above. This high activity is attributed to a pseudo-first-order kinetic constant of 9.92×10^{-3} s^{-1} (Fig. 19(a)) [32]. The {$Ru_4O_4(OH)_2(H_2O)_4$} cluster at the core of **Ru4-SiW10** can be regarded as an optimal RuO_2 cluster where each Ru^{IV} site is accessible to the solvent, presenting the largest surface area favorable for catalysis. While the metal spectators do not directly participate in the chemical reaction, they play a critical role in providing electronic stabilization for the formation of a high-valent Ru–O site capable of water oxidation [103].

Another widely used method for water oxidation catalysis involves the use of $[Ru(bpy)_3]^{3+}$ as an oxidizing agent. All catalysts identified using this oxidation method are high-valent Ru-POMs. **Ru4-SiW10** also exhibits high oxidation activity under this method (Fig. 19(b)). It is evident that the {Ru_4} core with {SiW_{10}} possesses superior catalytic properties compared to that with {PW_{10}} [79]. In experiments dominated by **Ru4-SiW10**, water oxidation activity was observed to be two orders of magnitude higher than that of $RuCl_3$. Additionally, the turnover number for **Ru4-SiW10** in catalytic water oxidation experiments is approximately 18 ($n(O_2)/n$(**Ru4-SiW10**)) or 120 ($n([Ru(bpy)_3]^{3+})/n$(**Ru4-SiW10**)) [16]. The simplified mechanism for the water oxidation by $[Ru(bpy)_3]^{3+}$ has been determined for **Ru4-SiW10** to be as follows:

$$[Ru(bpy)_3]^{3+} + \{Ru_4^{IV}\} \rightarrow [Ru(bpy)_3]^{2+} + \{Ru_3^{IV}Ru^{V}\} \quad (1)$$

$$[Ru(bpy)_3]^{3+} + \{Ru_3^{IV}Ru^{V}\} \rightarrow [Ru(bpy)_3]^{2+} + \{Ru_3^{IV}Ru_2^{V}\} \quad (2)$$

$$[Ru(bpy)_3]^{3+} + \{Ru_3^{IV}Ru_2^{V}\} \rightarrow [Ru(bpy)_3]^{2+} + \{Ru^{IV}Ru_3^{V}\} \quad (3)$$

$$[Ru(bpy)_3]^{3+} + \{Ru^{IV}Ru_3^{V}\} \rightarrow [Ru(bpy)_3]^{2+} + \{Ru_4^{V}\} \quad (4)$$

$$\{Ru_4^{V}\} + 2H_2O \rightarrow \{Ru_4^{IV}\} + O_2 + 4H^+ \quad (5)$$

Equation (5) is the rate-determining step, while Eq. (4) is a preequilibrium reaction. Reactions in Eqs. (1)–(4) occur rapidly. Ultimately, $[Ru(bpy)_3]^{2+}$ is regenerated to the +3 valence state by $S_2O_8^{2-}$ under irradiation [79].

The water oxidation catalyzed by $K_2(Me_2NH_2)_2H_2[\gamma$-$SiW_{10}O_{38}\{RuN\}_2]\cdot 5H_2O$ (denoted as **Ru2-SiW10**) yields approximately 40% dioxygen, calculated as productivity = $4n(O_2)/n([Ru(bpy)_3]^{3+}$, and exhibits a catalyst turnover number of approximately 12, calculated as TON = $n(O_2)/n$(**Ru2-SiW10**).

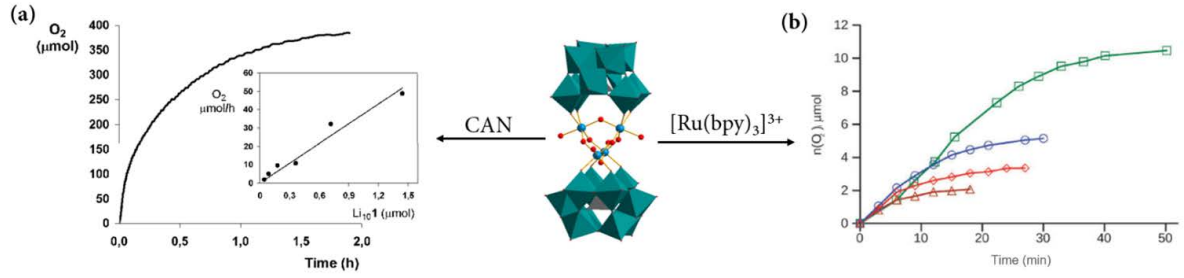

Figure 19 Kinetics of O_2 evolution by **Ru4-SiW10** (4.3 μmol) with CAN (1720 μmol), in H_2O (10 mL) at 20 °C. The inset shows a plot of initial rates vs. **Ru4-SiW10** (0.045–1.45 μmol) with CAN (10.9 mmol). (b) Kinetics of light induced O_2 formation from water oxidation with persulfate as a sacrificial electron acceptor. Conditions: Xe lamp, 420–520 nm bandpass filter, 1.0 mM $[Ru(bpy)_3]Cl_2$, 5 mM $Na_2S_2O_8$, 20 mM Na_2SiF_6 buffer pH 5.8, 5.0 mM **Ru4-SiW10** (green squares), 5.1 mM $[\{Ru_4O_5(OH)(H_2O)_4\}(\gamma\text{-}PW_{10}O_{36})_2]^{9-}$ (blue circles), 3.9 mM **Ru4-SiW10** (red diamonds) or 2.6 mM $[\{Ru_4O_5(OH)(H_2O)_4\}(\gamma\text{-}PW_{10}O_{36})_2]^{9-}$ (brown triangles), total solution volume in each reaction, 8 mL. (a) is reprinted from the permission from Ref. [32], © American Chemical Society 2008. (b) is reprinted from the permission from Ref. [79], © The Royal Society of Chemistry 2010.

Under highly oxidative reaction conditions, the catalyst may undergo decomposition owing to the oxidation of its nitride ligands, similar to the irreversible oxidation observed in its CV experiments performed in acetonitrile. Deprived of its nitrogen atoms, the catalyst could transform into one of the known catalysts for water oxidation, namely $\gamma\text{-}[SiW_{10}O_{38}\{Ru^{III}(OH_2)\}_2]^{6-}$ and **Ru4-SiW10** [62]. $[Ru(bpy)_3]^{3+}$ is used as the photosensitizer, and $S_2O_8^{2-}$ serves as a sacrificial electron acceptor. **Ru3-SiW9** exhibits even higher catalytic activity than **Ru4-SiW10** despite using a dosage nine times greater than **Ru4-SiW10**. This remarkable activity is attributed to the $\{Ru^{III}Ru^{IV}_2\}$ group, as evidenced by its CV profile, which displays three redox peaks: $Ru^{III/II}$ (−0.22 to −0.12 V vs. Ag/AgCl, pH 1.0), $Ru^{IV/III}$ (0.32–0.59 V vs. Ag/AgCl, pH 1.0), and $Ru^{V/IV}$ (0.70–0.87 V vs. Ag/AgCl, pH 1.0) [64]. Although the yields obtained using this method are lower than those achieved with CAN, it addresses two key issues: (i) increasing access to a larger fraction of visible-light energy through photosensitizers with absorption properties at $\lambda > 520$ nm, and (ii) reducing charge recombination and/or decomposition of the oxidized photosensitizer by facilitating rapid hole scavenging by the catalytic domain [104]. It appears that the catalytic activity for water oxidation is closely related to the coordination environment and the redox state of the Ru centers. Among all the Ru active sites, the $\{Ru_4O_4(OH)_2(H_2O)_4\}$ cluster exhibits the highest catalytic efficiency. Whether this cluster can also perform effectively in open POMs, such as $[\{Ru^{IV}_4O_6(H_2O)_9\}_2Sb_2W_{20}O_{68}(OH)_2]^{4-}$, is a subject of further investigation.

Furthermore, the mode of interaction with other molecules is also widely used. A cationic water-soluble saddle-distorted porphyrin, existing in its di-protonated form (H_41^{6+}), a type of photosensitizer, forms stable supramolecular assemblies with **Ru-SiW11** through electrostatic interactions. This material was synthesized in 2018 by Kojima et al. owing to the strong interaction between H_41^{6+} and POM, leading to the formation of a 2:1 complex. Under visible-light irradiation, these assemblies form adducts between the porphyrin and an oxidant, enabling them to perform photocatalytic oxidation of organic substrates in water. Around both the upper and the underside of the center of H_41^{6+}, two Cl^- ions are present, capping it and forming strong hydrogen bonds via four inner pyrrolic NH protons. The stabilization of the saddle-distorted H_41^{6+} is attributed to this favorable combination mode, which also enables its photoexcitation capability. In the composite, the POMs function as efficient electron donors owing to the photoinduced electron transfer (PET) from the POMs to H_41^{6+} in the 1:2 supramolecular assemblies. The electrostatic interaction between the supramolecular catalyst composite and $S_2O_8^{2-}$ renders it a highly effective catalyst for water oxidation. Coupled with the rapid intra-supramolecular electron transfer from H_41^{5+}, which is formed via PET from **Ru-SiW11** to $^1(H_41^{6+})^*$, to $S_2O_8^{2-}$, the photocatalytic reactions proceed efficiently. The material has been demonstrated to effectively perform photocatalytic oxidation of organic substrates (alcohol → aldehyde/ketone) in water under visible-light irradiation [105].

In 2019, Bonchio and Prato et al. employed template-directed assembly of light-harvesting perylene bisimide domains with a POM, which serves as a water oxidation catalyst, to synthesize a catalyst that mimics the proximal Mn_4CaO_5 oxygen-evolving catalyst in photosystems II (PSII–OEC) in nature and is specifically tailored for oxygen evolution. The catalyst was obtained due to self-assembly of bis-cationic N,N'-bis(2-(trimethylammonium) ethylene)perylene-3,4,9,10-tetracarboxylic acid bisimide (PBI) with **Ru4-SiW10** in water solvent. The near equivalence in axial lengths of both **Ru4-SiW10** and PBI molecular structures, along with the complementary charge distributions surrounding the longest dimension, contribute to the electrostatic assembly of PBI and **Ru4-SiW10**, particularly in an axial alignment. Additionally, the hydrophobic properties of the molecular building blocks play a considerable role in the assembly process (Fig. 20(a)). Upon testing, a redox potential of $E = +2.20$ V vs. NHE was attributed to the PBI^*/PBI^- couple. It is expected that the excited-state PBI^* will harness multiple electron transfer from **Ru4-SiW10**, exhibiting oxidation characteristics in the potential range of 0.75–1.02 V, under the potential at which water oxidation begins at 1.2 V vs. NHE. Consequently, the driving force for electron transfer is considerably higher in the PBI quantasome compared to classical Ru polypyridine sensitizers ($[Ru(bpy)_3]^{3+/2+} = +1.26$ vs. NHE) or CAN (+1.75 vs. NHE), resulting in high photocatalytic activity (Fig. 20(b)) [106].

The materials used to load Ru-POMs can enhance their properties. Atomic layer deposition (ALD) can apply a nanoscale oxide coating (Al_2O_3), confirmed to have the potential for facilitating immobilization and considerably enhancing the stability of this extensive family of molecular water oxidation catalysts when positioned on electrode surfaces (Hill et al., 2017). Their studies revealed that the catalytic activity of the system correlated with the thickness of the Al_2O_3 layer used as the base. POMs fixed on the 4

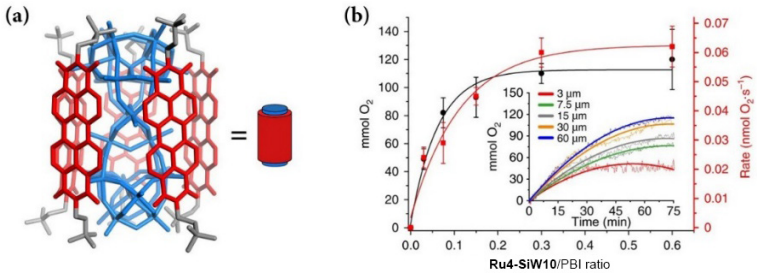

Figure 20 (a) Figurative representation of the $[PBI]_5$ **Ru4-SiW10** building block (**Ru4-SiW10** blue framework; PBI, red (aromatic body) and grey (alkylammonium tails) framework), shown as a core-shell cylindrical amphiphile (cartoon: PBI shell, red cylinder; **Ru4-SiW10**, blue cylinder). (b) Plot of evolved O_2 (left axis, black) and initial rate of O_2 production (right axis, red) vs. **Ru4-SiW10**/PBI ratio. Error bars arise from the maximum deviations in experiments run in triplicate. Inset: oxygen evolution kinetics with [PBI] = 100 μM, $[S_2O_8^{2-}]$ = 1 mM, Ru_4POM (3.0–60 μM) in 20 mM phosphate buffer, pH 7, on irradiation with an LED white lamp (4.5 mW·cm^{-2}). (a) and (b) are reprinted from the permission from Ref. [106], © Springer Nature 2018.

nm coated Al_2O_3 photoanode remained for 12 h, while those on the 3 nm coating dissolved into the electrolyte. The 6 nm blocks hinder hole transfer to the electrolyte. This result provides further convincing evidence that the thickness of Al_2O_3 ALD layers is crucial because a critical thickness (~ 4 nm) ensures POMs remain attached to the photoanode surface during catalysis. Conversely, under applied potential conditions (240 mM sodium borate buffer with 0.1 M KNO_3, pH 8.3, potential maintained at 1.24 V vs. RHE), hematite–APS–**Ru4-SiW10**–4nm Al_2O_3 photoanodes achieve a perfect faradaic yield of 100%. Hematite photoanodes coated with only 4 nm of Al_2O_3 ALD exhibit negligible water oxidation [107].

In 2022, Galiano, Figoli, Bonchio and Carraro et al. discovered that halloysite nanotubes (HNTs) were naturally occurring aluminosilicates with a higher susceptibility to selective surface modification compared to other nanotubes. This is achieved through two methods: functionalizing the aluminol layer on the internal wall via condensation with 2-aminoethyl phosphonic acid or reacting the external silanol groups with 3-aminopropyl triethoxysilane. HNT-APTES/**Ru4-SiW10** with **Ru4-SiW10** on the outer surface exhibits superior catalytic activity than those on the inner surface (but not superior to **Ru4-SiW10**). 3-Aminopropyltriethoxy silane (APTES) uses electrostatic interaction to facilitate the grafting of **Ru4-SiW10** onto the outer surface of the HNTs. In this study, porous membranes for water filtration were fabricated using the composite because the nanostructures can be readily dispersed into porous polyether sulfone (PES) films. In comparison to undoped PES membranes, this approach eliminates phase separation, enhances hydrophilicity, improves porosity, and increases permeability. This method allows for efficient transport of the POM catalyst [108].

Therefore, future studies of water oxidation catalysis can focus on the following: (i) synthesizing new and enhanced Ru-POMs with improved stability; (ii) devising facile approaches to obtain well-defined Ru-POMs with controllable Ru content and high yields; (iii) investigating suitable cations or supports to minimize Ru-POM dissolution.

3.3 Catalysis of organic reactions

Owing to their unparalleled redox and catalytic capabilities, various Ru-POMs have emerged as versatile catalysts for organic reactions, facilitating the oxidation of alkanes, alkenes, and alcohols. In the context of olefin ring formation, Ru^{II} in simple **Ru-PW11** directly interacts with the oxidant to generate an activated metal-oxo intermediate, substantially enhancing the substrate's epoxidation potential. Notably, other catalysts require the prior reduction of Ru^{III} to Ru^{II} for activation. The inherent insolubility of Ru-POMs in the reaction environment allows for their convenient recycling. As the reaction proceeds, the accumulation of activated species enhances their interaction with alkenes, leading to a progressive increase in epoxide formation. The reactivity trend among cyclic olefins follows the order cyclohexene > cis-cyclooctene. The lower conversion observed for cis-cyclooctene implies that it undergoes more strain compared to cyclohexene. This strain makes it more challenging for cis-cyclooctene to interact effectively with the active Ru^{II} sites during the reaction. Ring size and strain are likely contributing factors, potentially hindering the oxidation process [43]. Furthermore, the simple **Ru-PW11** can catalyze cyclohexane and other organic compounds to yield corresponding alcohols and ketones. When compared to other metals in the same POM structure, Ru demonstrates superior properties (Ru > Rh > Co ~ Fe) owing to its favorable coordination environment [109]. Ru-POMs also exhibit good activity in the catalytic oxidation of olefins using hydrogen peroxide as the oxidant [14, 110].

Other molybdenum/vanadium-containing POMs also exhibit high catalytic activity in the oxidation of various alcohols, such as benzyl alcohol, p-methylbenzyl alcohol, cyclohexanol, 1-octanol, and 2-octanol, yielding aldehydes, ketones, or carboxylic acids. The selectivity of the reaction varies depending on the specific POM used. This catalytic activity is attributed to the synergistic combination of the Ru fragment and the POM unit in the cluster POMs. This unique structure facilitates the formation of a crucial metal–alcoholate intermediate, which plays a key role in the catalytic aerobic oxidation process [84, 86].

Leveraging the insolubility of $[(n\text{-}C_4H_9)_4N]_4H_4[SiW_{11}Ru^{III}(H_2O)O_{39}]\cdot 2H_2O$ in solvents such as isobutyl acetate, tert-butylacetate, and trifluorotoluene, this POM can function as a heterogeneous catalyst under diverse reaction conditions. For the oxidation of alkanes and alcohols, the reaction setup involves 1 mmol of substrate, 0.5 mmol of catalyst, 3 mL of isobutyl acetate, a temperature of 383 K, and an oxygen atmosphere. This catalytic system demonstrates versatility in oxidizing various alkanes and efficiently converting alcohols to their corresponding carbonyl compounds with high to quantitative yields. Notably, the absence of the catalyst considerably hinders the reaction, as evidenced by a mere 4% conversion when using a mixture of $RuCl_3$ and the POMs precursor [36].

$K_5NaH_{10}[\{Ru_4(H_2O)_n\}(WO_2)_4(AsW_9O_{33})_4]\cdot mH_2O$ exhibits remarkable structural stability and a distinctive geometry, enabling it to catalyze the oxidation of alcohols. In the specific case of 1-(4-chlorophenyl)ethanol oxidation to 4'-chloroacetophenone, this POM and its analogs achieve reaction yields ranging from 86.8% to ~ 98.5% in a short reaction time of 2 h under mild conditions. The

catalytic efficiency of the POMs is influenced by the position of the functional group on the aromatic ring, with para and meta substitutions showing higher reactivity compared to ortho substitutions. Notably, the POMs exhibit limitations in catalyzing the oxidation of long-chain alcohols to their corresponding ketones. However, POMs with reduced aqua ligands and subjected to high-temperature heat treatment demonstrate enhanced catalytic properties. The absence of inner water ligands in the coordination environment of the Ru^{III} ions in the POM creates a spacious environment that allows tert-Butyl hydroperoxide (TBHP) (aq.), the oxidant, to easily access the active sites from in the cage. This accessibility results in an increase in the number of active sites available for catalysis. However, substrates with larger-structured ligands may encounter steric hindrance, which can hinder their interaction with the active sites and limit the reaction's efficiency [91].

Numerous Ru-POMs possess the ability to catalyze the oxidation of long-chain alkanes to alcohols or ketones [70, 73, 82, 111]. High-valent Ru-POMs follow a free radical mechanism that can be summarized in four steps, as described by Bi et al. for the example of $Cs_3(NH_4)[\{Ru_4O_6(H_2O)_9\}_2Sb_2W_{20}O_{68}(OH)_2]\cdot 9H_2O$ (**SbWRu**):

$$Ru^{IV}+RCH_2R^1 \rightarrow +H^+ +RCH\cdot R^1 \quad (6)$$

$$RCH\cdot R^1 + O_2 \rightarrow RCH(OO)\cdot R^1 \quad (7)$$

$$RCH(OO)\cdot R^1 + R^2CH_2R^3 \rightarrow RCH(OOH)R^1 + R^2CH\cdot R^3 \quad (8)$$

$$Ru^{III} + RCH(OOH)R^1 \rightarrow RCH(O)\cdot R^1 + OH^- + Ru^{IV} \quad (9)$$

Equation (6): An active Ru^{IV} site in the **SbWRu** catalyst is initially generated from n-tetradecane through a one-electron transfer reaction. Simultaneously, Ru^{IV} is reduced to Ru^{III}, and free radicals RCH·R1 are formed.

Equation (7): Peroxyl radicals $RCH(OO\cdot)R^1$ are produced via the reaction between the free radicals $RCH\cdot R^1$ and oxygen molecules.

Equation (8): The peroxyl radicals $RCH(OO\cdot)R^1$ react with n-tetradecane to generate peroxide $RCH(OOH)R^1$ and an additional set of free radicals $R^2CH\cdot R^3$.

Equation (9): The peroxide $RCH(OOH)R^1$ can oxidize Ru^{III} back to Ru^{IV}.

The initial formation of $RCH\cdot R^1$ is a crucial step in the oxidation of n-tetradecane, and the catalyst plays a vital role in facilitating the generation of these free radicals [112].

Ru-POMs can also catalyze the oxidation of nitrogen and sulfur atoms in organic compounds. $Cs_2Na_4H_7[(SbW_9O_{33})_6\{Ru(H_2O)_5\}(RuCl_3)(RuO_6)_2\{W(H_2O)\}_6(WO)_4\{WO_2(H_2O)\}_2\{WO_2(H_2O)_2\}_2\{WO_5(H_2O)\}]\cdot 43H_2O$ (denoted as **Ru-POM-OC-1**), synthesized by Niu et al., can selectively catalyze the conversion of anilines to azobenzenes, azoxybenzenes, nitrosobenzenes, and nitrobenzols, with conversions reaching up to 99%. This high efficiency may be attributed to the calculated highest occupied molecular orbit (HOMO) level of 0.97 eV (vs. RHE) and lowest unoccupied molecular orbital (LUMO) level of –0.68 eV (vs. RHE), which make the catalytic cycle thermodynamically favorable.

As indicated in Table 6, the reaction's result is influenced by reaction time, solvent, and additives. Notably, in the case of aniline with a fluorine substituent in the inner ortho position (Table 6, entry 2), oxidation is also possible. However, for aniline with a methyl substituent in the inner ortho position, the reactions proceed with lower yields compared to other substitution positions. Regarding the reaction mentioned in Table 6, entry 4, aniline with a methyl substituent in the ortho position can also undergo oxidation in this catalytic system. This marks the first time a closed catalytic redox cycle has been established between anilines and their corresponding oxidative products (anilines → azoxybenzenes → azobenzenes → nitrosobenzenes → nitrobenzols → anilines) with maximum functionalization. Furthermore, a positive correlation exists between the composition of the catalytic site and the catalytic activity [96].

For sulfur-containing organic compounds, **$(Ru2)_2As4W40$**, synthesized by Niu et al., exhibits high selectivity. Notably, the reaction of dialkyl sulfides and certain alkyl aryl sulfides, such as ethyl phenyl sulfide, 4-methylthioanisole, and 4-methoxythioanisole, with this catalyst leads to complete transformation and 100% selectivity to the corresponding sulfones.

Table 6 **Ru-POM-OC-1**'s selective catalytic oxidation of anilines to various products[a]

Entry	Reaction	Condition	Yield (%)	Remark
1	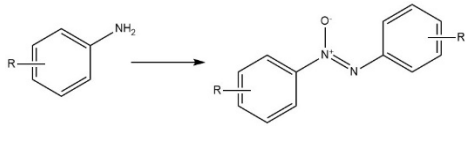	Catalyst (0.1 mol%) 30% H_2O_2 (2 eq.) Na_2HAsO_4 (0.05 eq.) MeOH (1 mL), 40 °C, 12 h	63–97	The alkyl longer than Me only exists on the para-position (except OEt); aniline with F on the meta-position only have yield of 63% (other are all > 80%).
2	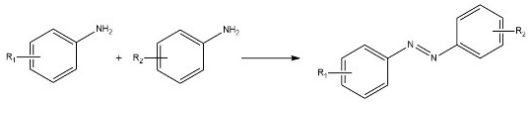	Catalyst (0.1 mol%) 30% H_2O_2 (1.6 eq.) $Na_2S_2O_8$ (0.05 eq.) MeOH (3 mL), 40 °C, 24 h	63–91	The lowest yield comes from the Me on the inner ortho-position, with F on inner ortho-position or meta position are both 74%, other functional group on the para-position are all yields higher than 78%.
3		Catalyst (0.025 mol%) 30% H_2O_2 (1.4 eq.) $Na_2S_2O_8$ (0.05 eq.) toluene (1 mL), 30 °C, 1 h	68–85	The halogen group have lower yields than others except Me on the ortho-position (71%), when Cl on the meta=position yield the lowest (only Cl except Me). Yield of Cl > Br > F
4	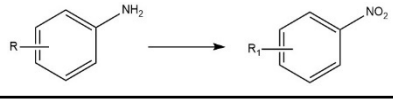	Catalyst (0.05 mol%) 30% H_2O_2 (5.0 eq.) K_2CO_3 (0.05 eq.) MeOH (1 mL), 40 °C, 2 h	77–95	The OEt on the ortho-position yield the lowest.

[a]R = Me, Et, n-Bu, i-Pr, t-Bu, OMe (for entries 2 and 4), OEt (for entries 1, 2, 4), F, Cl (for entries 2, 3, 4), Br (for entries 2, 3, 4). The dosage of $ArNH_2$ in all reactions is 1.0 mmol. The highest yield comes from which R = none except entry 3 which is comes from Et on the para-position.

In contrast, achieving comparable conversion and selectivity for diphenyl thioether requires extending the reaction time to 90 min, possibly owing to the reduced electron density of the sulfur atom in this compound. However, when it comes to the oxidation of more resistant sulfur-containing compounds, only minimal conversions are achieved, indicating their stability even at higher temperatures. Notably, when the reactions are performed in methanol under the optimized conditions, sulfoxides become the major products with high conversions (96.6%–98.3%) and good selectivity (79%–89%). The exception is diphenyl thioether, which shows 48% conversion with 96% selectivity toward the sulfoxide after 120 min [90]. Although $NaWO_4{\cdot}H_2O$ and the mixture of $NaWO_4{\cdot}H_2O$ and $RuCl_3$ can also achieve 89% and 90% conversion, respectively ($RuCl_3$ alone results in low conversion), these results suggest that the POM unit is the primary catalytic center. However, these systems can only function as homogeneous catalysts in the reaction. Therefore, **$(Ru2)_2As4W40$** demonstrate superior performance in these reactions. However, the exact contribution of the Ru centers requires further investigation. The two studies by Niu and Wang et al. highlight the potential of Ru-POMs and demonstrate that rational design based on their designability can broaden their applications.

Modifying the ligand can also lead to the discovery of new catalytic activities. In 2019, Patel et al. attached chiral (R(-)-1-cyclohexylethylamine (Cy)) to the Ru in a Keggin-type POM, creating a heterogeneous catalyst that is the first Ru–POM to facilitate the formation of styrene oxide [113]. Furthermore, combining Ru-POMs with suitable supports can enhance their catalytic activity. For instance, a cellulose/propylamine-modified silica hybrid material has been used to support the Ru-POMs (α-$[SiW_9O_{37}Ru^{III}_3(H_2O)_xCl_{3-x}]^{(10-x)-}$) (denoted as **Ru-POM-CSH**, ca. 1.4% w/w) via the sol–gel synthesis method. This material exhibits a remarkably low bulk density (0.19 $g{\cdot}cm^{-3}$) and high porosity (80%). After undergoing more than 400 turnover cycles, the optimized catalyst exhibits excellent catalytic activity and stability during the heterogeneous aerobic oxidation of formaldehyde in the gas phase at room temperature. With only carbon dioxide and water as the major oxidation products, this suggests that the catalyst has the potential for the complete mineralization of formaldehyde present in contaminated air. However, the continuous purification of air using **Ru-POM-CSH** material will depend on the level of CH_2O concentration [114].

A novel "notched-POM" approach has been developed for synthesizing a composite that features atomically dispersed noble-metal atoms anchored onto a uniform subsupport of WO_x clusters embedded in a carbon-nitrogen matrix. In 2021, Wang et al. reported a new "notched-POM" approach for synthesizing a composite, which was equivalent to loading Ru-POMs onto a carbon-nitrogen carrier. This approach involves an anion exchange process where $[PW_{11}O_{39}\{Ru(arene)(H_2O)\}]^{5-}$ is added to a suspension solution containing a preprepared anionic polymer coated on SiO_2. The resulting powder is then pyrolyzed in an argon atmosphere. Finally, the product is obtained by etching with ammonium hydrogen fluoride to remove the SiO_2 template. The synergistic effect of the Ru active center, the WO_x subsupport clusters, and the carbon-nitrogen substrate considerably enhance the catalytic activity of Ru1@WO_x/CN for the conversion of levulinic acid to γ-valerolactone (GVL) (conversion ~ 100%), which is better than Ru1/CN (conv. = 17%) and Ru1@WO_x (conv. = 13%) [115].

The strategy of modifying cations to enhance catalytic activity has also been used. In 2023, Wang and Hou group developed a monosubstituted Ru-POM-based ionic liquid ($[TOMA_6SiW_{11}O_{39}Ru(DMSO)]$, TOMA = methyltrioctylammonium, denoted as Ru-POM-IL) by introducing stoichiometric quaternary ammonium salts into **Ru-PW11**. This ionic liquid exhibits a melting point of approximately 95–96 °C and possesses properties similar to conventional ionic liquids, such as immiscibility with non-polar solvents, high thermal stability, negligible volatility, and excellent miscibility with most organic solvents, excluding non-polar alkanes and water. Despite the low crystallinity of the POM, in combination with 1-butyl-3-methyl-imidazolium acetate (BMImOAc), it can effectively catalyze the N-formylation of amines with CO_2/H_2 to produce formamides without requiring additional additives [116].

Ru-POMs possess the ability to catalyze a wide range of challenging organic reactions. This versatility can be attributed to the adjustable valence of the Ru catalytic site in the POM and the good solubility of certain Ru–POMs, which enables them to function as heterogeneous catalysts. Additionally, modifications to the terminal ligands, the POM framework, the substrate, or the cations have proven to be effective strategies for enhancing the synergistic effects and obtaining optimal catalysts.

3.4 Other applications

Besides their catalytic capabilities, Ru-POMs exhibit a range of notable properties. This section will provide a brief overview of their proton conduction properties and medical applications

3.4.1 Conductive capability

$H_6[Ru(H_2O)FeW_{11}O_{39}]{\cdot}18H_2O$ exhibits a high proton conductivity of 4.51×10^{-3} $S{\cdot}cm^{-1}$ at room temperature (22 °C), classifying it as a solid high-proton conductor (calculated from Fig. 21). This exceptional conductivity may be attributed to the presence of the Ru–Fe bond, which enhances the electron conductivity [46]. In contrast, $Na_{5.5}H_{6.5}[(SbW_9O_{33})_2\{WO_2(OH)\}_2\{WO_2\}RuC_7H_3NO_4]{\cdot}36H_2O$ demonstrates an effective proton conductivity of 2.97×10^{-2} $S{\cdot}cm^{-1}$ at 348 K and 75% RH, which could be attributed to its unique interlayer structure. This interlayer is fully confined and consists of hydrogen atoms from interlayer crystal waters, organic ligands, and acidic protons. The interlayer serves as the primary transport channel for protons. Furthermore, the interlayer organic ligands and acidic protons form a stable hydrogen bond network, which is resistant to higher temperatures. At 423 K and 75% RH, the material maintains a high conductivity of 1.99×10^{-2} $S{\cdot}cm^{-1}$,

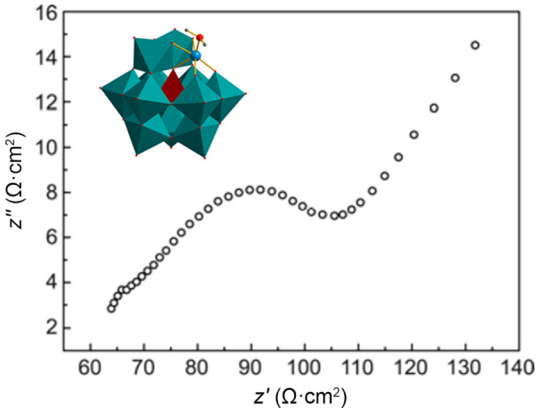

Figure 21 EIS of the $H_6[Ru(H_2O)FeW_{11}O_{39}]{\cdot}18H_2O$ at 22 °C. The figure is reprinted from the permission from Ref. [46], © Xu, S. X. et al. 2011.

highlighting the considerable role of the crystal and microstructure of POM-based layered ionic crystals in proton conduction [74].

3.4.2 *Composition monitoring*

In 2020, Ma et al. successfully synthesized a composite film with enhanced electrocatalytic activity for ascorbic acid (AA) detection by incorporating graphene and $[Ru^{II}(bpy)_3]^{2+}$ into the POM PMo_9V_3. The resulting sensor exhibited remarkable analytical performance, with a wide concentration range of 7.5×10^{-7} to 2.07×10^{-4} M and a low detection limit of 1.0×10^{-7} M. This performance is comparable or even superior to previously reported AA sensors. Additionally, the sensor demonstrated excellent anti-interference properties toward other substances, including dopamine, citric acid, sucrose, fructose, L-glutamic acid, L-tryptophan, and L-cysteine [117].

3.4.3 *Hole scavenging from photogenerated*

In addition, **Ru4-SiW10** exhibits rapid hole scavenging capabilities for both photogenerated Ru^{III} species in homogeneous solution and on a sensitized semiconductor surface. This swift performance is probably attributed to of remarkable properties of catalyst **Ru4-SiW10**, including its high negative charge which enhances close interaction with positively charged oxidants, and the low reorganizational energy resulting from terminal ligands that securely bind and effectively shield the redox active $\{Ru_4\}$ core from the surrounding solvent. The fast rate of hole scavenging is an excellent premise for the use of the new catalyst in practical water splitting photochemical devices [118].

4 Conclusion and prospect

In summary, Ru-POMs with Ru(IV) state have been widely used in organocatalysis, electrocatalysis, and photocatalysis etc. due to their excellent designability and redox properties. For example, **Ru-POM-OC-1** firstly established a closed catalytic redox cycle between anilines and its corresponding oxidative products. The method of adding proper additive has been also firmed to further improve the properties, such as PDI-NO, which could increase the conductivity of the catalytic system. However, the low yield and the strict synthesis conditions limited the widely applications of fascinating Ru-POMs. How to improve the yields of the Ru-POMs with multi-Ru cores is worth further studying. We could also concentrate on the Ru-POMs with open structure such as multi-substituted Ru-POMs and the mono-substituted Ru POMs with higher yields. Suitable supports or ligands are suggested to stabilize the Ru-POMs to improve their stability and enhance their catalytic properties. Moreover, porous MOFs could be used to encapsulate the Ru-POMs to inhibit the aggregation of Ru-POMs and achieve their molecular catalysis while realizing their recovery. Mixing other metals with Ru in Ru-POMs would be also an effective way to enhance the catalysis activity with the help of synergistic effect. For the future study, with the development of renewable energy, it is predicted that more Ru-POMs clusters will be developed for electrocatalytic organic synthesis, especially for the electrocatalytic oxidation of alkanes to alcohols, alcohol to aldehydes, or aldehydes to acids. Moreover, the applications of Ru-POMs on the biology and medicines would be promising. To further understand the mechanism of the catalytic ability of the Ru-POMs, the relationships between the structures and properties should be further studied such as the amount of Ru sites and the catalytic properties.

Acknowledgements

This work was supported by the National Natural Science Foundation of China (Nos. 22171287 and 52303274), Taishan Scholar Project of Shandong Province (No. tsqn202103046), Natural Science Foundation of Shandong Province (Nos. ZR2024QB076 and ZR2022QE175), Young Innovative Science and Technology Support Program for Universities of Shandong Province, China (Nos. 2021KJ014 and 2023KJ280), and Fundamental Research Funds for the Central Universities (Nos. 24CX07007A and 22CX01002A-1).

Declaration of competing interest

The authors have no competing interests to declare that are relevant to the content of this article.

Author contribution statement

Q. M. C.: Data curation, investigation, visualization, writing – original draft. R. L. G.: Visualization, writing – review & editing. Y. F. W.: Writing – review & editing. J. S. X.: Writing – review & editing. Q. Y. Z.: Writing – review & editing. M. Z. Z.: Writing – review & editing. X. Y. Q.: Writing – review & editing. M. H. L.: Supervision, writing – review & editing. Y. C. H.: Conceptualization，funding acquisition, supervision, writing – review & editing.

Use of AI statement

None.

References

[1] Lian, X. K.; Chen, H. B.; Lin, Y. D.; Li, X. X.; Zheng, S. T. Polyoxometalate-based all-inorganic open frameworks. *Coord. Chem. Rev.* **2023**, *497*, 215440.

[2] Chen, X. F.; Wu, H. Z.; Shi, X. J.; Wu, L. X. Polyoxometalate-based frameworks for photocatalysis and photothermal catalysis. *Nanoscale* **2023**, *15*, 9242–9255.

[3] Zhang, H. C.; Fu, S. Y. Polyoxometalate as an effective catalyst for catalytic lignin into value-added molecules. *ChemCatChem* **2024**, *16*, e20230124.

[4] Yue, Z. Y.; Wang, R. J.; Li, J. L.; Tang, M. L.; Yang, L.; Gu, H.; Wang, X. J.; Sun, T. D. Recent advances in polyoxometalate based nanoplatforms mediated reactive oxygen species cancer therapy. *Chem.—Asian J.* **2023**, *18*, e202300749.

[5] Li, L.; Yu, Y. T.; Hua, Y.; Li, X. N.; Zhang, H. Recent progress in polyoxometalate-viologen photochromic hybrids: Structural design, photochromic mechanism, and applications. *Inorg. Chem. Front.* **2023**, *10*, 1965–1985.

[6] Lai, Q. S.; Li, X. X.; Zheng, S. T. All-inorganic POM cages and their assembly: A review. *Coord. Chem. Rev.* **2023**, *482*, 215077.

[7] Qian, D. Q.; Lin, Y. D.; Xiao, H. P.; Wu, B.; Li, X. X.; Zheng, S. T. Advances in coinage-metal-substituted polyoxometalates: A review. *Polyoxometalates* **2024**, *3*, 9140040.

[8] Guan, Y.; Xiao, H. P.; Li, X. X.; Zheng, S. T. Recent advances on the synthesis, structure, and properties of polyoxotantalates. *Polyoxometalates* **2023**, *2*, 9140023.

[9] Zeb, Z.; Huang, Y. C.; Chen, L. L.; Zhou, W. B.; Liao, M. H.; Jiang, Y. Y.; Li, H. T.; Wang, L. M.; Wang, L.; Wang, H. et al. Comprehensive overview of polyoxometalates for electrocatalytic hydrogen evolution reaction. *Coord. Chem. Rev.* **2023**, *482*, 215058.

[10] Putaj, P.; Lefebvre, F. Polyoxometalates containing late transition and noble metal atoms. *Coord. Chem. Rev.* **2011**, *255*, 1642–1685.

[11] Liu, M.; Deng, W. P.; Zhang, Q. H.; Wang, Y. L.; Wang, Y. Polyoxometalate-supported ruthenium nanoparticles as bifunctional heterogeneous catalysts for the conversions of cellobiose and cellulose into sorbitol under mild conditions. *Chem. Commun.* **2011**, *47*, 9717–9719.

[12] Neumann, R.; Abu-Gnim, C. A ruthenium heteropolyanion as catalyst for alkane and alkene oxidation. *J. Chem. Soc., Chem. Commun.* **1989**, 1324–1325.

[13] Rong, C. Y.; Pope, M. T. Lacunary polyoxometalate anions are pi-acceptor ligands. Characterization of some tungstoruthenate(II,III,IV,V) heteropolyanions and their atom-transfer reactivity. *J. Am. Chem. Soc.* **1992**, *114*, 2932–2938.

[14] Neumann, R.; Khenkin, A. M. Noble metal (RuIII, PdII, PtII) substituted "sandwich" type polyoxometalates: Preparation, characterization, and catalytic activity in oxidations of alkanes and alkenes by peroxides. *Inorg. Chem.* **1995**, *34*, 5753–5760.

[15] Bagno, A.; Bonchio, M.; Sartorel, A.; Scorrano, G. Microwave-assisted rapid incorporation of ruthenium into lacunary keggin-type polyoxotungstates: One-step synthesis, ^{99}Ru, ^{183}W NMR characterization and catalytic activity of $[PW_{11}O_{39}Ru^{II}(DMSO)]^{5-}$. *Eur. J. Inorg. Chem.* **2000**, *2000*, 17–20.

[16] Geletii, Y. V.; Botar, B.; Kögerler, P.; Hillesheim, D.; Musaev, D.; Hill, C. An all-inorganic, stable, and highly active tetraruthenium homogeneous catalyst for water oxidation. *Angew. Chem., Int. Ed.* **2008**, *47*, 3896–3899.

[17] Li, H. F.; Chen, W. J.; Yuan, Z. L.; Jin, Y. Z.; Zhao, Y. J.; Ma, P. T.; Niu, J. Y.; Wang, J. P. Controlled assembly of Ru-containing polyoxometalates for photocatalytic activity of the primary amine coupling reaction. *Inorg. Chem.* **2022**, *61*, 9935–9945.

[18] Furukawa, H.; Nakamura, T.; Inagaki, H.; Nishikawa, E.; Imai, C.; Misono, M. Oxidation of cyclopentene with hydrogen peroxide catalyzed by 12-heteropoly acids. *Chem. Lett.* **1988**, *17*, 877–880.

[19] Shimizu, M.; Orita, H.; Hayakawa, T.; Takehira, K. A convenient synthesis of alkyl-substituted p-benzoquinones from phenols by a H_2O_2/heteropolyacid system. *Tetrahedron Lett.* **1989**, *30*, 471–474.

[20] Yamawaki, K.; Yoshida, T.; Nishihara, H.; Ishii, Y.; Ogawa, M. Chemoselective oxidation of secondary hydroxy functions catalyzed by $[PMo_{12}O_{40}]^{3-}[C_5H_5N^+(CH_2)_{15}CH_3]_3$. *Synth. Commun.* **1986**, *16*, 537–541.

[21] Katsoulis, D. E.; Pope, M. T. New chemistry for heteropolyanions in anhydrous nonpolar solvents. Coordinative unsaturation of surface atoms. Polyanion oxygen carriers. *J. Am. Chem. Soc.* **1984**, *106*, 2737–2738.

[22] Piepgrass, K.; Pope, M. T. Oxygen atom transfer chemistry of heteropolytungstate 'browns' in nonaqueous solvents. *J. Am. Chem. Soc.* **1989**, *111*, 753–754.

[23] Bart, J. C.; Anson, F. C. Coordination, electron transfer and catalytic chemistry of a ruthenium-substituted heteropolytungstate anion as revealed in its electrochemical behavior. *J. Electroanal. Chem.* **1995**, *390*, 11–19.

[24] Chu, X. X.; Wang, L.; Li, J. R.; Xu, H. Strategies for promoting catalytic performance of Ru-based electrocatalysts towards oxygen/hydrogen evolution reaction. *Chem. Rec.* **2023**, *23*, e202300013.

[25] Li, Y. W.; Feng, L. G. Recent advances and perspectives in Ru hybrid electrocatalysts for the hydrogen evolution reaction. *Energy Fuels* **2023**, *37*, 8079–8098.

[26] Nguyen, T. B.; Sherpa, K.; Chen, C. W.; Chen, L.; Dong, C. D. Breakthroughs and prospects in ruthenium-based electrocatalyst for hydrogen evolution reaction. *J. Alloys Compd.* **2023**, *968*, 172020.

[27] Li, C. L.; Chen, L. Y.; Dou, D.; Wang, H. B.; Zhao, Q. P.; Cong, Y. Y. Recent research progress on ruthenium-based catalysts at full pH conditions for the hydrogen evolution reaction. *Ionics* **2023**, *29*, 4987–5001.

[28] Kim, J.; Lee, J. Recent progress in strategies for ruthenium-based electrocatalysts for alkaline hydrogen evolution and oxidation reactions. *Energy Fuels* **2023**, *37*, 17765–17781.

[29] Zhu, J.; Hu, L. S.; Zhao, P. X.; Lee, L. Y. S.; Wong, K. Y. Recent advances in electrocatalytic hydrogen evolution using nanoparticles. *Chem. Rev.* **2020**, *120*, 851–918.

[30] Hambourger, M.; Moore, G. F.; Kramer, D. M.; Gust, D.; Moore, A. L.; Moore, T. A. Biology and technology for photochemical fuel production. *Chem. Soc. Rev.* **2009**, *38*, 25–35.

[31] Hammarström, L.; Hammes-Schiffer, S. Artificial photosynthesis and solar fuels. *Acc. Chem. Res.* **2009**, *42*, 1859–1860.

[32] Sartorel, A.; Carraro, M.; Scorrano, G.; Zorzi, R. D.; Geremia, S.; Mcdaniel, N. D.; Bernhard, S.; Bonchio, M. Polyoxometalate embedding of a tetraruthenium(IV)-oxo-core by template-directed metalation of $[\gamma\text{-}SiW_{10}O_{36}]^{8-}$: A totally inorganic oxygen-evolving catalyst. *J. Am. Chem. Soc.* **2008**, *130*, 5006–5007.

[33] Sartorel, A.; Miró, P.; Salvadori, E.; Romain, S.; Carraro, M.; Scorrano, G.; Valentin, M. D.; Llobet, A.; Bo, C.; Bonchio, M. Water oxidation at a tetraruthenate core stabilized by polyoxometalate ligands: Experimental and computational evidence to trace the competent intermediates. *J. Am. Chem. Soc.* **2009**, *131*, 16051–16053.

[34] Izarova, N. V.; Pope, M. T.; Kortz, U. Noble metals in polyoxometalates. *Angew. Chem., Int. Ed.* **2012**, *51*, 9492–9510.

[35] Filipek, K. Synthesis, characterization and reactivity of ruthenium complexes of the lacunary Keggin polyoxoanion: $[SiW_{11}O_{39}RuL]^{n-}$, L = H_2O, NO, N_2. *Inorg. Chim. Acta* **1995**, *231*, 237–239.

[36] Yamaguchi, K.; Mizuno, N. Heterogeneously catalyzed liquid-phase oxidation of alkanes and alcohols with molecular oxygen. *New J. Chem.* **2002**, *26*, 972–974.

[37] Sadakane, M.; Higashijima, M. Synthesis and electrochemical behavior of $[SiW_{11}O_{39}Ru^{III}(H_2O)]^{5-}$ and its oxo-bridged dimeric complex $[SiW_{11}O_{39}Ru^{IV}ORu^{III}SiW_{11}O_{39}]^{11-}$. *Dalton Trans.* **2003**, 659–664.

[38] Bi, L. H.; Kortz, U.; Keita, B.; Nadjo, L. The ruthenium(II)-supported heteropolytungstates $[Ru(dmso)_3(H_2O)XW_{11}O_{39}]^{6-}$ (X = Ge, Si). *Dalton Trans.* **2004**, 3184–3190.

[39] Artero, V.; Laurencin, D.; Villanneau, R.; Thouvenot, R.; Herson, P.; Gouzerh, P.; Proust, A. Synthesis, characterization, and photochemical behavior of $\{Ru(arene)\}^{2+}$ derivatives of α-$[PW_{11}O_{39}]^{7-}$: An organometallic way to ruthenium-substituted heteropolytungstates. *Inorg. Chem.* **2005**, *44*, 2826–2835.

[40] Laurencin, D.; Villanneau, R.; Gérard, H.; Proust, A. Experimental and theoretical study of the regiospecific coordination of Ru^{II} and Os^{II} fragments on the lacunary polyoxometalate $[\alpha\text{-}PW_{11}O_{39}]^{7-}$. *J. Phys. Chem. A* **2006**, *110*, 6345–6355.

[41] Lahootun, V.; Besson, C.; Villanneau, R.; Villain, F.; Chamoreau, L. M.; Boubekeur, K.; Blanchard, S.; Thouvenot, R.; Proust, A. Synthesis and characterization of the Keggin-type ruthenium-nitrido derivative $[PW_{11}O_{39}\{RuN\}]^{4-}$ and evidence of its electrophilic reactivity. *J. Am. Chem. Soc.* **2007**, *129*, 7127–7135.

[42] Sadakane, M.; Iimuro, Y.; Tsukuma, D.; Bassil, B. S.; Dickman, M. H.; Kortz, U.; Zhang, Y.; Ye, S.; Ueda, W. Carbonyl-ruthenium substituted α-Keggin-tungstosilicate, $[\alpha\text{-}SiW_{11}O_{39}Ru^{II}(CO)]^{6-}$: Synthesis, structure, redox studies and reactivity. *Dalton Trans.* **2008**, 6692–6698.

[43] Shringarpure, P.; Patel, A. Undecatungstophospho(aqua) ruthenate(II): One pot synthesis, characterization and non-solvent liquid phase aerobic oxidation of alkenes. *Inorg. Chim. Acta* **2009**, *362*, 3796–3800.

[44] Besson, C.; Geletii, Y. V.; Villain, F.; Villanneau, R.; Hill, C. L.; Proust, A. Nitrogen-atom transfer from $[PW_{11}O_{39}Ru^{VI}N]^{4-}$ to PPh_3. *Inorg. Chem.* **2009**, *48*, 9436–9443.

[45] Sadakane, M.; Rinn, N.; Moroi, S.; Kitatomi, H.; Ozeki, T.; Kurasawa, M.; Itakura, M.; Hayakawa, S.; Kato, K.; Miyamoto, M. et al. Preparation and structural characterization of Ru^{II}-DMSO and

Ru^{III}-DMSO-substituted α-Keggin-type phosphotungstates, $[PW_{11}O_{39}Ru^{II}DMSO]^{5-}$ and $[PW_{11}O_{39}Ru^{III}DMSO]^{4-}$, and catalytic activity for water oxidation. *Z. Anorg. Allg. Chem.* **2011**, *637*, 1467–1474.

[46] Xu, S. X.; Wu, X. F.; Wu, Q. Y.; Yan, W. F. Synthesis, characterization and properties of ruthenium-substituted polyoxometallic acid $H_6Ru(H_2O)FeW_{11}O_{39}\cdot 18H_2O$ with Keggin structure. *Chin. Sci. Bull.* **2011**, *56*, 2679–2682.

[47] Ogo, S.; Miyamoto, M.; Ide, Y. Sano, T. Sadajkane, M. Hydrothermal and solid-state transformation of ruthenium-supported Keggin-type heteropolytungstates $[XW_{11}O_{39}\{Ru(II)(benzene)(H_2O)\}]^{n-}$ (X = P (n = 5), Si (n = 6), Ge (n = 6)) to ruthenium-substituted Keggin-type heteropolytungstates. *Dalton Trans.* **2012**, 9901–9907.

[48] Sokolov, M. N.; Adonin, S. A.; Mainichev, D. A.; Sinkevich, P. L.; Vicent, C.; Kompankov, N. B.; Gushchin, A. L.; Nadolinny, V. A.; Fedin, V. P. New {RuNO} polyoxometalate $[PW_{11}O_{39}Ru^{II}(NO)]^{4-}$: Synthesis and reactivity. *Inorg. Chem.* **2013**, *52*, 9675–9682.

[49] Ogo, S.; Shimizu, N.; Ozeki, T.; Kobayashi, Y.; Ide, Y.; Sano, T.; Sadakane, M. Determination of α-Keggin structure of $[GeW_{11}O_{39}Ru^{III}(H_2O)]^{5-}$. Reaction of $[GeW_{11}O_{39}Ru^{III}(H_2O)]^{5-}$ with dimethyl sulfoxide to form $[GeW_{11}O_{39}Ru^{III}(dmso)]^{5-}$ and their structural characterization. *Dalton Trans.* **2013**, 2540–2545.

[50] Shimizu, N.; Ozeki, T.; Shikama, H.; Sano, T.; Sadakane, M. Synthesis and structural characterization of isomers of Ru-substituted Keggin-type germanotungstate with dmso ligand. *J. Cluster Sci.* **2014**, *25*, 755–770.

[51] Liu, B.; Yan, J.; Wang, Y. F.; Yi, X. Y. Redox chemistry of ruthenium ions in mono-substituted Keggin tungstophosphate: A new synthetic extension for ruthenium derivatives based on $[PW_{11}O_{39}Ru^{VI}N]^{4-}$. *Dalton Trans.* **2015**, *44*, 16882–16887.

[52] Nomiya, K.; Torii, H.; Nomura, K.; Sato, Y. Synthesis and characterization of a monoruthenium(III)-substituted Dawson polyoxotungstate derived by Br_2 oxidation of the 1:2 complex of ruthenium(II) and $[\alpha_2\text{-}P_2W_{17}O_{61}]^{10-}$. The reactivity of cis-$[RuCl_2(DMSO)_4]$ as a ruthenium source. *J. Chem. Soc., Dalton Trans.* **2001**, 1506–1512.

[53] Sakai, Y.; Shinohara, A.; Hayashi, K.; Nomiya, K. Synthesis and characterization of two novel, mono-lacunary dawson polyoxometalate-based, water-soluble organometallic ruthenium(II) complexes: Molecular structure of $[\{(C_6H_6)Ru(H_2O)\}(\alpha_2\text{-}P_2W_{17}O_{61})]^{8-}$. *Eur. J. Inorg. Chem.* **2006**, *2006*, 163–171.

[54] Ogo, S.; Shimizu, N.; Nishiki, K.; Yasuda, N.; Mizuta, T.; Sano, T.; Sadakane, M. Preparation and redox studies of α_1- and α_2-isomers of mono-Ru-substituted Dawson-type phosphotungstates with a DMSO ligand: $[\alpha_1/\alpha_2\text{-}P_2W_{17}O_{61}Ru^{II}(DMSO)]^{8-}$. *Inorg. Chem.* **2014**, *53*, 3526–3539.

[55] Nishiki, K.; Ota, H.; Ogo, S.; Sano, T.; Sadakane, M. Preparation and structural characterization of mono-Ru-substituted α_2-dawson-type phosphotungstate with a carbonyl ligand and other Ru(CO)-substituted heteropolytungstates. *Eur. J. Inorg. Chem.* **2015**, *2015*, 2714–2723.

[56] Nishiki, K.; Umehara, N.; Kadota, Y.; López, X.; Poblet, J. M.; Mezui, C. A.; Teillout, A. L.; Mbomekalle, I. M.; de Oliveira, P.; Miyamoto, M. et al. Preparation of α_1- and α_2-isomers of mono-Ru-substituted Dawson-type phosphotungstates with an aqua ligand and comparison of their redox potentials, catalytic activities, and thermal stabilities with Keggin-type derivatives. *Dalton Trans.* **2016**, *45*, 3715–3726.

[57] Mukhacheva, A. A.; Shmakova, A. A.; Volchek, V. V.; Romanova, T. E.; Benassi, E.; Gushchin, A. L.; Yanshole, V.; Sheven, D. G.; Kompankov, N. B.; Abramov, P. A. et al. Reactions of $[Ru(NO)Cl_5]^{2-}$ with pseudotrilacunary $\{XW_9O_{33}\}^{9-}$ (X = As^{III}, Sb^{III}) anions. *Dalton Trans.* **2019**, *48*, 15989–15999.

[58] Ogo, S.; Moroi, S.; Ueda, T.; Komaguchi, K.; Hayakawa, S.; Ide, Y.; Sano, T.; Sadakane, M. Preparation of tetrabutylammonium salt of a mono-Ru(III)-substituted α-Keggin-type silicotungstate with a 4,4'-bipyridine ligand and its electrochemical behaviour in organic solvents. *Dalton Trans.* **2013**, *42*, 7190–7195.

[59] Besson, C.; Chen, S. W.; Villanneau, R.; Izzet, G.; Proust, A. A new synthetic route towards a Ru(III) substituted heteropolytungstate anion. *Inorg. Chem. Commun.* **2009**, *12*, 1042–1044.

[60] Bi, L. H.; Hussain, F.; Kortz, U.; Sadakane, M.; Dickman, M. H. A novel isopolytungstate functionalized by ruthenium: $[HW_9O_{33}Ru^{II}_2(dmso)_6]^{7-}$. *Chem. Commun.* **2004**, 1420–1421.

[61] Quiñonero, D.; Wang, Y.; Morokuma, K.; Khavrutskii, L. A.; Botar, B.; Geletii, Y. V.; Hill, C. L.; Musaev, D. G. The role of the central atom in structure and reactivity of polyoxometalates with adjacent d-electron metal sites. computational and experimental studies of γ-$[(X^{n+}O_4)Ru^{III}_2(OH)_2(M_{FM})_{10}O_{32}]^{(8-n)-}$ for M_{FM} = Mo and W, and X = Al^{III}, Si^{IV}, P^{V}, and S^{VI}. *J. Phys. Chem. B.* **2006**, *110*, 170–173.

[62] Besson, C.; Musaev, D. G.; Lahootun, V.; Cao, R.; Chamoreau, L. M.; Villanneau, R.; Villain, F.; Thouvenot, R.; Geletii, Y. V.; Hill, C. L. et al. Vicinal dinitridoruthenium-substituted polyoxometalates gamma-$[XW_{10}O_{38}\{RuN\}_2]^{6-}$ (X = Si or Ge). *Chemistry* **2009**, *15*, 10233–10243.

[63] Gamelas, J. A. F.; Carapuça, H. M.; Balula, M. S.; Evtuguin, D. V.; Schlindwein, W.; Figueiras, F. G.; Amaral, V. S.; Cavaleiro, A. M. V. Synthesis and characterisation of novel ruthenium multi-substituted polyoxometalates: α,β-$[SiW_9O_{37}Ru_4(H_2O)_3Cl_3]^{7-}$. *Polyhedron* **2010**, *29*, 3066–3073.

[64] Car, P. E.; Guttentag, M.; Baldridge, K. K.; Alberto, R.; Patzke, G. R. Synthesis and characterization of open and sandwich-type polyoxometalates reveals visible-light-driven water oxidation via POM-photosensitizer complexes. *Green Chem.* **2012**, *14*, 1680–1688.

[65] Bi, L. H.; Chubarova, E. V.; Nsouli, N. H.; Dickman, M. H.; Kortz, U.; Keita, B.; Nadjo, L. Dilacunary decatungstates functionalized by organometallic ruthenium(II), $[\{Ru(C_6H_6)(H_2O)\}\{Ru(C_6H_6)\}(\gamma\text{-}XW_{10}O_{36})]^{4-}$ (X = Si, Ge). *Inorg. Chem.* **2006**, *45*, 8575–8583.

[66] Bi, L. H.; Kortz, U.; Dickman, M. H.; Keita, B.; Nadjo, L. Trilacunary heteropolytungstates functionalized by organometallic ruthenium(II), $[(RuC_6H_6)_2XW_9O_{34}]^{6-}$ (X = Si, Ge). *Inorg. Chem.* **2005**, *44*, 7485–7493.

[67] Kikuchi, M.; Ota, H.; López, X.; Nakaya, T.; Tsunoji, N.; Sano, T.; Sadakane, M. Reactivity of a (benzene)ruthenium(II) cation on a di-lacunary γ-Keggin-type silicotungstate and synthesis of a mono-(benzene)ruthenium(II)-attached γ-Keggin-type silicotungstate. *Eur. J. Inorg. Chem.* **2018**, *2018*, 1778–1786.

[68] Bösing, M.; Loose, I.; Pohlmann, H.; Krebs, B. New strategies for the generation of large heteropolymetalate clusters: The β-*B*-SbW_9 fragment as a multifunctional unit. *Chem.—Eur. J.* **1997**, *3*, 1232–1237.

[69] Laurencin, D.; Villanneau, R.; Herson, P.; Thouvenot, R.; Jeannin, Y.; Proust, A. A new organometallic heteropolytungstate related to $[Sb_2W_{22}O_{74}(OH)_2]^{12-}$: Synthesis and structural characterisation of the bis-$\{Ru(p\text{-}cymene)\}^{2+}$-containing anion $[Sb_2W_{20}O_{70}\{Ru(p\text{-}cymene)\}_2]^{10-}$. *Chem. Commun.* **2005**, 5524–5526.

[70] Bi, L. H.; Al-Kadamany, G.; Chubarova, E. V.; Dickman, M. H.; Chen, L. F.; Gopala, D. S.; Richards, R. M.; Keita, B.; Nadjo, L.; Jaensch, H. et al. Organo-ruthenium supported heteropolytungstates: Synthesis, structure, electrochemistry, and oxidation catalysis. *Inorg. Chem.* **2009**, *48*, 10068–10077.

[71] Bi, L. H.; Li, B.; Bi, S.; Wu, L. X. Synthesis and crystal structure of Ru^{III}-supported tungstoantimonate $[Sb_2W_{20}Ru^{III}_2(H_2O)_2(dmso)_6O_{68}]^{4-}$. *J. Solid State Chem.* **2009**, *182*, 1401–1407.

[72] Kalinina, I. V.; Izarova, N. V.; Kortz, U. Bis[tetraruthenium(IV)]-containing polyoxometalates: $[\{Ru^{IV}_4O_6(H_2O)_9\}_2Sb_2W_{20}O_{68}(OH)_2]^{4-}$ and $[\{Ru^{IV}_4O_6(H_2O)_9\}_2\{Fe(H_2O)_2\}_2\{\beta\text{-}TeW_9O_{33}\}_2H]^{-}$. *Inorg. Chem.* **2012**, *51*, 7442–7444.

[73] Zheng, D. M.; Wang, R. Q.; Du, Y.; Hou, G. F.; Wu, L. X.; Bi, L. H. A new organo-ruthenium substituted tungstotellurate: Synthesis,

structural characterization and catalytic properties. *New J. Chem.* **2016**, *40*, 8829–8836.

[74] Yang, M. N.; Li, H. F.; Zhang, Y.; Ji, S. Y.; Chen, W. J.; Ma, P. T.; Wang, J. P.; Niu, J. Y. Organic hybrid antimoniotungstate layered ionic crystal: Synthesis, structure, and interlayer-confined proton conduction. *Inorg. Chem.* **2023**, *62*, 6467–6473.

[75] Neumann, R.; Dahan, M. Molecular oxygen activation by a ruthenium-substituted "Sandwich" type polyoxometalate. *J. Am. Chem. Soc.* **1998**, *120*, 11969–11976.

[76] Neumann, R.; Dahan, M. A ruthenium-substituted polyoxometalate as an inorganic dioxygenase for activation of molecular oxygen. *Nature.* **1997**, *388*, 353–355.

[77] Chen, S. W.; Villanneau, R.; Li, Y. L.; Chamoreau, L. M.; Boubekeur, K.; Thouvenot, R.; Gouzerh, P.; Proust, A. Hydrothermal synthesis and structural characterization of the high-valent ruthenium-containing polyoxoanion $[\{PW_{11}O_{39}\}_2\{(HO)Ru^{IV}–O–Ru^{IV}(OH)\}]^{10-}$. *Eur. J. Inorg. Chem.* **2008**, *2008*, 2137–2142.

[78] Geletii, Y. V.; Besson, C.; Hou, Y.; Yin, Q. S.; Musaev, D. G.; Quiñonero, D.; Cao, R.; Hardcastle, K. I.; Proust, A.; Kögerler, P. et al. Structural, physicochemical, and reactivity properties of an all-inorganic, highly active tetraruthenium homogeneous catalyst for water oxidation. *J. Am. Chem. Soc.* **2009**, *131*, 17360–17370.

[79] Besson, C.; Huang, Z. Q.; Geletii, Y. V.; Lense, S.; Hardcastle, K. I.; Musaev, D. G.; Lian, T. Q.; Proust, A.; Hill, C. L. $Cs_9[(\gamma\text{-}PW_{10}O_{36})_2Ru_4O_5(OH)(H_2O)_4]$, a new all-inorganic, soluble catalyst for the efficient visible-light-driven oxidation of water. *Chem. Commun.* **2010**, *46*, 2784–2786.

[80] Zhao, Y. J.; Wan, R.; Li, H. F.; Zhao, R. K.; Chen, W. J.; Song, H. M.; Ma, P. T.; Niu, J. Y.; Wang, J. P. ^{183}W nuclear magnetic resonance and photocatalysis studies of two ruthenium-decorated isopolyoxometalates $\{Ru_2W_{10}\}$ and $\{Ru_2W_{13}\}$ via pH-induced assemblies. *Inorg. Chem.* **2022**, *61*, 12097–12105.

[81] Bi, L. H.; Hou, G. F.; Li, B.; Wu, L. X.; Kortz, U. Synthesis and crystal structure of pseudo-sandwich-type heteropolytungstates functionalized by organometallic ruthenium(II). *Dalton Trans.* **2009**, *54*, 6345–6353.

[82] Meng, R. Q.; Suo, L.; Hou, G. F.; Liang, J.; Bi, L. H.; Li, H. L.; Wu, L. X. Organo-Ru supported sandwich-type tungstoarsenates: Synthesis, structure and catalytic properties. *CrystEngComm.* **2013**, *15*, 5867–5876.

[83] Artero, V.; Proust, A.; Herson, P.; Villain, F.; Cartier Dit moulin, C.; Gouzerh, P. Synthesis and characterization of the first carbene derivative of a polyoxometalate. *J. Am. Chem. Soc.* **2003**, *125*, 11156–11157.

[84] Khenkin, A. M.; Shimon, L. J. W.; Neumann, R. Preparation and characterization of new ruthenium and osmium containing polyoxometalates, $[M(DMSO)_3Mo_7O_{24}]^{4-}$ (M = Ru(II), Os(II)), and their use as catalysts for the aerobic oxidation of alcohols. *Inorg. Chem.* **2003**, *42*, 3331–3339.

[85] Bi, L. H.; Wang, B.; Hou, G. F.; Li, B.; Wu, L. X. A novel heptatungstovanadate fragment stabilized by organo-ruthenium group: $[HVW_7O_{28}Ru(dmso)_3]^{6-}$. *CrystEngComm.* **2010**, *12*, 3511–3514.

[86] Shi, H. Y.; Zhou, W. Y.; Song, X. M.; Jia, A. Q.; Shi, H. T.; Zhang, Q. F. Ruthenium(II)-supported phosphovanadomolybdates $[Ru(dmso)_3PMo_6V_3O_{32}]^{6-}$ and $[Ru(PMo_6V_3O_{32})_2]^{14-}$, and their use as heterogeneous catalysts for oxidation of alcohols. *New J. Chem.* **2021**, *45*, 1551–1555.

[87] Randall, W. J.; Weakley, T. J. R.; Finke, R. G. Oxidation resistant inorganic-porphyrin analog polyoxometalates. 3. Synthesis and X-ray crystallographic characterization of a new heteropolyoxoanion structural type, the diruthenium-oxo-bridged bimetallic inorganic-porphyrin analog $KLi_{15}[O\{Ru^{IV}Cl(\alpha_2\text{-}P_2W_{17}O_{61})\}_2]\cdot 2KCl\cdot 60H_2O$. *Inorg. Chem.* **1993**, *32*, 1068–1071.

[88] Laurencin, D.; Thouvenot, R.; Boubekeur, K.; Gouzerh, P.; Proust, A. Connecting ruthenium substituted Keggin-type tungstophosphates by oxotungstic bridges: Evidence for the steric effect of $\{RuL_3\}^{2+}$ (L_3 = η^6-arene, $(DMSO)_3$) fragments. *C. R. Chim.* **2012**, *15*, 135–142.

[89] Nsouli, N. H.; Chubarova, E. V.; Al-Oweini, R.; Bassil, B. S.; Sadakane, M.; Kortz, U. Organoruthenium-containing heteropoly-23-tungstate family $[\{Ru(L)\}_2(\alpha\text{-}XW_{11}O_{39})_2WO_2]^{m-}$ (L = benzene, p-cymene; X = Ge^{IV}, Si^{IV}, m = 10; B^{III}, m = 12). *Eur. J. Inorg. Chem.* **2013**, *2013*, 1742–1747.

[90] Han, M. D.; Niu, Y. J.; Wan, R.; Xu, Q. F.; Lu, J. K.; Ma, P. T.; Zhang, C.; Niu, J. Y.; Wang, J. P. A crown-shaped Ru-substituted arsenotungstate for selective oxidation of sulfides with hydrogen peroxide. *Chem.—Eur. J.* **2018**, *24*, 11059–11066.

[91] Li, H. F.; Chen, W. J.; Zhao, Y. J.; Zou, Y.; Zhao, X.; Song, J. P.; Ma, P. T.; Niu, J. Y.; Wang, J. P. Regulating the catalytic activity of multi-Ru-bridged polyoxometalates based on differential active site environments with six-coordinate geometry and five-coordinate geometry transitions. *Nanoscale* **2021**, *13*, 8077–8086.

[92] Chen, W. J.; Li, H. F.; Song, J. P.; Zhao, Y. J.; Ma, P. T.; Niu, J. Y.; Wang, J. P. Binuclear Ru(III)-containing polyoxometalate with efficient photocatalytic activity for oxidative coupling of amines to imines. *Inorg. Chem.* **2022**, *61*, 2076–2085.

[93] Bi, L. H.; Mal, S. S.; Nsouli, N. H.; Dickman, M. H.; Kortz, U.; Nellutla, S.; Dalal, N. S.; Prinz, M.; Hofmann, G.; Neumann, M. Mixed-valence 24-vanadophosphate decorated with six $Ru^{II}(dmso)_3$ groups: $[\{Ru^{II}_3(dmso)_9PV^{V}_{11}V^{IV}Ru^{III}O_{37}(OH)_3\}_2]^{8-}$. *J. Cluster Sci.* **2008**, *19*, 259–273.

[94] Wan, R.; Li, H. F.; Ma, X. Y.; Liu, Z.; Singh, V.; Ma, P. T.; Zhang, C.; Niu, J. Y.; Wang, J. P. Preparation, characterization and electrocatalysis performance of a trimeric ruthenium-substituted isopolytungstate. *Dalton Trans.* **2019**, *48*, 10327–10336.

[95] Wan, R.; Liu, Z.; Ma, X. Y.; Li, H. F.; Ma, P. T.; Zhang, C.; Niu, J. Y.; Wang, J. P. Discovery of two Na^+-centered Silverton-type polyoxometalates $\{NaM_{12}O_{42}\}$ (M = Mo, W). *Chem. Commun.* **2021**, *57*, 2172–2175.

[96] Li, H. F.; Yuan, Z. L.; Chen, W. J.; Yang, M. N.; Sun, Y. H.; Zhang, S. H.; Ma, P. T.; Wang, J. P.; Niu, J. Y. Controllable redox reaction cycle enabled by multifunctional Ru-containing polyoxometalate-based catalysts. *J. Mater. Chem. A* **2023**, *11*, 10813–10822.

[97] Kortz, U.; Savelieff, M. G.; Bassil, B. S.; Dickman, M. H. A large, novel polyoxotungstate: $[As^{III}_6W_{65}O_{217}(H_2O)_7]^{26-}$. *Angew. Chem., Int. Ed.* **2001**, *40*, 3384–3386.

[98] Liu, Y. P.; Zhao, S. F.; Guo, S. X.; Bond, A. M.; Zhang, J.; Zhu, G. B.; Hill, C. L.; Geletii, Y. V. Electrooxidation of ethanol and methanol using the molecular catalyst $[\{Ru_4O_4(OH)_2(H_2O)_4\}(\gamma\text{-}SiW_{10}O_{36})_2]^{10-}$. *J. Am. Chem. Soc.* **2016**, *138*, 2617–2628.

[99] Ding, Y. H.; Li, H. Y.; Hou, Y. Robust polyoxometalate-loaded nickel foam for electrocatalytic oxygen evolution reaction. *Mater. Lett.* **2018**, *221*, 264–266.

[100] Kim, U.; Cho, Y.; Jeon, D.; Kim, Y.; Park, S.; Seo, J.; Lee, J.; Oh, N. K.; Lee, G.; Ryu, J. et al. Zwitterionic conjugated surfactant functionalization of graphene with pH-independent dispersibility: An efficient electron mediator for the oxygen evolution reaction in acidic media. *Small* **2020**, *16*, 1906635.

[101] Zhou, H.; Dong, Y. Y.; Xin, X.; Chi, M. Z.; Song, T. L.; Lv, H. J. Electrocatalytic valorization of 5-hydroxymethylfurfural coupled with hydrogen production using tetraruthenium-containing polyoxometalate-based composites. *J. Mater. Chem. A* **2022**, *10*, 19963–19971.

[102] Sun, F. Y.; Bao, W. J.; Feng, C.; Bi, J. H.; Yue, C. L.; Zhang, C.; Liu, N.; Hao, H. Y.; Lu, Y. K. Construction of ultrafine and highly dispersed $RuSe_2$ on WO_x by "atom-to-cluster" strategy for efficient hydrogen evolution reaction. *Fuel* **2024**, *370*, 131815.

[103] Piccinin, S.; Sartorel, A.; Aquilanti, G.; Goldoni, A.; Bonchio, M.; Fabris, S. Water oxidation surface mechanisms replicated by a totally inorganic tetraruthenium-oxo molecular complex. *Proc. Natl. Acad. Sci. USA* **2013**, *110*, 4917–4922.

[104] Puntoriero, F.; La Ganga, G.; Sartorel, A.; Carraro, M.; Scorrano, G.;

Bonchio, M.; Campagna, S. Photo-induced water oxidation with tetranuclear ruthenium sensitizer and catalyst: A unique 4 × 4 ruthenium interplay triggering high efficiency with low-energy visible light. *Chem. Commun.* **2010**, *46*, 4725–4727.

[105] Ishizuka, T.; Ohkawa, S.; Ochiai, H.; Hashimoto, M.; Ohkubo, K.; Kotani, H.; Sadakane, M.; Fukuzumi, S.; Kojima, T. A supramolecular photocatalyst composed of a polyoxometalate and a photosensitizing water-soluble porphyrin diacid for the oxidation of organic substrates in water. *Green Chem.* **2018**, *20*, 1975–1980.

[106] Bonchio, M.; Syrgiannis, Z.; Burian, M.; Marino, N.; Pizzolato, E.; Dirian, K.; Rigodanza, F.; Volpato, G. A.; La Ganga, G.; Demitri, N. Hierarchical organization of perylene bisimides and polyoxometalates for photo-assisted water oxidation. *Nat. Chem.* **2019**, *11*, 146–153.

[107] Lauinger, S. M.; Piercy, B. D.; Li, W.; Yin, Q.; Collins-Wildman, D. L.; Glass, E. N.; Losego, M. D.; Wang, D. W.; Geletii, Y. V.; Hill, C. L. Stabilization of polyoxometalate water oxidation catalysts on hematite by atomic layer deposition. *ACS Appl Mater Interfaces.* **2017**, *9*, 35048–35056.

[108] Yu, J. Y.; Boudjelida, S.; Galiano, F.; Figoli, A.; Bonchio, M.; Carraro, M. Porous polymeric membranes doped with halloysite nanotubes and oxygenic polyoxometalates. *Adv. Mater. Interfaces* **2022**, *9*, 2102152.

[109] Matsumoto, Y.; Asami, M.; Hashimoto, M.; Misono, M. Alkane oxidation with mixed addenda heteropoly catalysts containing Ru(III) and Rh(III). *J. Mol. Catal. A: Chem.* **1996**, *114*, 161–168.

[110] Morris, A. M.; Anderson, O. P.; Finke, R. G. Reinvestigation of a Ru_2-incorporated polyoxometalate dioxygenase precatalyst, "$[WZnRu_2^{III}(H_2O)(OH)(ZnW_9O_{34})_2]^{11-}$": Evidence for marginal, ≤ 0.2 equivalents of Ru incorporation plus faster catalysis by physical mixtures of $[Ru^{II}(DMSO)_4Cl_2]$ and the parent polyoxometalate $[WZn_3(H_2O)_2(ZnW_9O_{34})_2]^{12-}$. *Inorg. Chem.* **2009**, *48*, 4411–4420.

[111] Ma, Z. Y.; Yu, T.; Bi, L. H. Ru-containing polyoxometalate fabricated on graphene oxide: Preparation, characterization and catalytic activity. *J. Solid State Chem.* **2019**, *275*, 16–22.

[112] Ma, Z. Y.; Wang, R. Q.; Yu, T.; Bi, L. H. Preparation, characterization and catalytic performance of polyoxometalate immobilized on the surface of halloysite. *J. Mater. Sci.* **2019**, *54*, 3817–3831.

[113] Patel, A.; Patel, K. Polyoxometalate based hybrid chiral material: Synthesis, characterizations and aerobic asymmetric oxidation reaction. *J. Coord. Chem.* **2019**, *72*, 3417–3429.

[114] Gamelas, J. A. F.; Oliveira, F.; Evtyugina, M. G.; Portugal, I.; Evtuguin, D. V. Catalytic oxidation of formaldehyde by ruthenium multisubstituted tungstosilicic polyoxometalate supported on cellulose/silica hybrid. *Appl. Catal. A: Gen.* **2016**, *509*, 8–16.

[115] Han, Y. H.; Dai, J.; Xu, R. R.; Ai, W. Y.; Zheng, L. R.; Wang, Y.; Yan, W. S.; Chen, W. X.; Luo, J.; Liu, Q.; et al. Notched-polyoxometalate strategy to fabricate atomically dispersed Ru catalysts for biomass conversion. *ACS Catal.* **2021**, *11*, 2669–2675.

[116] Ma, Y.; Chen, C.; Jiang, Y. J.; Wei, X. J.; Liu, Y.; Liao, H. Y.; Wang, H. F.; Dai, S.; An, P. F.; Hou, Z. S. Ruthenium single-atom anchored in polyoxometalate-ionic liquids for N-formylation of amines with CO_2 and H_2. *ACS Catal.* **2023**, *13*, 10295–10308.

[117] Guo, D. X.; Zhou, C. L.; Tan, L. C.; Ma, H. Y.; He, R. R.; Pang, H. J.; Wang, X. M. Electrochemical ascorbic acid sensor of composite film based on Keggin-type vanadium-substituted polyoxometalates decorated with graphene and $Ru(bpy)_3^{2+}$. *Colloids. Surf. A: Physicochem. Eng. Asp.* **2020**, *592*, 124550.

[118] Orlandi, M.; Argazzi, R.; Sartorel, A.; Carraro, M.; Scorrano, G.; Bonchio, M.; Scandola, F. Ruthenium polyoxometalate water splitting catalyst: Very fast hole scavenging from photogenerated oxidants. *Chem. Commun.* **2010**, *46*, 3152–3154.

Qingmiao Cai is currently majoring in material chemistry and pursuing bachelor's degree at China University of Petroleum (East China). His main research interests are related to using ruthenium-containing polyoxometalate clusters to design electrocatalysts with high-performance in acidic oxygen evolution reaction.

Yichao Huang received his Ph.D. degree from Tsinghua University in 2019. He is currently working as a professor at the School of Materials Science and Engineering, China University of Petroleum (East China). His research interests focus on the synthetic chemistry of polyoxometalate clusters, while designing energy catalytic materials for water electrolysis, fuel cells and ammonia synthesis.